LIST OF TABLES

LIST OF FIGURES

LIST OF ABBREVIATIONS

PM	Prime mover
SG	Synchronous generator
PLL	Phase-locked loops
UTSP	Unified three-phase signal processor
FFT	Fast Fourier transform
SISO	Single-input single-output
MIMO	Multiple-input multiple-output
SPS	Sim power systems
AVR	Automatic voltage regulator

LIST OF SYMBOLS AND UNITS OF MEASUREMENTS

v_{an}	Phase-neutral voltage, phase A (V)
$\mathbf{V}_{abc}$	Three-phase phase voltages matrix in abc-frame (V)
i_a	Line current, phase A (A)
$\mathbf{I}_{abc}$	Three-phase line currents matrix in abc-frame (A)
V_{dc}	DC-side voltage at the load (V)
E_{dc}	DC-side voltage at the rectifier (V)
I_{dc}	DC-side current at the rectifier (A)
ω	Frequency (rad/s)
α	Rectifier bridge firing angle (rad)
t	Time (s)
T	Period (s)
S_a	Switching function, phase A
$\mathbf{S}_{abc}$	Switching function matrix in abc-frame
$\mathbf{S}_{qd0}$	Switching function matrix in qd-frame
PF	Power factor
v_{s_a}	Source phase voltage, phase A (V)
v_{br_a}	Bridge input phase voltage, phase A (V)
V_L	Voltage drop across an inductance (V)
μ	Voltage notch width (rad)

r_μ	DC-side voltage drop equivalent resistance due to μ (Ω)
L_s	Equivalent source inductance (H)
V_{LL}	Line to line voltage under balanced conditions
V_{br}	Bridge input phase voltage (V)
ϕ	Phase angle of the phase voltage V_{br}
h	Harmonic order
$\mathbf{V}_{br,abc}$	Bridge input voltages matrix in abc-frame (V)
$\mathbf{V}_{br,qd0}$	Bridge input voltages matri in qd-frame (V)
$\mathbf{K}_s$	Park transform matrix
$\mathbf{K}_s^{-1}$	Inverse Park transform matrix
$\mathbf{T}_s$	Park transform augmented matrix for multiple three-phase signals system
$\mathbf{T}_s^{-1}$	Inverse Park transform augmented matrix for multiple three-phase signals system
θ	Park transform reference angle (rad)
δ_r	Park transform initial phase angle (rad)
δ_p	Positive sequence initial phase angle (rad)
δ_n	Negative sequence initial phase angle (rad)
δ_e	Phase angle error (rad)
ω_f	Filter frequency (rad/s)

INTRODUCTION

The research has been conducted with the industrial partner Andritz-Hydro, giving the opportunity to actually touch and manipulate the type of system that is to be modeled in this research. The company wanted to investigate the dynamic of their excitation system dynamics and its controls. The main goal of this research could be resumed in a single question that may seem not so complicated at first, but turned out to be much more challenging than originally anticipated. They wanted to know "Under which conditions can an excitation system be assumed as a first order?". The reason why this question was asked at first is because obviously from a modeling point of view, there is not a single pole present in the whole system since there is an excitation transformer, which introduces at least 4 poles in the loop, and also a line spike filter. Obviously, after asking the question and taking into account all the system's components, the first order hypothesis seemed like an oversimplification, which no one really knew where it came from (other than literature directly saying it can be assumed). To give a better visual reference of the synchronous generator control systems, figure 0.1 shows how the synchronous machine interacts with its control systems.

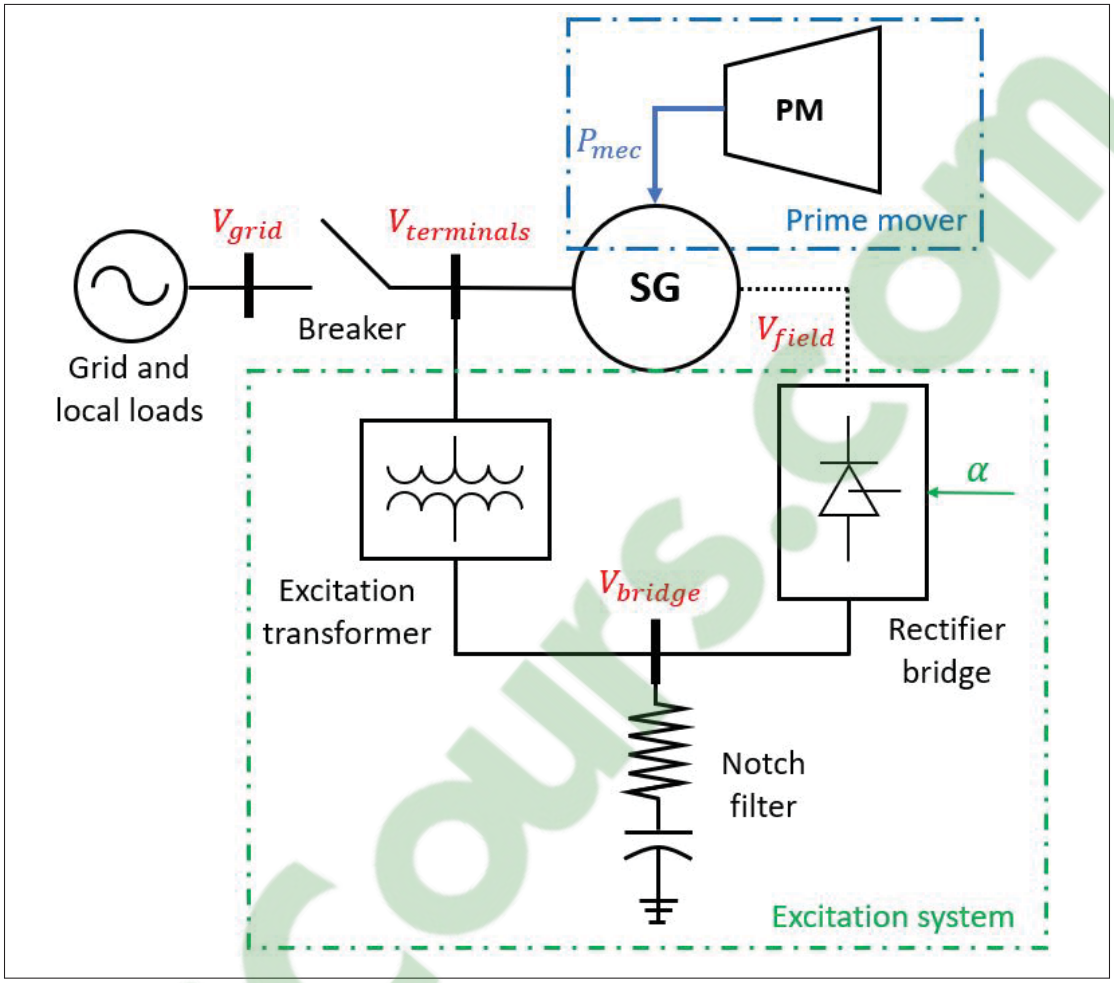

Figure 0.1 Schematic of the synchronous generator with its prime mover and excitation system

The synchronous machine has two modes of control. When the machine is offline, the control system's purpose is for synchronization with the grid. In such conditions, the voltage amplitude and phase angle of the machine terminals have to match the grid's before the breaker can be closed, and the machine is allowed to go online. The machine's internal voltage amplitude is controlled by the excitation system, while its phase angle and frequency is controlled by the prime mover in this mode of operation.

The online control mode is for power controls and direct interactions with the grid. Assuming that the active and reactive power are almost decoupled, we could say that the prime mover controls the active power through mechanical torque input on the machine's shaft. But more specifically, controlling the mechanical torque on the shaft creates a phase shift on the internal voltage of the machine in reference to the grid, which is called the power angle. The excitation system controls the generator's internal voltage magnitude again (like in offline mode). But in this case the goal of controlling the machine's voltage is to mainly control the reactive power output or input by going either under-excited or over-excited, which will dictate if the machine is consuming or emitting reactive power as mentioned in Chapman (2012). In short, the prime mover always has to do with frequency and phase angle of the machine's internal voltage, while the excitation system deals with the voltage magnitude.

To be able to understand the dynamics of the excitation system, its eigenvalues have to be extracted, and this will be the ultimate goal of this research. To do so, a review of the theory behind the rectifier bridges will be conducted. Then, the Park transform will be explained thoroughly. Next, the synchronization devices will be discussed in detail and two different types of PLL will be compared. Finally, the mathematical model by state-space representation of the excitation system will be built in Park's reference frame, and will also be validated both in simulations and with physical experiments.

CHAPTER 1

LITERATURE REVIEW

This chapter will tell how the references used in the research were able to advance the research, and give certain ideas that pushed the results forward. First, the whole process of using a thyristor-based rectifier bridge in itself can be overwhelmingly complicated for someone seeing it for the first time. The references used were able to give a quick but accurate understanding at first, but then came the idea of averaging the switching process to build a mathematical model. Then, since the rectifier bridge is to be used as an excitation system, basic understanding of synchronous machines was mandatory. Understanding the synchronous machine gave a hint of why the mathematical model of the excitation system has to be built in qd-frame to be used. Next, there are many ways to build a mathematical model of a physical system, but the state-space modeling technique turned out to be well aligned with the literature.

Thyristor-based rectifier bridges

The principal references used for the basic understanding of the thyristor rectifier bridges comes from Mohan (2003), Kundur (1994) and Erickson R. (2004), as they all touch the subject, but Erickson R. (2004) goes more into detail. All of them advance the theory of the commutation equivalent resistance due to line voltage notches caused by the line inductance effects. The commutation equivalent resistance has also been used for modeling purposes by Chaijarurnudomrung K.,K.-N. A. (2010). The switching process is also thoroughly explained in Kundur (1994), Mohan (2003) and Erickson R. (2004), which gives the basic knowledge needed to make a thyristor rectifier bridge firing board. In Chaijarurnudomrung K. (2010), the rectifier bridge is modeled as an averaged equivalent transformer model by doing the Fourier analysis on the square-shaped line current curves. The result is called the switching function, and can be used to obtain all the steady-state equations of the rectifier bridge given by Mohan (2003), Kundur (1994) and Erickson R. (2004).

The Park Transform

The Park transform is introduced in Kundur (1994) and Krause (2002), but the transform matrices that they use are not the same. For this research, the Park transform matrix used is the one that comes from Krause (2002). Since grids are not always perfectly balanced, properties of the Park transform under unbalanced conditions must be studied. The thesis Dupré (2019) does it, and explains how two sinusoidal signals of same amplitude shifted by 90 degrees can be injected in the inverse transform to obtain a clear harmonics-free negative sequence on the three-phase side of the transform. The theory of how the Park transform can be used to transfer differential equations into qd-frame is given in both Kundur (1994) and Krause (2002). Since a phase-angle reference is required for the Park transform, a synchronization device has to be used such as a PLL.

Synchronization devices

The book Best (2003) gives basic understanding of phase-locked loops, and is a good entry-level source on the subject. The author actually explains how and why mathematical models are made for such devices. The performance characteristics needed for a PLL to recover the phase angle properly are given, and the trade-off of the bandwidth versus the response time is explained. Also, the book has a chapter on how to incorporate filters into the loop and stabilize the devices through control problems solving. However, the phase detector used in the book are not what was used in the research simply because the qd-frame phase detector fits better in the body of the research, introducing the need for qd-frame signal analysis.

Two PLL devices are to be designed in the research. One of them uses the usual abc-frame signals and is the Unified Three-Phase Signal Processor (UTSP), first introduced in Karimi (2008), then improved and simplified in Karimi H.,Y. S. (2019). The UTSP is a PLL that is actually able to decouple the sequences of a three-phase signal, and give their angles and amplitudes separately. The other one uses Park transform as a phase detector, meaning that the signals going in the filter are in qd-frame. The article Karimi H. (2012) uses a combination

of Clarke and Park transforms as a phase detector since the PLL is to be used for single-phase synchronization. The synchronization device of this research needs to be for three-phase circuits applications, so the Clarke transform was removed. However, the stability analysis method is clearly explained, and thus the filter can be adapted for lower frequency harmonics applications. The line inductance is also assumed to be of high value in the physical applications of the excitation system model, since the excitation transformer is design to attenuate short-circuits, and has high leakage inductance values, therefore notches are always present on the three-phase signals entering the rectifier bridge's synchronization system.

To properly design a synchronization system, the input signals have to be correctly characterized to design the filter accordingly, which must be designed before the loop controller can stabilize the whole thing and set the performance characteristics. The book Corinthios (2009) gives all the knowledge needed for Fourier analysis as well as filter design, with the mathematical background needed to understand exactly how the Fourier analysis can be conducted on the bridge input phase voltages. The article Graham (1993) gives the method for a Fourier analysis done of the input bridge voltage. The Fourier analysis is done on a trapezoidal-shaped line currents (in presence of line voltage notches), then the equivalent impedance seen by the bridge is used to calculate the voltage drop in the equivalent inductance to find the input bridge voltage frequency characterstics. The results given by the Fourier analysis had to be transferred into qd-frame. The only article found on the Park transform's frequency domain properties Zhang B.,Yi S. (2000), but the results are not proven in any way, and the method's basic hypothesis are not exactly clearly given. Still, this article gave away the idea that some work could be done on the properties of the Park transform when used on signals containing harmonics.

Modeling of the excitation system

In Krause (2002) and Kundur (1994), the excitation systems are explained, setting the hypothesis used for the excitation system model creation. Those references actually tell us that a transformer is in the excitation loop, as well as a harmonic filter, telling us the exact topology of the excitation circuit used to build the mathematical model. Since the synchronous machine modeling is

always in qd-frame, we will use the Park transform to model the whole excitation system. The book Balabanian N. (1969) gives strong techniques for state-space modeling of complex systems called circuit tearing. The technique tells us that the separate subsystems can be modeled and validated separately, before being put together in a functioning global model. Also, the state-space representation modeling method is thoroughly explained in Balabanian N. (1969), as well as the meaning of such mathematical knowledge on a physical system. The state-space model of the excitation system can be used to extract eigenvalues (or closed-loop poles) of the system, much needed for the control system design of the excitation system. It can also be used to conduct transient analysis on the system, which is how the model will be validated.

Before the excitation system modeling can be started, the behavior of thyristor-based six-pulse rectifier bridges has to be studied, which is the subject of the next chapter.

CHAPTER 2

THYRISTOR-BASED SIX-PULSE RECTIFIER BRIDGE THEORY

This chapter gives the basic theory needed on six-pulse thyristor-based rectifiers to be able to follow every step of the research. First, the switching behavior is explained thoroughly to introduce how the switching function will be created. Then, the switching function is built by Fourier analysis on a flat-shaped current waveform to obtain an equivalent transformer expression. This equivalent transformer expression is an algebraic relation that will use the firing angle to line the three-phase side to the DC side of the excitation system. The line voltage notch phenomenon is also explained, and a full Fourier analysis is done on the trapezoidal-shaped current waveform to build the harmonic terms expressions of the three-phase currents and voltages of the rectifier bridge. After this chapter, one should be able to understand how equations are drawn from a switching circuit to build an averaged mathematical model into abc-frame.

To continue further with the chapter, the following assumptions have to be made.

1. Three-phase circuits are perfectly balanced.
2. Line resistance is neglectible.
3. The DC side inductance is large enough to apply the small ripple approximation, which is reasonable for large synchronous machines.

2.1 Three-phase rectifier bridge ideal switching behavior

In an ideal switching pattern, there are two switches (thyristors) conducting at all times. Figure 2.1 gives the general topology of a three-phase rectifier bridge, with the reference to each switches that will be used to explain the switching pattern.

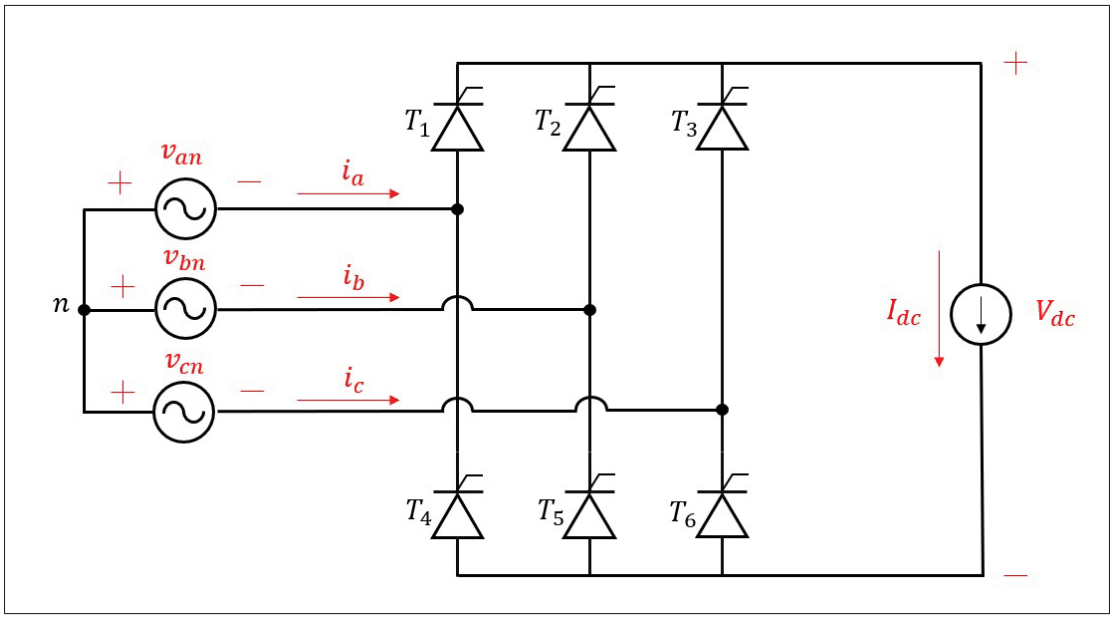

Figure 2.1 General topology of a 6-pulse rectifier bridge

The DC current source on the DC side is there according to the assumption that the DC side current is almost perfectly constant, with either very low or no ripple. In reality, a large inductance has to be present on the DC load to achieve this. Since the bridge is connected to a synchronous machine rotor, the large inductance assumption is always valid, their time constants being typically in the order of around a second.

A pair of thyristors connected to the same phase are called an Arm. Thyristors T_1 and T_4 are the phase A arm, T_2 and T_5 for phase B, T_3 and T_6 for phase C. Upper arms are the thyristors connected to the positive terminal of the DC side, and lower arms are the ones connected to the negative terminal. Some states of the switching pattern will never happen and that is a complete arm conducting. The ideal switching pattern goes as follows. Let us consider the following line voltages : $V_{ab}, V_{ac}, V_{bc}, V_{ba}, V_{ca}, V_{cb}$. These are the AC sources that will be connected to the DC side one sixth of a cycle each to produce the DC voltage at the output. Meaning that the period window in which the thyristors can be activated is 120 degrees in total, separated in two periods of 60 degrees. The switches can be activated when the voltage of the arm on

which the switch is connected in respect to the other two arms is higher in magnitude than any other possible line voltage (of the 6 possibilities). For example, if we consider the switch T_2, its conducting window would be when line voltages V_{ba}, V_{bc} would be higher in magnitude than the other 4 line voltages. Starting with the line voltage V_{ab} connected to the DC-side (T_1 and T_5 conducting). Once V_{ac} gets higher in magnitude than V_{ab}, T_5 stops conducting, and T6 must be activated next. Once V_{bc} gets higher than V_{ac}, T_1 stops conducting, and T_2 can be activated, and so on. Considering 6 switching configurations, every thyristor will conduct in 2 consecutive configuration, and the next switching pattern is determined alternatively between the upper and lower arms. To illustrate better the patterns, the figure below shows the conducting thyristors for every sequence (6 sequences in total going from S_1 to S_6).

Sequence	s_1	s_2	s_3	s_4	s_5	s_6
Upper arms	T_1		T_2		T_3	
Lower arms	T_5	T_6		T_4		T_5

Figure 2.2 Conducting thyristors for every sequence of a cycle of the rectifier bridge

As said before, to determine the current waveform of the lines, we must assume that the DC-side inductance is large enough to apply the small ripple approximation. Also, the line inductances need to be small enough to consider the transitions between the current states as instantaneous (neglecting the voltage notches for now). There are three possibilities for the line currents (three possible states), which are either $I_{dc}, 0, -I_{dc}$. When the upper arm of the phase is connected to the DC-side, the current going through the line is I_{dc}. When no arms of the phase are connected, the current is null, and when the lower arm of the phase is connected to the DC-side, the line current is equal to $-I_{dc}$. To better illustrate, the figure 2.3 shows the ideal waveform of the line A current, $i_a(t)$.

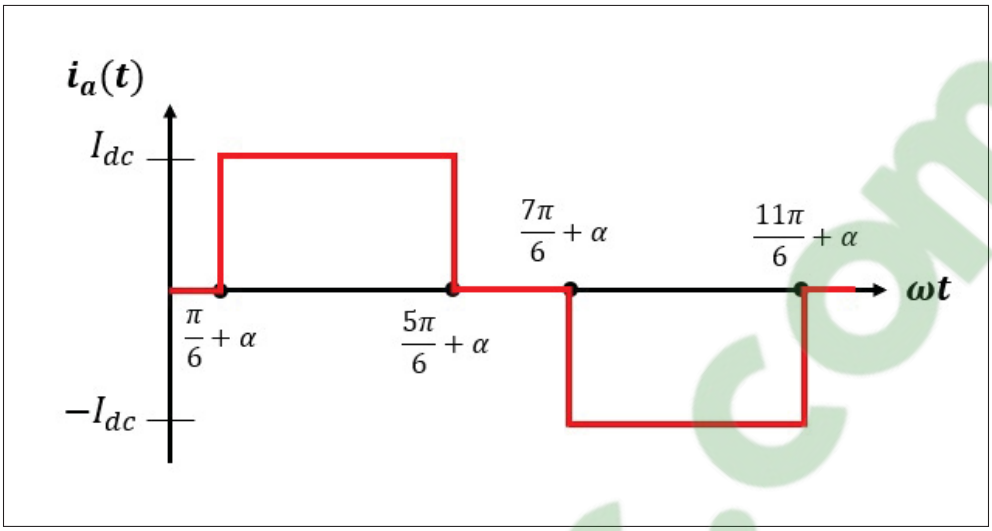

Figure 2.3 Waveform of the line current used for the Fourier analysis

2.2 Expression of the switching function of the rectifier bridge

The next step is to use the waveform of figure 2.3 to find a periodic function expressed with time. The function will be found with the Fourier analysis, and will be called Switching Function. Knowing that any signal can be expressed as a sum of sine and cosine functions with a DC-component added to it, we may write:

$$f(t) = a_0 + \sum(a_n \cos(n\omega t)) + \sum(b_n \sin(n\omega t)) \tag{2.1}$$

Just by looking at the waveform of figure 2.3, we know that the DC-component is null (by symmetry), so $a_0 = 0$. The terms a_n and b_n for a waveform of unitary amplitude are expressed:

$$\begin{aligned} a_n &= \frac{\omega}{\pi}\int_0^T \cos(n\omega t)dt \\ b_n &= \frac{\omega}{\pi}\int_0^T \sin(n\omega t)dt \end{aligned} \tag{2.2}$$

Developing the a_n term first:

$$
\begin{aligned}
a_n &= \int_{\frac{\pi/6+\alpha}{\omega}}^{\frac{5\pi/6+\alpha}{\omega}} \cos(n\omega t)dt - \int_{\frac{7\pi/6+\alpha}{\omega}}^{\frac{11\pi/6+\alpha}{\omega}} \cos(n\omega t)dt \\
&= \frac{1}{n\pi}\left(\sin(n5\pi/6 + n\alpha) - \sin(n\pi/6 + n\alpha) - \sin(n11\pi/6 + n\alpha) + \sin(n7\pi/6 + n\alpha)\right) \\
&= \frac{1}{n\pi}(\cos(n\alpha)(\sin(5n\pi/6) - \sin(n\pi/6) - \sin(11n\pi/6) + \sin(7n\pi/6)) \\
&+ \sin(n\alpha)(\cos(5n\pi/6) - \cos(n\pi/6) - \cos(11n\pi/6) + \cos(7n\pi/6))) \\
&= \frac{1}{n\pi}\sin(n\alpha)(2\cos(5n\pi/6) - 2\cos(n\pi/6)) \\
&= \frac{-4}{n\pi}(\sin(n\alpha)\sin(n\pi/2)\sin(n\pi/3))
\end{aligned}
$$

The final expression of a_n being:

$$
a_n = \frac{-4\sin(n\alpha)\sin(\frac{n\pi}{2})\sin(\frac{n\pi}{3})}{n\pi} \tag{2.3}
$$

Developing the b_n term:

$$
\begin{aligned}
b_n &= \int_{\frac{\pi/6+\alpha}{\omega}}^{\frac{5\pi/6+\alpha}{\omega}} \sin(n\omega t)dt - \int_{\frac{7\pi/6+\alpha}{\omega}}^{\frac{11\pi/6+\alpha}{\omega}} \sin(n\omega t)dt \\
&= \frac{1}{n\pi}(-\cos(5n\pi/6 + n\alpha) + \cos(n\pi/6 + n\alpha) + \cos(11n\pi/6 + n\alpha) - \cos(7n\pi/6 + n\alpha)) \\
&= \frac{1}{n\pi}(\cos(n\alpha)(-\cos(5n\pi/6) + \cos(n\pi/6) + \cos(11n\pi/6) - \cos(7n\pi/6)) \\
&+ \sin(n\alpha)(\sin(5n\pi/6) - \sin(n\pi/6) - \sin(11n\pi/6) + \sin(7n\pi/6))) \\
&= \frac{1}{n\pi}\cos(n\alpha)(2\cos(n\pi/6) - 2\cos(5n\pi/6)) \\
&= \frac{4}{n\pi}\cos(n\alpha)\sin(n\pi/2)\sin(n\pi/3)
\end{aligned}
$$

The final expression of b_n being:

$$b_n = \frac{4\cos(n\alpha)\sin(\frac{n\pi}{2})\sin(\frac{n\pi}{3})}{n\pi} \tag{2.4}$$

Now to build the signal in terms of sine and cosine term summed, we use equation (2.1), and replace the a_n and b_n terms in the equation. The following signal built will be called switching function $S_a(t)$ of the phase-A of the rectifier. We find:

$$\begin{aligned} S_a(t) &= \frac{-4\sin(n\alpha)\sin(\frac{n\pi}{2})\sin(\frac{n\pi}{3})}{n\pi}\cos(n\omega t) + \frac{4\cos(n\alpha)\sin(\frac{n\pi}{2})\sin(\frac{n\pi}{3})}{n\pi}\sin(n\omega t) \\ &= \frac{4}{n\pi}\sin\left(\frac{n\pi}{2}\right)\sin\left(\frac{n\pi}{3}\right)(-\sin(n\alpha)\cos(n\omega t) + \cos(n\alpha)\sin(n\omega t)) \\ &= \frac{4}{n\pi}\sin\left(\frac{n\pi}{2}\right)\sin\left(\frac{n\pi}{3}\right)\sin(n\omega t - n\alpha) \end{aligned}$$

The final result of the switching function of the phase-A being:

$$S_a(t) = \frac{4sin(\frac{n\pi}{2})\sin(\frac{n\pi}{3})\sin(n\omega t - n\alpha)}{n\pi} \tag{2.5}$$

Multiplying equation (2.5) by the current value of the DC side of the rectifier would give the waveform of the line current. Since we must neglect the harmonics for the dq0 model we wish to build, we keep only the term for $n = 1$ in the equation (2.5), giving:

$$S_a(t) = \frac{2\sqrt{3}}{\pi}\sin(\omega t - \alpha) \tag{2.6}$$

Since we know that the current flowing through phase B and C are the same as phase A but shifted in phase by 120 degrees, we may express the switching function as a matrix:

$$\mathbf{S}_{abc}(t) = \begin{bmatrix} S_a(t) \\ S_b(t) \\ S_c(t) \end{bmatrix} = \frac{2\sqrt{3}}{\pi} \begin{bmatrix} \sin(\omega t - \alpha) \\ \sin(\omega t - \alpha - 2\pi/3) \\ \sin(\omega t - \alpha + 2\pi/3) \end{bmatrix} \tag{2.7}$$

2.3 Steady-state equations equations in abc reference frame

The switching function is to be used as transformer-equivalent model equations of the rectifier for steady-state values calculations. The DC voltage can be expressed as (Chaijarurnudomrung K. (2010)):

$$E_{dc} = \mathbf{S}_{abc}(t)^T \mathbf{V}_{abc} \tag{2.8}$$

From there, the matrix multiplications can be expanded, then simplified with trigonometric identities, yielding.

$$E_{dc} = \frac{3\sqrt{2}}{\pi} V_{LL(rms)} \cos(\alpha)$$

Equation (2.3) is also known in the literature as:

$$E_{dc} = 1.3505 \ \cos(\alpha) \ V_{L(rms)}$$

Equation (2.8) links the DC voltage to the three-phase line-to-line voltage (Root Mean Square (rms) value). The line current can also be linked to the DC current with the following equation given in Chaijarurnudomrung K. (2010):

$$\mathbf{I}_{abc} = I_{dc} \mathbf{S}_{abc} \tag{2.9}$$

Expanding the terms yields:

$$\mathbf{I}_{abc} = \frac{2\sqrt{3}}{\pi} I_{dc} \begin{bmatrix} \sin(\omega t - \alpha) \\ \sin(\omega t - \alpha - 2\pi/3) \\ \sin(\omega t - \alpha + 2\pi/3) \end{bmatrix}$$

While supposing that the line currents are balanced, their fundamental rms magnitude can be expressed as:

$$I_{fund(rms)} = \frac{\sqrt{6}}{\pi} I_{dc} = 0.78 I_{dc} \tag{2.10}$$

The rms value of a signal can be expressed by the well known relation:

$$f_{rms} = \sqrt{f_0^2 + \sum_{n=1}^{\infty} \frac{f_n^2}{2}} \tag{2.11}$$

Supposing that the voltage on the AC side of converter is perfectly sinusoidal, its rms value is obtained by dividing its amplitude by a $\sqrt{2}$ factor.

Since the line current have harmonics content (determined before by the switching function equation (2.5), the total rms value of the current can be computed. Expressing the rms value of the current as:

$$I_{rms} = \sqrt{I_0^2 + \sum_{n=1}^{\infty} \frac{I_n^2}{2}} \tag{2.12}$$

Knowing that there is no DC value in the line current, the I_0 term can be removed. Also, using equation (2.5) multiplied by the DC current as I_n terms, one finds the total rms line current to be:

$$I_{rms} = \frac{I_{dc}}{\sqrt{2}}\sqrt{\sum_{n=1}^{\infty}\left(\frac{4}{n\pi}\sin\left(\frac{n\pi}{2}\right)\sin\left(\frac{n\pi}{3}\right)\right)}$$
$$= \frac{I_{dc}}{\sqrt{2}}\sqrt{\frac{4}{3}}$$

Which can be reduced to:

$$I_{rms} = \sqrt{\frac{2}{3}}I_{dc} \tag{2.13}$$

The average power of a signal containing harmonics can be expressed as:

$$P_{av} = \frac{V_0 I_0}{2} + \sum_{n=1}^{\infty}\frac{V_n I_n}{2}\cos(\phi_n - \theta_n) \tag{2.14}$$

Equation (2.14) tells us that power is produced by the harmonics only when the current and voltage harmonics are at the same frequency. Since we assume the voltage on the AC side to be sinusoidal, the only frequency of the current affecting the power is the fundamental. We know that the phase shift between the voltage and current at fundamental frequency is the angle α caused by the rectifier bridge imposing its phase shift. We can then reduce equation (2.14) to:

$$P_{av} = \frac{V_1 I_1}{2}\cos(\alpha) \tag{2.15}$$

The power of two signals containing harmonics is expressed:

$$PF = \frac{P_{av}}{V_{rms} I_{rms}} \tag{2.16}$$

Using equations (2.13, 2.15 and 2.16) we find the power factor to be:

$$PF = \frac{\frac{V_1}{2}\frac{2\sqrt{3}}{\pi} I_{dc}\cos(\alpha)}{I_{dc}\sqrt{\frac{2}{3}}\frac{V_1}{\sqrt{2}}}$$

Which can be reduced to:

$$PF = \frac{3\cos(\alpha)}{\pi} \tag{2.17}$$

Equation (2.17) gives us the power factor, while considering the harmonic content of the line current. This tells us that the highest power factor we can achieve is in fact $3/\pi$. Since we know that for an ideal converter, the power entering on the three-phase side is all transferred to the DC side, we understand that the harmonic content of the current tends to create reactive power only. However, it is true only because the line voltage is considered purely sinusoidal for now.

2.4 Line inductance effects on the rectifier bridge

To have better visual reference for the rest of the chapter, figure 2.4 shows the electrical schematic of the rectifier bridge with line inductance added.

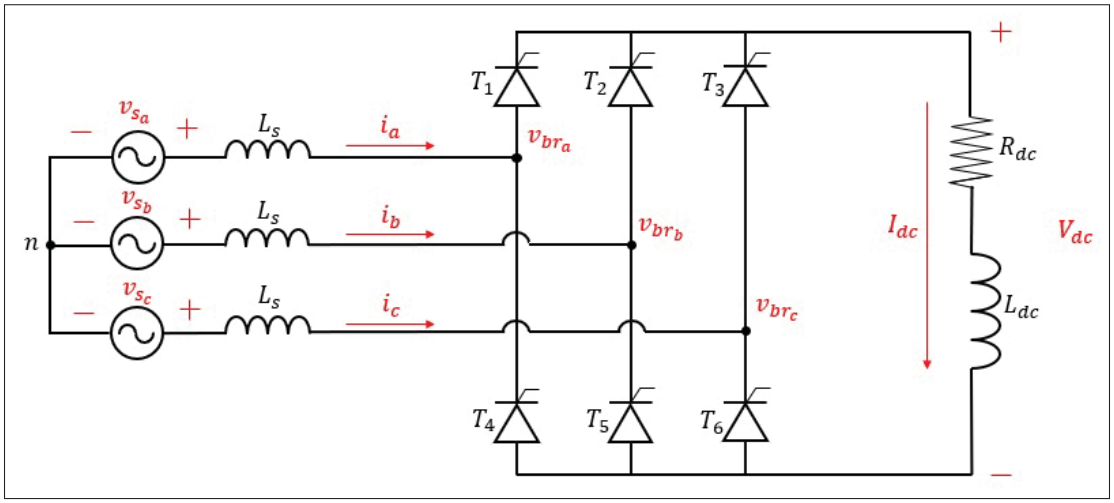

Figure 2.4 Electrical schematic of the rectifier bridge with line inductance added

When line inductances appear on the lines feeding a rectifier bridge using thyristors, two main phenomenon start to take place. First, since the inductance is seen as an impedance, there will be a phase shift between the source voltage $\mathbf{V}_{s,abc}$and the input voltage of the bridge $\mathbf{V}_{br,abc}$. This means that the phase shift created by the bridge is no longer between the source voltage and the line current anymore. But instead between the bridge voltage $\mathbf{V}_{br,abc}$ and the line currents $\mathbf{I}_{abc}$. The second phenomenon is the line voltage notches.

The notch phenomenon happens when two thyristors of the same DC-pole (but two different phases) conduct together for a short period of time. For example, while the upper arm conducting goes from phase A to phase B, there is a short period of time during which both thyristors will conduct. During this time, the two thyristors will exchange current. As the thyristor connected to phase A has his current decreasing, the thyristor connected to phase B has his current increased while the thyristor connected to the negative DC-pole stays connected and has a constant current flowing through it. The figure below shows modified sequences of the conducting thyristors (derived from figure 2.2). The N sequence present in the table is to indicate when a line voltage notch happens.

Sequence	s_1	N	s_2	N	s_3	N	s_4	N	s_5	N	s_6	N
Upper arms	T_1			$T_{1,2}$	T_2			$T_{2,3}$	T_3			$T_{3,1}$
Lower arms	T_5	$T_{5,6}$	T_6			$T_{6,4}$	T_4			$T_{4,5}$	T_5	

Figure 2.5 Conducting thyristors for every sequence of a cycle of the rectifier bridge with voltage notch phenomenon

This phenomenon happens because the line inductance opposes current variations, as the well-known differential expression $V_L = L\frac{d(I_L)}{dt}$ tells us so. The perfect square-wave line current

is never supposed to happen in theory if there is an inductance present on the lines. We know from the inductance's differential expression that if the inductance value is high, the current will take more time reaching his next step value. If the step value itself (DC-current value) is higher, it will also take more time for the line current to reach its maximum value. Based on that, we know that the phenomenon worsens as the DC current or the line inductance increases. Also, DC current rises as the firing angle lowers in thyristors bridge. The figure below shows the line current over a full period when voltage notch phenomenon occurs. Note that the notch width is denoted μ.

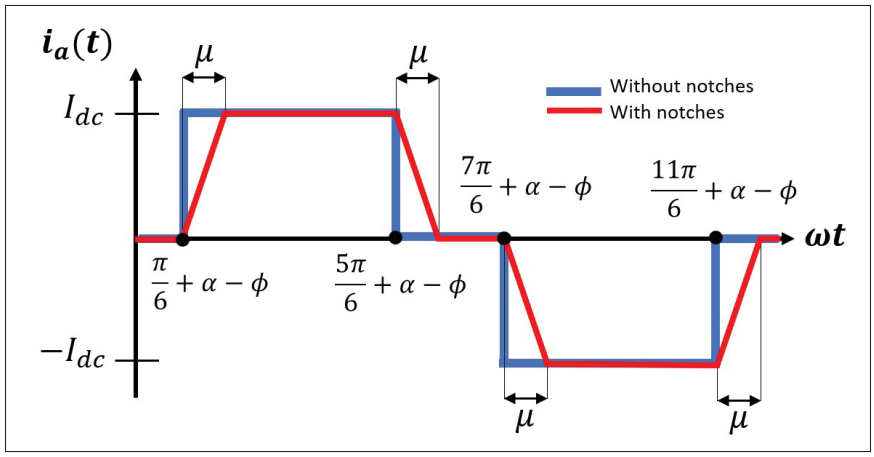

Figure 2.6 Line current over a full period when voltage notch phenomenon occurs

If notches go wider than 60 degrees (one sixth of a period), four thyristors will conduct at the same time. Since the future averaged model takes into account the voltage notches with an equivalent DC resistor r_μ, we can expect the model to severely diverge if the notches reach this point. On the line current waveform, we will see the notches reaching 60 degrees wide when the line currents no longer have a plateau at zero on their waveform.

In Mohan (2003), the DC-side voltage is expressed in terms of line inductance and DC-current as:

$$V_{dc} = \frac{3\sqrt{2}}{\pi} V_{LL} \cos(\alpha) - \frac{3\omega L_s I_{dc}}{\pi}$$

This equation gives us a way to represent the voltage drop on the average DC voltage due to the voltage notch phenomenon as a resistor in which the direct current flows through. The resistance r_μ is expressed by:

$$r_\mu = \frac{3\omega L_s}{\pi} \tag{2.18}$$

Note that in a real application, the voltage drop due to the voltage notch phenomenon does not cause additional losses in the rectifier bridge, meaning that the voltage loss produced by the voltage notch phenomenon will not cause any additional heat in the rectifier bridge. In the control system, the steady-state error created by the notches should be easily removed by the generator's Automatic Voltage Regulator (AVR) controller.

There is also a way to express the voltage notch width in terms of firing angle, line inductance, grid frequency, source voltage and DC current. In Mohan (2003), the notch width μ is expressed in the equation:

$$\cos(\alpha + \mu) = \cos(\alpha) - \frac{2\omega L_s I_{dc}}{\sqrt{2} V_{LL}} \tag{2.19}$$

By isolating the notch width, we find:

$$\mu = \cos^{-1}\left(\cos(\alpha) - \frac{2\omega L_s I_{dc}}{\sqrt{2} V_{LL}}\right) - \alpha \tag{2.20}$$

Equation (2.19) is useful since the equivalent line inductance seen be a rectifier bridge is difficult to establish precisely (as well as the infinite bus voltage behind it). Using this equation by isolating the line inductance would give the possibility to calculate the line inductance seen by

the converter by measuring the notch width with an oscilloscope. Also, this equation will be directly used to show the limits of the dq0 model of the rectifier in the part where the validation of the model with simulation tools is done.

The addition of an inductance on the lines also creates a phase shift between the source and the voltage input of the rectifier. Since the phase shift created by the rectifier is between its input voltage and the line currents, the angle of the voltage input $V_{br}\angle\phi$ has to be added to equation (2.7). Then, equation (2.7) becomes:

$$\mathbf{S}_{abc}(t) = \begin{bmatrix} S_a(t) \\ S_b(t) \\ S_c(t) \end{bmatrix} = \frac{2\sqrt{3}}{\pi} \begin{bmatrix} \sin(\omega t - \alpha + \phi) \\ \sin(\omega t - \alpha + \phi - 2\pi/3) \\ \sin(\omega t - \alpha + \phi + 2\pi/3) \end{bmatrix} \tag{2.21}$$

2.5 Rectifier bridge input phase voltages and line currents Fourier analysis

A Fourier analysis can be done on the trapezoidal-shaped line currents of the rectifier to predict the harmonics content caused by the equivalent line inductances seen by the rectifier. Once the current is known, the voltage can then be deduced. The final goal is to know precisely the harmonics content of the input phase voltages of the rectifier to be able to design the synchronization system accordingly. By using the same method as the Fourier analysis of the square-wave currents developed section 2.2 and figure 2.6 as a reference, we write the Fourier coefficients of the trapezoidal currents:

$$\begin{aligned} a_h(t) = \frac{\omega}{\pi}\left(\int_{T_1}^{T_2} f_1(t)\cos(h\omega t)dt + \int_{T_2}^{T_3} \cos(h\omega t)dt + \int_{T_3}^{T_4} f_2(t)\cos(h\omega t)dt\right) \\ + \frac{\omega}{\pi}\left(\int_{T_5}^{T_6} f_3(t)\cos(h\omega t)dt - \int_{T_6}^{T_7} \cos(h\omega t)dt + \int_{T_7}^{T_8} f_4(t)\cos(h\omega t)dt\right) \end{aligned}$$

$$b_h(t) = \frac{\omega}{\pi}\left(\int_{T_1}^{T_2} f_1(t)\sin(h\omega t)dt + \int_{T_2}^{T_3}\sin(h\omega t)dt + \int_{T_3}^{T_4} f_2(t)\sin(h\omega t)dt\right)$$
$$+ \frac{\omega}{\pi}\left(\int_{T_5}^{T_6} f_3(t)\sin(h\omega t)dt - \int_{T_6}^{T_7}\sin(h\omega t)dt + \int_{T_7}^{T_8} f_4(t)\sin(h\omega t)dt\right)$$

Where $f_i(t)$ functions used to represent the notch effects on the currents are:

$$f_1(t) = \frac{\omega t - \alpha - \pi/6}{\mu}$$
$$f_2(t) = \frac{-\omega t + \alpha + \mu + 5\pi/6}{\mu}$$
$$f_3(t) = \frac{-\omega t + \alpha + 7\pi/6}{\mu}$$
$$f_4(t) = \frac{\omega t - \alpha - \mu}{\mu}$$

And the terms T_i are:

$$T_1 = \frac{\alpha + \pi/6}{\omega}, T_2 = \frac{\alpha + \pi/6 + \mu}{\omega}, \quad T_3 = \frac{\alpha + 5\pi/6}{\omega}, T_4 = \frac{\alpha + 5\pi/6 + \mu}{\omega},$$
$$T_5 = \frac{\alpha + 7\pi/6}{\omega}, T_6 = \frac{\alpha + 7\pi/6 + \mu}{\omega}, \quad T_7 = \frac{\alpha + 11\pi/6}{\omega}, T_8 = \frac{\alpha + 11\pi/6 + \mu}{\omega}$$

By combining the Fourier coefficients, the line current for a single phase can then be written:

$$I_a(t) = I_{dc} f_h(t)$$

Where the function $f_h(t)$ is identified as:

$$f_h(t) = a_h(t)\cos(h\omega t) + b_h(t)\sin(h\omega t)$$

Function $f_h(t)$ being the result of 12 integral terms combined with trigonometric multiplications, it results into a function without closed form. The approach used to write simplified equations is to express the result of $f_h(t)$ for h going from 1 to 15, then find a recurring pattern. By using trigonometric functions and superposing them by multiplications to fit the recurring pattern of $f_h(t)$, we can find an equivalent expression $(e_h(t))$that will be way more simplified and easier to work with. The function $f_h(t)$ terms for $h = 1$ to 15 are:

Table 2.1 $f_h(t)$ harmonic terms

h order	Fourier coefficients function harmonic terms
1	$\frac{\sqrt{3}(2\cos(\alpha-\omega t)-2\cos(\alpha+\mu-\omega t))}{\mu\pi}$
2	0
3	0
4	0
5	$-\frac{\sqrt{3}(2\cos(5\alpha-5\omega t)-2\cos(5\alpha+5\mu-5\omega t))}{25\mu\pi}$
6	0
7	$-\frac{\sqrt{3}(2\cos(7\alpha-7\omega t)-2\cos(7\alpha+7\mu-7\omega t))}{49\mu\pi}$
8	0
9	0
10	0
11	$\frac{\sqrt{3}(2\cos(11\alpha-11\omega t)-2\cos(11\alpha+11\mu-11\omega t))}{121\mu\pi}$
12	0
13	$\frac{\sqrt{3}(2\cos(13\alpha-13\omega t)-2\cos(13\alpha+13\mu-13\omega t))}{169\mu\pi}$

We can already see that we express a function $g_h(t)$ as:

$$g_h(t) = \frac{2\cos(h\alpha - h\omega t) - 2\cos(h\alpha + h\mu - h\omega t)}{\pi\mu h^2}$$

Which by trigonometric identity, is also equal to:

$$g_h(t) = \frac{4\sin\left(h\omega t - h\alpha - \frac{h\mu}{2}\right)\sin\left(\frac{h\mu}{2}\right)}{\pi\mu h^2}$$

And can also be expressed with the $\mathrm{sinc}(x)$ function for future analysis:

$$g_h(t) = \frac{-2\sin\left(h\omega t - h\alpha - \frac{h\mu}{2}\right)\mathrm{sinc}\left(\frac{h\mu}{2}\right)}{\pi h}$$

Next, we need to build a z_h function that will create the recurring pattern in the harmonics. It needs to alternate sign every 2 terms, and give some sort of constant of $\sqrt{3}$, and all even terms need to be cut out. To do that, we use $z_1(h) = \cos(\frac{h\pi}{6})$ and $z_2(h) = \sin(\frac{h\pi}{2})^2$, and multiply them.

Table 2.2 z_h harmonic terms

h order	$\mathbf{z_1(h)}$	$\mathbf{z_2(h)}$	**Recurring function** $\mathbf{z_h = z_1(h)z_2(h)}$
1	$\sqrt{3}/2$	1	$\sqrt{3}/2$
2	1/2	0	0
3	0	1	0
4	-1/2	0	0
5	$-\sqrt{3}/2$	1	$-\sqrt{3}/2$
6	-1	0	0
7	$-\sqrt{3}/2$	1	$-\sqrt{3}/2$
8	-1/2	0	0
9	0	1	0
10	1/2	0	0
11	$\sqrt{3}/2$	1	$\sqrt{3}/2$
12	1/2	0	0
13	$\sqrt{3}/2$	1	$\sqrt{3}/2$

Desired function $e_h(t)$ equivalent to $f_h(t)$ is built by multiplying z_h and $g_h(t)$:

$$e_h(t) = 2(z_h)g_h(t)$$

With the expanded version:

$$e_h(t) = \frac{4\cos\left(\frac{h\pi}{6}\right)\sin\left(\frac{h\pi}{2}\right)^2 \sin\left(h\omega t - h\alpha - \frac{h\mu}{2}\right)\mathrm{sinc}\left(\frac{h\mu}{2}\right)}{\pi h}$$

For verification purposes, the spectrum has been reconstructed with both $e_h(t)$ and $f_h(t)$, and superposed, with an example using the parameters $\alpha = 0$, $\omega = 120\pi$ and $\mu = \pi/6$ and taking the first 25 h harmonics orders. Figure 2.7 shows the superposed reconstructed curves.

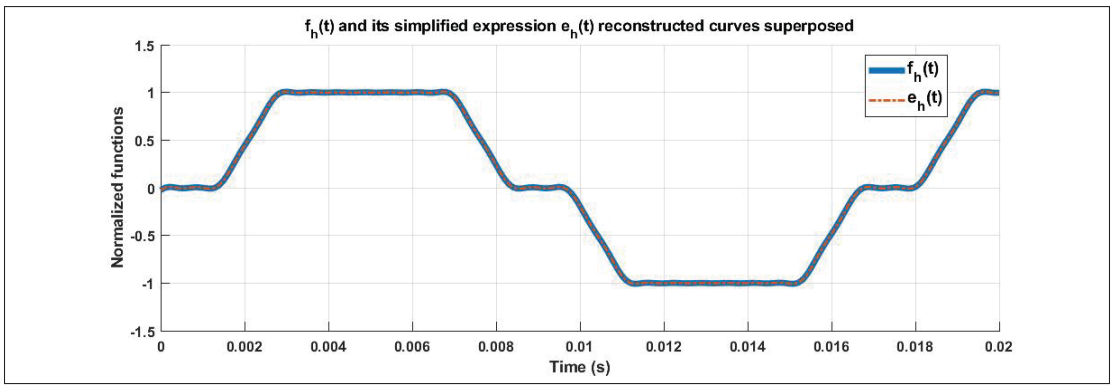

Figure 2.7 Comparison between $f_h(t)$ and $e_h(t)$ by superposition of reconstructed curves

Since the curves are perfectly superposed, it shows that $f_h(t)$ and $e_h(t)$ are actually equal. We can then expand the $e_h(t)$ expression into three-phase signals $\mathbf{e}_{abc}$ that will be used to reconstruct the input bridge voltage $\mathbf{V}_{br,abc}$ spectrum. We define $\mathbf{e}_{abc}$ as a three-phase signal as:

$$\mathbf{e}_{abc} = \frac{4\cos\left(\frac{h\pi}{6}\right)\sin\left(\frac{h\pi}{2}\right)^2 \operatorname{sinc}\left(\frac{h\mu}{2}\right)}{\pi h}\begin{bmatrix} \sin\left(h\omega t - h\alpha - \frac{h\mu}{2}\right) \\ \sin\left(h\omega t - h\alpha - \frac{h\mu}{2} - \frac{2\pi h}{3}\right) \\ \sin\left(h\omega t - h\alpha - \frac{h\mu}{2} + \frac{2\pi h}{3}\right) \end{bmatrix}$$

Using the voltage drop across the equivalent inductance, the bridge input phase voltage is written:

$$\mathbf{V}_{br,abc} = \mathbf{V}_{s,abc} - \mathbf{V}_{L,abc} = \mathbf{V}_{s,abc} - jhI_{dc}\omega L_s \mathbf{e}_{abc}$$

Knowing that the j operator adds a phase shift of $\pi/2$ to periodic signals, we may write the voltage drop across the equivalent inductance as:

$$\mathbf{V}_{L,abc} = \frac{4\omega L_s I_{dc} cos(\frac{h\pi}{6})\sin(\frac{h\pi}{2})^2 sinc(\frac{h\mu}{2})}{\pi}\begin{bmatrix} \sin(h\omega t - h\alpha - \frac{h\mu}{2} + \frac{\pi}{2}) \\ \sin(h\omega t - h\alpha - \frac{h\mu}{2} + \frac{\pi}{2} - \frac{2n\pi}{3}) \\ \sin(h\omega t - h\alpha - \frac{h\mu}{2} + \frac{\pi}{2} + \frac{2n\pi}{3}) \end{bmatrix}$$

And considering the source voltage $\mathbf{V}_{s,abc}$ to be harmonics-free, it is given by:

$$\mathbf{V}_{s,abc} = V_s\begin{bmatrix} \sin(\omega t) \\ \sin(\omega t - \frac{2\pi}{3}) \\ \sin(\omega t + \frac{2\pi}{3}) \end{bmatrix}$$

We can also write the voltage harmonics for orders $h > 1$:

$$\mathbf{V}_{br,abc} = \frac{4\omega L_s I_{dc}\cos(\frac{h\pi}{6})\sin(\frac{h\pi}{2})^2 sinc(\frac{h\mu}{2})}{\pi}\begin{bmatrix} \sin(h\omega t - h\alpha - \frac{h\mu}{2} - \frac{\pi}{2}) \\ \sin(h\omega t - h\alpha - \frac{h\mu}{2} - \frac{\pi}{2} - \frac{2h\pi}{3}) \\ \sin(h\omega t - h\alpha - \frac{h\mu}{2} - \frac{\pi}{2} + \frac{2h\pi}{3}) \end{bmatrix}, \ \forall\ h > 1 \tag{2.22}$$

Which gives us the following phase voltage amplitude and angle expressions for $h > 1$:

$$\begin{aligned} \widehat{V}_{br,h} &= \frac{4\omega L_s I_{dc} \cos(\frac{h\pi}{6}) \sin(\frac{h\pi}{2})^2 sinc(\frac{h\mu}{2})}{\pi}, \ \forall \ h > 1 \\ \angle V_{br,h} &= -h\alpha - \frac{h\mu}{2} - \frac{\pi}{2}, \ \forall \ h > 1 \end{aligned} \tag{2.23}$$

The fundamental wave of phase A at the input bridge voltage is written:

$$V_{br,a,fund} = V_s \sin(\omega t) - \frac{4\omega L_s I_{dc} \cos(\frac{\pi}{6}) \sin(\frac{\pi}{2})^2 sinc(\frac{\mu}{2})}{\pi} \sin\left(\omega t - \alpha - \frac{\mu}{2} + \frac{\pi}{2}\right)$$

And reduces to:

$$V_{br,a,fund} = \sqrt{V_s^2 + V_{L,1}^2 - 2V_s V_{L,1} \sin(\alpha + \mu/2)} \sin(\omega t + \phi_{br,1}) \tag{2.24}$$

Where:

$$\begin{aligned} V_{L,1} &= \frac{2\sqrt{3}\omega L_s I_{dc} sinc(\mu/2)}{\pi} \\ \phi_{br,1} &= atan\left(\frac{V_{L,1} \sin(\alpha + \mu/2) - V_s}{V_{L,1} \cos(\alpha + \mu/2)}\right) \end{aligned}$$

Note that the amplitude equation has been expressed in terms of the well-known $sinc(x)$ function, which describes very well the visual appearance of the amplitude modulation introduced by the voltage notch width on the spectrum. All the frequencies that are multiples of $h\mu = 2\pi n$ will be cut out of the spectrum, meaning that every time the $h\mu$ product is equal to a multiple of 2π, the harmonic will be cancelled. We can also understand from this that the modulation has more and more effects as the voltage notches widen. To better visualize this effect, figure 2.8 below shows the modulation curve for different notch width angles.

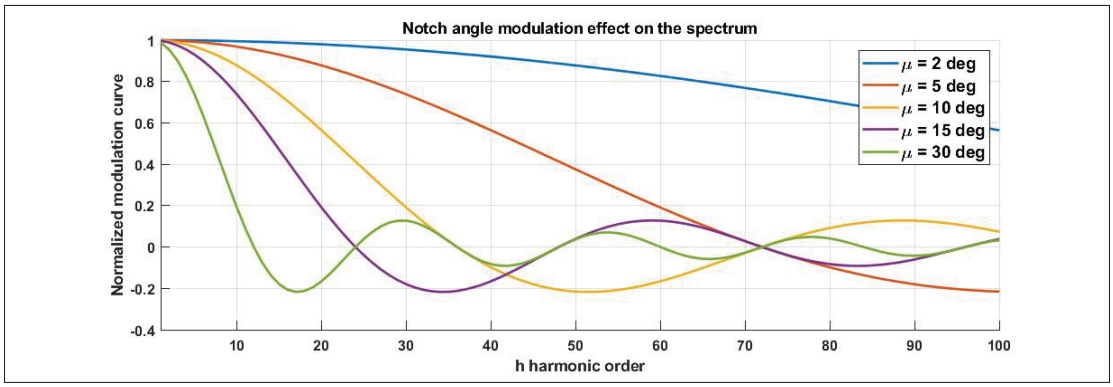

Figure 2.8 Voltage notch width modulation curves for different notch angles

As the notch angle is lowered, its modulation effects on the spectrum would tend to disappear. However, the modulation effects rapidly take effects as the notches widen.

Now consider the two normalized function derived from equation 2.23, $x_1(h) = \cos(\frac{h\pi}{2})\sin(\frac{h\pi}{2})^2$ and $x_2(h) = sinc(\frac{h\mu}{2})$. While $x_1(h)$ is considered as the basic modulated signal, $x_2(h)$ is the modulating signal. Figure 2.9 shows an example of the functions superposed for a notch width angle of 15 degrees.

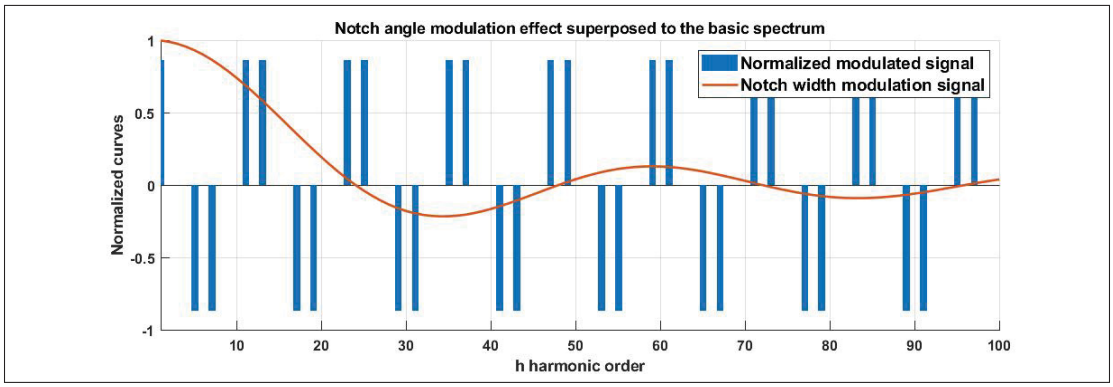

Figure 2.9 Normalized notch angle modulating curve superposed to the normalized modulated basic spectrum for a notch angle of 15 degrees

Note that the first four harmonics present in the spectrum are $h = 5,\ 7,\ 11,\ 13$. Then, by taking the absolute value of the $x_1(h)$ function and applying the $x_2(h)$ modulation to it, we get the following spectrum example:

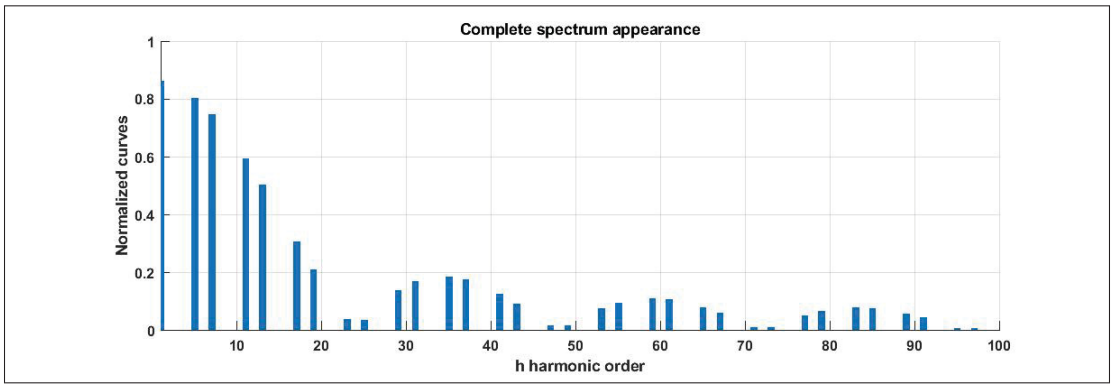

Figure 2.10 Complete normalized spectrum appearance for a notch angle of 15 degrees

The parameters V_s, L_s, μ, I_{dc} and α need to be known for the Fourier analysis to be completed correctly. The $\mathbf{V}_{br,abc}$ Fourier analysis is verified by matching those parameters with a simulation file, and then the curves can be matched to see how they fit. The parameters used for the simulation file are: $L_s = 5$ mH, $I_{dc}(av) = 2$ A, $V_s = 25$ V, $\alpha = \pi/6$ rad, and μ is calculated by using the equation 2.20. Figures 2.11, 2.12 and 2.13 show the comparison of the Fourier-reconstructed wave-form with the simulation curves by using the first 100 harmonic n orders.

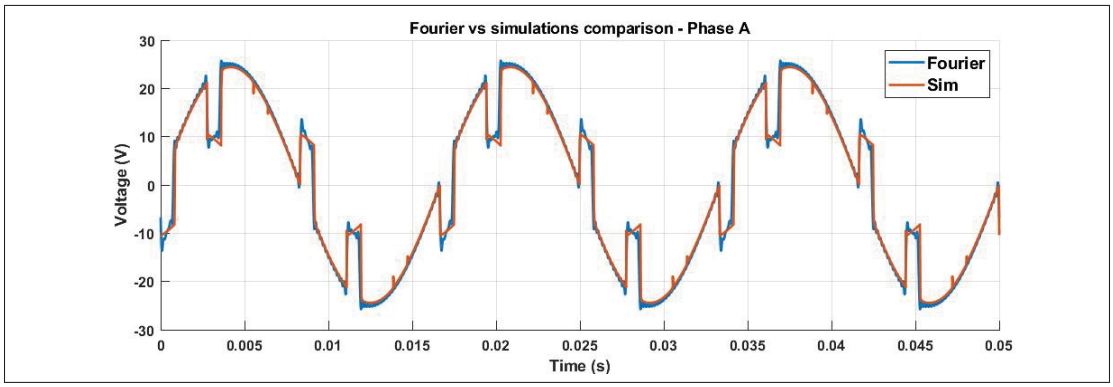

Figure 2.11 Fourier analysis comparison with simulation file - Phase A

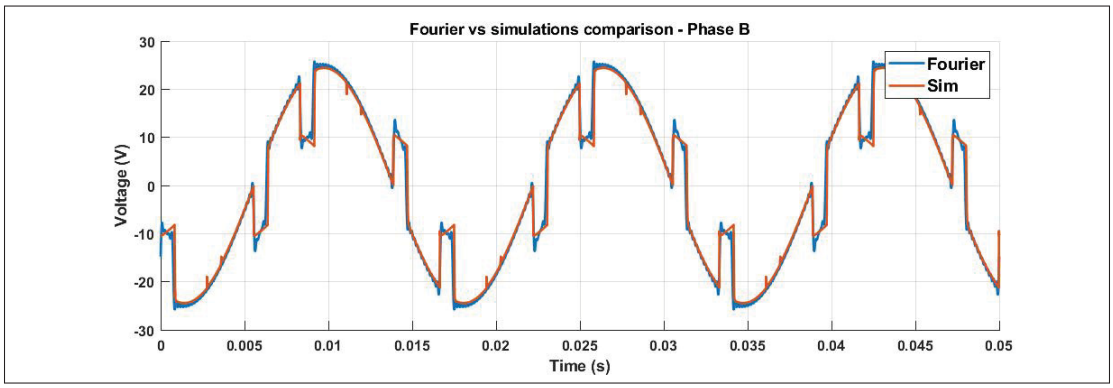

Figure 2.12 Fourier analysis comparison with simulation file - Phase B

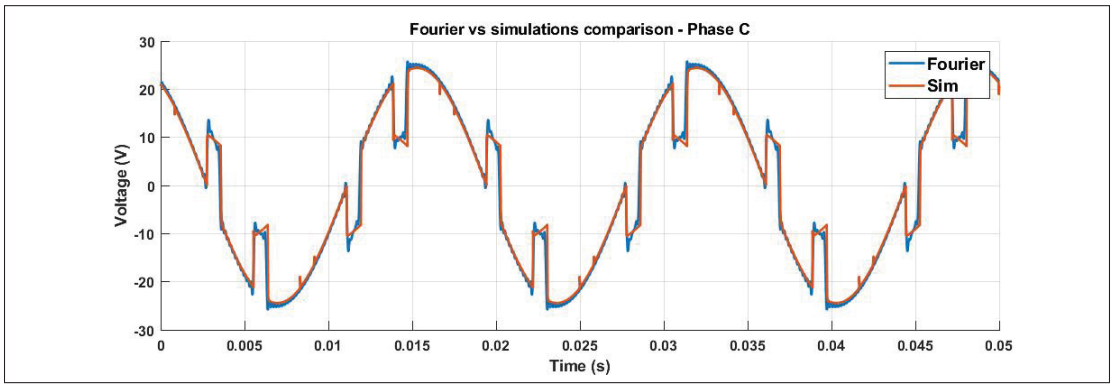

Figure 2.13 Fourier analysis comparison with simulation file - Phase C

By using the same parameters as the ones used for figures (2.11-2.13), we compare the FFT spectrum recovered from the simulations with the harmonics amplitudes calculated with the discussed method.

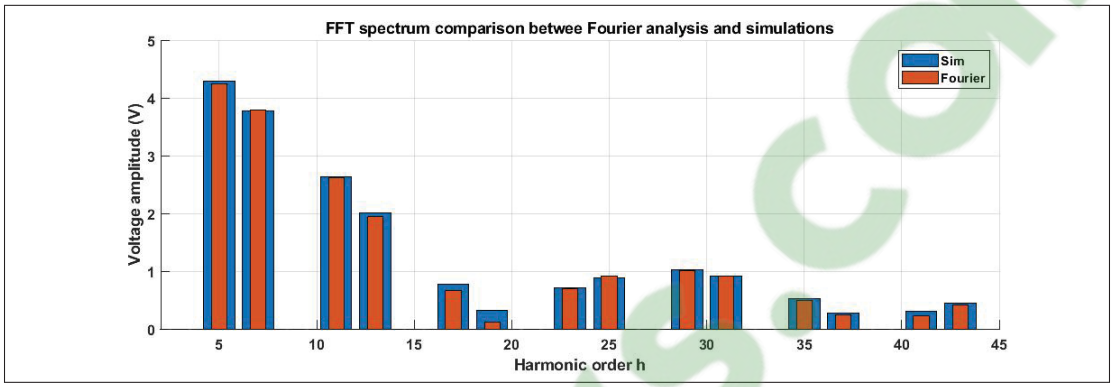

Figure 2.14 FFT spectrum comparison between Fourier analysis and simulation model recorded data

The Fourier analysis is clearly able to reconstruct the frequency spectrum of the bridge input voltage, though the notch angle calculation may be a little bit off since the $\mathrm{sinc}(x)$ function modulation looks shifted in the frequency spectrum by a small amount.

2.5.1 Conclusions on thyristor-based six-pulse rectifier bridge theory

In this chapter, the assumptions needed for excitation system modeling have been presented. The switching behavior of the bridge has been explained, leading to a switching function obtained by Fourier analysis done on the line currents, giving the equivalent transformer ratio used for steady-state equations of the rectifier bridge under ideal conditions. Next, effects of line inductance has been discussed thoroughly, and a Fourier analysis validated by simulations has been done on input line currents and phase voltages. It has been discovered that the frequency spectrum of the line currents and phase voltages are modulated by a cardinal sine factor. This Fourier analysis is to be ultimately used to define the input signals of the synchronization system that needs to be designed. But since one of the synchronization system is based on Park's

reference frame theory, the obtained Fourier analysis has to be transferred into the synchronous reference frame, which is the subject of the next chapter.

CHAPTER 3

THE PARK'S TRANSFORM - SYNCHRONOUS REFERENCE FRAME

The Park's transform uses a phase reference provided by a synchronization device to produce a rotating reference frame that transforms three-phase signals into three constant signals under some specific conditions. The main utility of the transform is for control systems since having constant values largely simplify control problems. The transform allows to transpose the equations of a three-phase systems into three equations that can each be represented as DC circuits as well. We will see that Park's theory can also be used to build phase-locked loops, as the transform can be used in phase detector devices. However, there are some limits to this type of phase detectors, which will be discussed in the Chapter 4.

3.1 Definition of the Park's transform matrix

The transformation matrix as given by Krause (2002) applied to three-phase signals gives qd0-frame signals as:

$$\begin{bmatrix} f_q \\ f_d \\ f_0 \end{bmatrix} = \mathbf{K}_s \begin{bmatrix} f_a \\ f_b \\ f_c \end{bmatrix}$$

Where the definition of the transformation matrix $\mathbf{K}_s$ is:

$$\mathbf{K}_s = \frac{2}{3} \begin{bmatrix} \cos\left(\theta(t)\right) & \cos\left(\theta(t) - \frac{2\pi}{3}\right) & \cos\left(\theta(t) + \frac{2\pi}{3}\right) \\ \sin\left(\theta(t)\right) & \sin\left(\theta(t) - \frac{2\pi}{3}\right) & \sin\left(\theta(t) + \frac{2\pi}{3}\right) \\ 1/2 & 1/2 & 1/2 \end{bmatrix} \tag{3.1}$$

And the inverse transformation:

$$\begin{bmatrix} f_a \\ f_b \\ f_c \end{bmatrix} = \mathbf{K}_s^{-1} \begin{bmatrix} f_q \\ f_d \\ f_0 \end{bmatrix}$$

Where the inverse transform matrix $\mathbf{K}_s^{-1}$ is defined:

$$\mathbf{K}_s^{-1} = \begin{bmatrix} \cos\left(\theta(t)\right) & \sin\left(\theta(t)\right) & 1 \\ \cos\left(\theta(t) - 2\pi/3\right) & \sin\left(\theta(t) - 2\pi/3\right) & 1 \\ \cos\left(\theta(t) + 2\pi/3\right) & \sin\left(\theta(t) + 2\pi/3\right) & 1 \end{bmatrix} \tag{3.2}$$

Note that if the angle provided to the Park's transform is constant at a null value, the obtained transformation matrix is the same as the Clarke's transform matrix. Also, the angle $\theta(t)$ varies over time, and could be expressed as $\omega_r t + \delta_r$, where ω_r is the angular frequency, and δ_r is the initial angle of the reference frame.

3.2 Expressing parameters into the Park's referential frame

The present section explains in detail what happens when three-phase values are observed through the qd-frame, even when the three-phase signals are unbalanced and polluted with harmonics. The main goal of this section is to understand the properties of the transform to transfer the result of the Fourier analysis obtained in the previous chapter to characterize properly the input signals of the synchronization system built in qd-frame.

3.2.1 Observed parameters under unbalanced three-phase signal conditions

Consider the set of three-phase signals which may be balanced or unbalanced expressed into symmetrical components:

$$\mathbf{f}_{abc} = \begin{bmatrix} f_a \\ f_b \\ f_c \end{bmatrix} = A_p \begin{bmatrix} \sin(\omega t + \delta_p) \\ \sin(\omega t + \delta_p - 2\pi/3) \\ \sin(\omega t + \delta_p + 2\pi/3) \end{bmatrix} + A_n \begin{bmatrix} \sin(\omega t + \delta_n) \\ \sin(\omega t + \delta_n + 2\pi/3) \\ \sin(\omega t + \delta_n - 2\pi/3) \end{bmatrix} + A_z \begin{bmatrix} \sin(\omega t + \delta_z) \\ \sin(\omega t + \delta_z) \\ \sin(\omega t + \delta_z) \end{bmatrix}$$

Where we define the parameters:

- A_p as the amplitude of the positive sequence signal.
- δ_p as the initial phase angle of the positive sequence signal.
- A_n as the amplitude of the negative sequence signal.
- δ_n as the initial phase angle of the negative sequence signal.
- A_z as the amplitude of the zero sequence signal.
- δ_z as the initial phase angle of the zero sequence signal.

By multiplying the signals $\mathbf{f}_{abc}$ by the transformation matrix K_s where we substitute the reference angle $\theta(t)$ by $\omega_r t + \delta_r$ we find:

$$\begin{bmatrix} f_q \\ f_d \\ f_0 \end{bmatrix} = \begin{bmatrix} A_p \sin((\omega - \omega_r)t + \delta_p - \delta_r) + A_n \sin((\omega + \omega_r)t + \delta_n + \delta_r) \\ A_p \cos((\omega - \omega_r)t + \delta_p - \delta_r) - A_n \cos((\omega + \omega_r)t + \delta_n + \delta_r) \\ A_z \sin(\omega t + \delta_z) \end{bmatrix}$$

Now if the PLL is considered locked on the input signal frequency, we find:

$$\begin{bmatrix} f_q \\ f_d \\ f_0 \end{bmatrix} = \begin{bmatrix} A_p \sin(\delta_p - \delta_r) + A_n \sin(2\omega t + \delta_n + \delta_r) \\ A_p \cos(\delta_p - \delta_r) - A_n \cos(2\omega t + \delta_n + \delta_r) \\ A_z \sin(\omega t + \delta_z) \end{bmatrix} \tag{3.3}$$

Equation (6.1) tells us that the positive sequence creates DC signals only, and the negative sequence of an unbalanced signal produces ripple at twice the grid's frequency. If the signal is balanced, meaning that the negative and zero sequences are absent in the $\mathbf{f}_{abc}$ signals, we find:

$$\begin{bmatrix} f_q \\ f_d \\ f_0 \end{bmatrix} = \begin{bmatrix} A_p \sin(\delta_p - \delta_r) \\ A_p \cos(\delta_p - \delta_r) \\ 0 \end{bmatrix} \tag{3.4}$$

If the signal $\mathbf{f}_{abc}$ is balanced, but the PLL is not locked on the grid's frequency yet, we find:

$$\begin{bmatrix} f_q \\ f_d \\ f_0 \end{bmatrix} = \begin{bmatrix} A_p \sin((\omega - \omega_r)t + \delta_p - \delta_r) \\ A_p \cos((\omega - \omega_r)t + \delta_p - \delta_r) \\ 0 \end{bmatrix} \tag{3.5}$$

Equation (3.5) shows that if the PLL is not locked on the frequency of the signal, the qd0 signals will have a pulsating component at the frequency error of the PLL.

3.2.2 Observed parameters for a three-phase positive-sequence signal with harmonics

Here, we wish to isolate the behavior of the transform while there are harmonics on the three-phase signal, so we consider the input signals to be perfectly balanced. Also, we consider the angle reference signal for the transform to be representing the angle of the fundamental of the three-phase signal. To represent the three-phase signal harmonics, we write the transform's input signal as:

$$\mathbf{V}_{abc,h} = A_h \begin{bmatrix} \sin(h\omega t + \delta_h) \\ \sin(h\omega t + \delta_h - 2h\pi/3) \\ \sin(h\omega t + \delta_h + 2h\pi/3) \end{bmatrix} \tag{3.6}$$

By transferring this signal into qd-frame by multiplying $\mathbf{V}_{qd0,h} = \mathbf{K}_s \mathbf{V}_{abc,h}$ and expressing the harmonic terms for every harmonic order up to 7, we get the terms expressed in table 3.1.

Table 3.1 qd-frame harmonics expressions

h order	**q-axis**	**d-axis**	**0-axis**
1	$A_1 \sin(\delta_1)$	$A_1 \cos(\delta_1)$	0
2	$A_2 \sin(3\omega t + \delta_2)$	$-A_2 \cos(3\omega t + \delta_2)$	0
3	0	0	$A_3 \sin(3\omega t + \delta_3)$
4	$A_4 \sin(3\omega t + \delta_4)$	$A_4 \cos(3\omega t + \delta_4)$	0
5	$A_5 \sin(6\omega t + \delta_5)$	$-A_5 \cos(6\omega t + \delta_5)$	0
6	0	0	$A_6 \sin(6\omega t + \delta_6)$
7	$A_7 \sin(6\omega t + \delta_7)$	$A_7 \cos(6\omega t + \delta_7)$	0

The harmonic terms are written as sums, where the $3k = h$, and h is the order of the qd-frame transform input signal harmonic orders. The use of k subscript is to emphasis on the facts that the recurring pattern happens every third harmonics, and that the frequencies seen in qd-frame are always multiples of 3 of the grid's frequency.

$$
\begin{aligned}
V_q &= \sum_{k=1}^{\infty} \left(A_{(3k-1)} \sin(3k\omega t + \delta_{(3k-1)}) + A_{(3k+1)} \sin(3k\omega t + \delta_{(3k+1)}) \right) \\
V_d &= \sum_{k=1}^{\infty} \left(-A_{(3k-1)} \cos(3k\omega t + \delta_{(3k-1)}) + A_{(3k+1)} \cos(3k\omega t + \delta_{(3k+1)}) \right) \\
V_0 &= \sum_{k=1}^{\infty} \left(A_{(3k)} \sin(3k\omega t + \delta_{(3k)}) \right)
\end{aligned}
\tag{3.7}
$$

The expressions can also be rewritten to be able to quickly find the amplitude and phase angle of the components observed in qd-frame at a specific frequency.

$$\begin{bmatrix} V_q \\ V_d \\ V_0 \end{bmatrix} = \begin{bmatrix} \sqrt{A_{h-1}^2 + A_{h+1}^2 + 2A_{h-1}A_{h+1}\cos(\delta_{h-1} - \delta_{h+1})}\ \sin\left(h\omega t + \phi_q\right) \\ \sqrt{A_{h-1}^2 + A_{h+1}^2 - 2A_{h-1}A_{h+1}\cos(\delta_{h-1} - \delta_{h+1})}\ \sin\left(h\omega t + \phi_d\right) \\ A_h \sin\left(h\omega t + \phi_0\right) \end{bmatrix},\ h = \{3, 6, 9, ...\} \tag{3.8}$$

Where:

$$\begin{aligned} \phi_q &= \tan^{-1}\left(\frac{A_{h-1}\cos(\delta_{h-1}) + A_{h+1}\cos(\delta_{h+1})}{A_{h-1}\sin(\delta_{h-1}) + A_{h+1}\sin(\delta_{h+1})}\right) \\ \phi_d &= \tan^{-1}\left(\frac{A_{h-1}\sin(\delta_{h-1}) - A_{h+1}\sin(\delta_{h+1})}{-A_{h-1}\cos(\delta_{h-1}) + A_{h+1}\cos(\delta_{h+1})}\right) \\ \phi_0 &= \delta_0 \end{aligned} \tag{3.9}$$

The qd-frame signals expressed in equation (3.8) are both expressed as sine terms, but if the phase angles ϕ_q and ϕ_d are lagging each other by $\pi/2$, one of them will become cosine.

3.2.3 Observed parameters for a harmonics-polluted three-phase negative-sequence signal

Similarly to the previous section, we wish to isolate the behavior of the transform on the negative sequence harmonics. The three-phase negative-sequence signal containing harmonics is written:

$$\mathbf{V}_{abc,h} = A_h \begin{bmatrix} \sin(h\omega t + \delta_h) \\ \sin(h\omega t + \delta_h + 2h\pi/3) \\ \sin(h\omega t + \delta_h - 2h\pi/3) \end{bmatrix}$$

By writing the qd-frame values $\mathbf{V}_{qd0,h} = \mathbf{K}_s\mathbf{V}_{abc,h}$, and simplifying the obtained expressions for every harmonic orders up to 8, we get the terms expressed in table 3.2.

Table 3.2 qd-frame harmonics expressions for a negative sequence three-phase signal

h order	**q-axis**	**d-axis**	**0-axis**
1	$A_1 \sin(2\omega t + \delta_1)$	- $A_1 \cos(2\omega t + \delta_1)$	0
2	$A_2 \sin(\omega t + \delta_2)$	$A_2 \cos(\omega t + \delta_2)$	0
3	0	0	$A_3 \sin(3\omega t + \delta_3)$
4	$A_4 \sin(5\omega t + \delta_4)$	$-A_4 \cos(5\omega t + \delta_4)$	0
5	$A_5 \sin(4\omega t + \delta_5)$	$A_5 \cos(4\omega t + \delta_5)$	0
6	0	0	$A_6 \sin(6\omega t + \delta_6)$
7	$A_7 \sin(8\omega t + \delta_7)$	$-A_7 \cos(8\omega t + \delta_7)$	0
8	$A_8 \sin(7\omega t + \delta_8)$	$A_8 \cos(7\omega t + \delta_8)$	0

We find the recurring pattern to build the general term, and express the harmonic spectrum as an infinite sum:

$$
\begin{aligned}
V_q &= \sum_{k=1}^{\infty} \left(A_{(3k-2)} \sin((3k-1)\omega t + \delta_{(3k-2)}) + A_{(3k-1)} \sin((3k-2)\omega t + \delta_{(3k-1)}) \right) \\
V_d &= \sum_{k=1}^{\infty} \left(-A_{(3k-2)} \cos((3k-1)\omega t + \delta_{(3k-2)}) + A_{(3k-1)} \cos((3k-2)\omega t + \delta_{(3k-1)}) \right) \\
V_0 &= \sum_{k=1}^{\infty} \left(A_{(3k)} \sin(3k\omega t + \delta_{(3k)}) \right)
\end{aligned}
\tag{3.10}
$$

The harmonic terms can also be expressed:

$$
\begin{aligned}
&V_{q,h} = A_{h-1}\sin(h\omega t + \delta_{h-1}),\ \forall\ \{h = 3k-1 | k \in \mathbb{N}\}\ \cup\ A_{h+1}\sin(h\omega t + \delta_{h+1}),\\
&\forall\ \{h = 3k-2 | k \in \mathbb{N}\}\\
&V_{d,h} = -A_{h-1}\cos(h\omega t + \delta_{h-1}),\ \forall\ \{h = 3k-1 | k \in \mathbb{N}\}\ \cup\ A_{h+1}\cos(h\omega t + \delta_{h+1}),\\
&\forall\ \{h = 3k-2 | k \in \mathbb{N}\}\\
&V_{0,h} = A_h\sin(h\omega t + \delta_h),\ \forall\ \{h = 3k | k \in \mathbb{N}\}
\end{aligned}
\tag{3.11}
$$

Equation (3.11) expresses the signals with union signs, which tells that if the frequency of the signal in qd-frame is of harmonic order $\{h = 3k-1 | k \in \mathbb{N}\}$, the left-hand side equation has to be used, and it is of order $\{h = 3k-2 | k \in \mathbb{N}\}$, the right-hand side expression should be used instead. Note that in contrast with the positive sequence signal harmonics, the negative sequence cuts all frequencies that are of multiples of 3 of the grid's frequency out of the qd axis.

3.2.4 Inverse transform properties

The inverse transform also has specific properties, as we will see in this section. Transferring back qd-frame signals into abc-frame may produce negative sequence or harmonics (or both), depending on the characteristics of the qd-frame signals. In this research, the inverse transform is used for the three-phase source signal production in the simulation files to inject a negative sequence on the source voltage to match the experimental data recorded in the laboratory. To make sure that the input qd-frame signals inject negative sequence and no harmonics in the source voltage, certain conditions have to be respected. Now, consider the following qd-frame signal:

$$\mathbf{V}_{qd0} = \begin{bmatrix} V_q \\ V_d \\ V_0 \end{bmatrix} = \begin{bmatrix} A_q + B_q \sin(h\omega t + \delta_q) \\ A_d + B_d \sin(h\omega t + \delta_d) \\ 0 \end{bmatrix} \tag{3.12}$$

By applying the inverse transform:

$$\mathbf{V}_{abc} = \mathbf{K}_s^{-1}\mathbf{V}_{qd0}$$

And using the arbitrary reference angle $\theta(t) = \omega t + \delta_r$ as a signal reference for the transform matrix, we obtain:

$$\begin{aligned} \mathbf{V}_{abc} = A_p \begin{bmatrix} \sin(\omega t + \phi_p) \\ \sin(\omega t + \phi_p - 2\pi/3) \\ \sin(\omega t + \phi_p + 2\pi/3) \end{bmatrix} + A_h \begin{bmatrix} \sin((h+1)\omega t + \phi_h) \\ \sin((h+1)\omega t + \phi_h - 2\pi/3) \\ \sin((h+1)\omega t + \phi_h + 2\pi/3) \end{bmatrix} \\ + A_n \begin{bmatrix} \sin((h-1)\omega t + \phi_n) \\ \sin((h-1)\omega t + \phi_n + 2\pi/3) \\ \sin((h-1)\omega t + \phi_n - 2\pi/3) \end{bmatrix} \end{aligned} \tag{3.13}$$

Where the amplitudes are:

$$\begin{aligned} A_p &= \sqrt{A_q^2 + A_d^2} \\ A_h &= \sqrt{B_q^2 + B_d^2 - 2B_qB_d \sin(\delta_q - \delta_d)} \\ A_n &= \sqrt{B_q^2 + B_d^2 + 2B_qB_d \sin(\delta_q - \delta_d)} \end{aligned} \tag{3.14}$$

And the phase angles:

$$\phi_p = \tan^{-1}\left(\frac{A_d}{A_q}\right) + \delta_r$$
$$\phi_h = \tan^{-1}\left(\frac{B_q cos(\delta_q) + B_d \sin(\delta_d)}{B_q sin(\delta_q) - B_d \cos(\delta_d)}\right) + \delta_r$$
$$\phi_n = \tan^{-1}\left(\frac{B_q cos(\delta_q) - B_d \sin(\delta_d)}{B_q sin(\delta_q) + B_d \cos(\delta_d)}\right) + \delta_r$$

By looking at equation (3.13), we understand that the DC signals in qd-frame will always give a perfectly balanced three-phase signal. However, the sinusoidal signals in qd-frame of arbitrary harmonic frequency will create two more periodic signals. One of them has a negative sequence, and is one harmonic order lower than the signal in qd-frame. The other is in positive sequence, and has a frequency of one order above the signal in qd-frame. With equation (3.14), notice that the amplitudes of the harmonic signals A_h and A_n can be canceled out if some conditions apply. In order to have no harmonics in the abc-frame signal, the following conditions have to be respected:

$$\begin{aligned} B_q &= B_d \\ \delta_q &= \delta_d + \pi/2 \end{aligned} \tag{3.15}$$

To cancel out the negative sequence in the abc-frame signals, the conditions are:

$$\begin{aligned} B_q &= B_d \\ \delta_d &= \delta_q + \pi/2 \end{aligned} \tag{3.16}$$

If none of those conditions are respected, both negative and positive sequence harmonic signals will be injected in the abc-frame. Note that the conditions expressed in equations (3.15) and (3.16) are exclusive to each other. It means that only one of the signals (negative-sequence harmonic or positive-sequence harmonic) can be canceled at a certain time. In the future model

simulation files, it will be necessary to inject a negative sequence in the three-phase source a the grid's frequency. To do so, we now understand that we need to have sinusoidal signals of same amplitude at twice the grid's frequency that lag each other by 90 degrees ($\delta_q = \delta_d + \pi/2$).

3.3 Power expressed into Park's referential

As will be shown in this section, it is often required to express the power entering and going out of an electronic converter to build an averaged model. We will later assume that the power going into the DC bus of the rectifier bridge is equal to the power input on the three-phase side. Knowing that power can be expressed as shown below for a three-phase system:

$$P = e_a i_a + e_b i_b + e_c i_c \tag{3.17}$$

Assuming the three-phase voltage to be expressed:

$$\mathbf{V}_{abc} = \begin{bmatrix} e_a & e_b & e_c \end{bmatrix}^T$$

And the current to be expressed:

$$\mathbf{I}_{abc} = \begin{bmatrix} i_a & i_b & i_c \end{bmatrix}^T$$

We may now write the power in the matrix product form:

$$P = \mathbf{V}_{abc}{}^T \mathbf{I}_{abc} \tag{3.18}$$

We express the power into qd-frame:

$$
\begin{aligned}
P &= (\mathbf{K}_s^{-1}\mathbf{V}_{qd0})^T\mathbf{K}_s^{-1}\mathbf{I}_{qd0} \\
&= V_d i_d(\cos(\theta(t))^2 + \cos(\theta(t) - 2\pi/3)^2 + \cos(\theta(t) + 2\pi/3)^2) \\
&+ V_q i_q(\sin(\theta(t))^2 + \sin(\theta(t) - 2\pi/3)^2 + \sin(\theta(t) + 2\pi/3)^2) + 3V_0 i_0
\end{aligned}
$$

Which reduces to:

$$P = \frac{3}{2}(V_d i_d + V_q i_q + 2V_0 i_0) \tag{3.19}$$

If homopolar sequence is neglected, the power equation can be simplified to:

$$P = \frac{3}{2}(V_d i_d + V_q i_q) \tag{3.20}$$

3.4 Conclusions on synchronous reference frame transform

In this chapter, the Park transform has been introduced and explained. Then, it has been discovered that the transform in itself has some properties affecting the frequency spectrum of its input signals, depending on if the input signal is positive sequence or negative sequence, and if it contains harmonics or not. The properties of the transform on an arbitrary signal were discussed, and the result of the Fourier analysis for the input signals of the synchronization systems can be transferred to the synchronous reference frame for an accurate characterization. The resulting expressions will be used to design one of the synchronization systems of this research, which is the subject of the next chapter.

CHAPTER 4

SYNCHRONIZATION DEVICES

In this chapter, two types of Phase-Locked Loop will be designed and compared and some recommendations will be made regarding synchronization techniques for excitation systems. The first PLL called qd0-PLL uses a Single-Input Single-Output (SISO) approach and uses the Park transform as phase detector. The second PLL called Unified Three-phase Signal Processor (UTSP) is based on a Multiple-Input Multiple-Output (MIMO) approach, and is naturally robust to noise and negative sequence three-phase inputs.

The qd-frame PLL design method will start without filter, then order 1 and 2 filters will be introduced. That way, one's understanding of the root-locus will gradually follow the increasing complexity, instead of being thrown directly into the finished design. The UTSP model used is a simplified and modified version introduced by Karimi H. (2019).

But first, to be able to design the synchronization systems, their input signals have to be characterized correctly to achieve the correct tuning. If the system is out of tune relative to the expected input signals, the estimated values will contain oscillatory components that are way beyond what can be used as phase-angle reference to a control system.

4.1 Synchronization systems input voltage input signals

The expected behavior of the synchronization systems is to first read a three-phase signal, and recover their correct amplitude, frequency and phase angle with precision. In theory, if the signal input has no harmonics and is perfectly balanced, building a tuning that will work well is quite straightforward. However, the synchronization systems may have to be able to give the correct estimations even if the harmonics content is aggressive, or if the grid is unbalanced. The bridge input phase voltage harmonics content due to voltage notches has been discussed in a previous section 2.5, and this voltage waveform will be used to test PLLs.

4.1.1 Input signals characterization of the UTSP

The expected harmonics content on the input bridge voltage has already been developed and validated in chapter 2, and a frequency spectrum example is given in figure 2.14. We expect the first harmonics to appear at 300 Hz (harmonic order 5). We then at least know that the eigenvalues of the UTSP have to be positioned at lower frequency than 300 Hz.

4.1.2 Input signals characterization of the qd-frame PLL

Using voltage harmonic described in equation (2.23), and substituting into qd-frame harmonic terms equation (3.8), we calculate the harmonic amplitudes seen in qd-frame. Figures 4.1 and 4.2 show the comparison between the computed terms, and the results of simulations using the same parameters as for the results obtained in figure 2.14.

As for the expected 120 Hz component coming from the negative sequence injected. First, the fundamental harmonic term of the positive sequence must be calculated with equation (2.24), then the voltage drop of the positive sequence, which is in turn applied to the negative sequence. One knows that the value must be added to both q and d axis at 120 Hz because it was previously determined that the oscillatory component coming from the negative sequence would appear on both axis, and have the same amplitude (but shifted by 90 degrees). The 120 Hz component is calculated:

$$V_{br,qd(120Hz)} = V_{s,p}\left(\frac{V_{s,n}}{V_{s,p}}\right)\left(\frac{\widehat{V}_{br,a,fund}}{V_{s,p}}\right) = \frac{V_{s,n}\widehat{V}_{br,a,fund}}{V_{s,p}} \tag{4.1}$$

Since we inject 2 percent of negative sequence in the source voltage, we know the $V_{s,n}/V_{s,p}$ ratio is equal to 0.02.

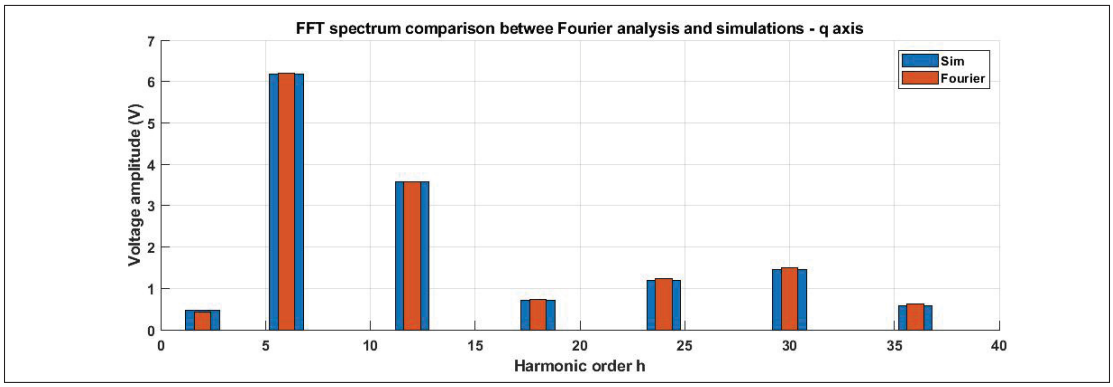

Figure 4.1 Input bridge voltage harmonic amplitudes comparison between Fourier and Simulations for q-axis

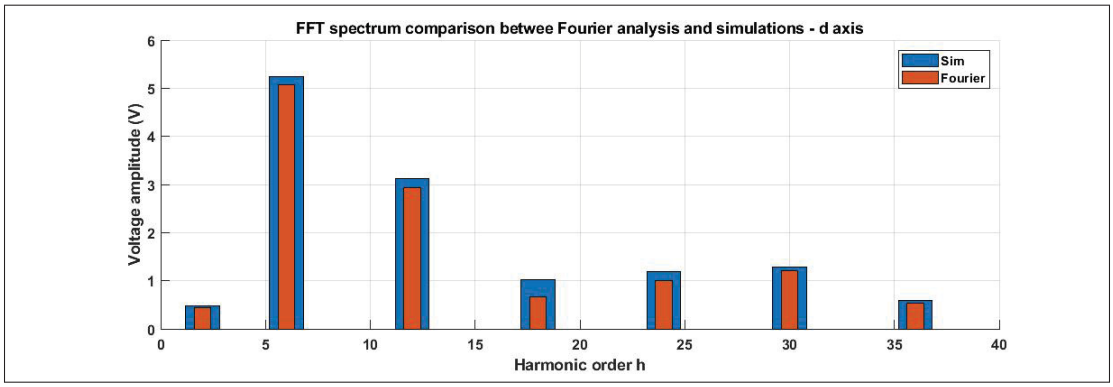

Figure 4.2 Input bridge voltage harmonic amplitudes comparison between Fourier and Simulations for d-axis

4.2 qd0-PLL model derivation and design

The idea of the qd0-PLL is to use the fact that using the Park transform on a three-phase signal decomposes it into a component perfectly in phase and another completely out of phase as discussed previously in section 3.2. This section will show how to design this type of PLL by including a filter that will be used to filter line voltage notches created by the rectifier bridge. The design will first be shown without a filter, then a first order low-pass filter will be added,

followed by a second order low-pass filter. As expected, we will see that the complexity of the design increases with the order of the filter increasing.

4.2.1 Mathematical model derivation of the qd0-PLL

Figure 4.3 is a block diagram representing the structure of the qd-frame PLL.

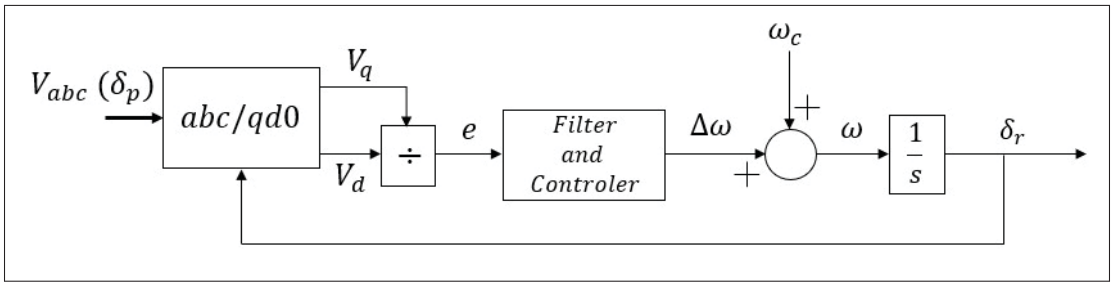

Figure 4.3 Block diagram of the qd0-PLL

To design the qd-PLL, we must first derive its mathematical model. To do so, we assume that the PLL is in locked state, and we recall the output of the Park transform to a balanced signal of sinusoidal origin being:

$$\begin{bmatrix} f_q \\ f_d \\ f_0 \end{bmatrix} = \begin{bmatrix} A_p sin(\delta_p - \delta_r) \\ A_p cos(\delta_p - \delta_r) \\ 0 \end{bmatrix}$$

Next, we assume that the angle error is very small. By assuming $\delta_p - \delta_r = \delta_e \approx 0$, which leads to $sin(\delta_e) \approx \delta_e$ we find that $f_q \approx A_p \delta_e$, and $f_d \approx A_p$. As shown on figure 4.3, the error signal going into the controller and filter is the component out of phase divided by the component in phase. Doing this cancels out the effect on the amplitude of the three-phase signal on the dynamic of the system. The PLL can be built without the amplitude normalization, but the

closed-loop poles would move on the root-locus as the amplitude changes because amplitude is seen as a gain entering the loop. The error signal in figure 4.3 then becomes:

$$e = \frac{f_q}{f_d} \approx \frac{A_p \delta_e}{A_p} = \delta_e$$

it is stated in Best (2003) that the transfer function of the PLL without the controller or filter is $1/s$, as the oscillator's transfer function is already assumed to be of the form $1/s$. The bloc diagram of the mathematical model of the qd0-PLL is then:

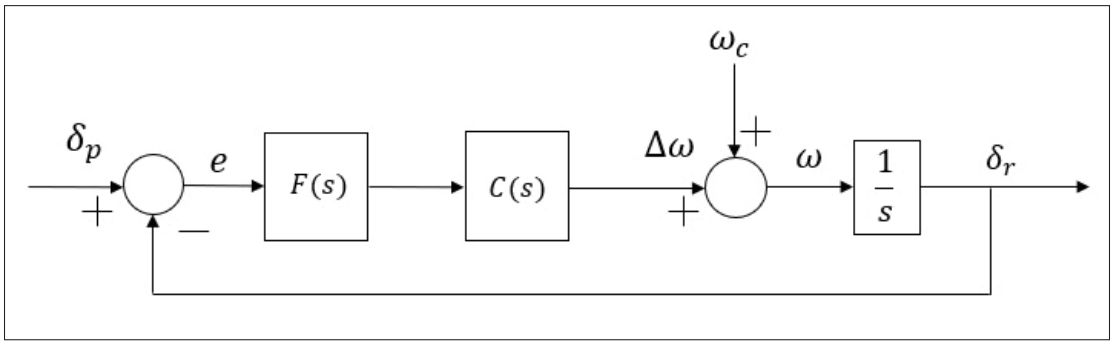

Figure 4.4 Mathematical model of the qd0-PLL

And the dynamic of the PLL is governed by the open-loop transfer function:

$$H(s) = \frac{F(s)C(s)}{s} \tag{4.2}$$

The controller used will be a Proportional-Integral (PI) controller, which has the transfer function:

$$C(s) = k_p + \frac{k_i}{s} = k_p \frac{\left(s + \frac{k_i}{k_p}\right)}{s} \tag{4.3}$$

As stated before, the filter's transfer function used in this research will first be unitary, then of the first order form:

$$F_1(s) = \frac{\omega_f}{s + \omega_f}$$

The second order filter's transfer function is:

$$F_2(s) = \frac{\omega_f^2}{s^2 + 2\xi\omega_f s + \omega_f^2}$$

4.2.2 Root-locus drawing of the qd0-PLL

To draw the root-locus of the qd0-PLL, some basic rules must first be recalled. The closed-loop transfer function form used for root-locus drawing is defined as:

$$G(s) = \frac{KH(s)}{1 + KH(s)} \tag{4.4}$$

Where $H(s)$ is the open-loop transfer function of unitary gain of the system. In our case, since we divided the error by the magnitude of the input signal, the gain of the system is only the gain of the controller, which is k_p. What must be understood from this is that the shape of the root-locus is governed by the position of the filter in respect to the position of the controller's zero (k_i/k_p). Then, the position of the closed-loop poles can be controlled via only the proportional gain k_p. We define the functions $N(s)$ and $D(s)$ as the numerator and denominator respectively of the open-loop transfer function $H(s)$, meaning that:

$$H(s) = \frac{N(s)}{D(s)}$$

The following rules are the ones to be remembered for the root-locus drawing process:

1. Root locus exists on the real axis only to the left of an odd number of poles and zeros.
2. The number of asymptotes N_a of the root-locus is expressed:

$$N_a = n_p - n_z \tag{4.5}$$

   Where n_p is the total number of poles of the transfer function $H(s)$, and n_z is the number of zeroes.
3. The origin of the asymptotic lines on the real axis is found with:

$$O_A = \frac{\sum p_i - \sum z_i}{N_a} \tag{4.6}$$

4. The angles of departure of the asymptotic lines on the real axis are expressed:

$$\theta_A = \frac{\pi(2k+1)}{N_a} \tag{4.7}$$

   Where $k = 0, 1, \ldots, (N_a - 1)$.
5. The intersection between the root-locus curves and the real axis can be found by finding the root values of the expression:

$$P(s) = N(s)D'(s) - N'(s)D(s) = 0 \tag{4.8}$$

6. The root locus starts on the open-loop poles at $K = 0$ and finishes on the open-loop zeroes at $K = \infty$.

For future development, the controller's zero will be referred to as k instead of $\frac{k_i}{k_p}$.

4.2.2.1 Root-locus drawing of the qd0-PLL without filter

To find the intersection points of the paths with the real axis, we define $N(s)$ and $D(s)$ as:

$$N(s) = s + k$$
$$D(s) = s^2 \tag{4.9}$$

Equation (4.10) gives the intersection points between the paths and the real axis.

$$P(s) = N(s)D'(s) - N'(s)D(s) = 0 \tag{4.10}$$

Where:

$$N'(s) = 1$$
$$D'(s) = 2s \tag{4.11}$$

Substituting in equation (4.10) yields:

$$P(s) = (s + k)(2s) - s^2 = s^2 + 2ks = 0$$

And intersection points are:

$$s_1 = 0$$
$$s_2 = -2k$$

Since there are two zeros at the origin, and the paths exist on the real axis only when an odd number of poles and zeros are present to the right, we deduce that the paths of the root locus must go in a circle of radius k, centered on the zero of the controller. The resulting root locus plot is shown on figure 4.5, where the red lines are the possible paths of the closed-loop poles, the blue "X" are the open-loop poles, and the blue "O" are the open-loop zeros.

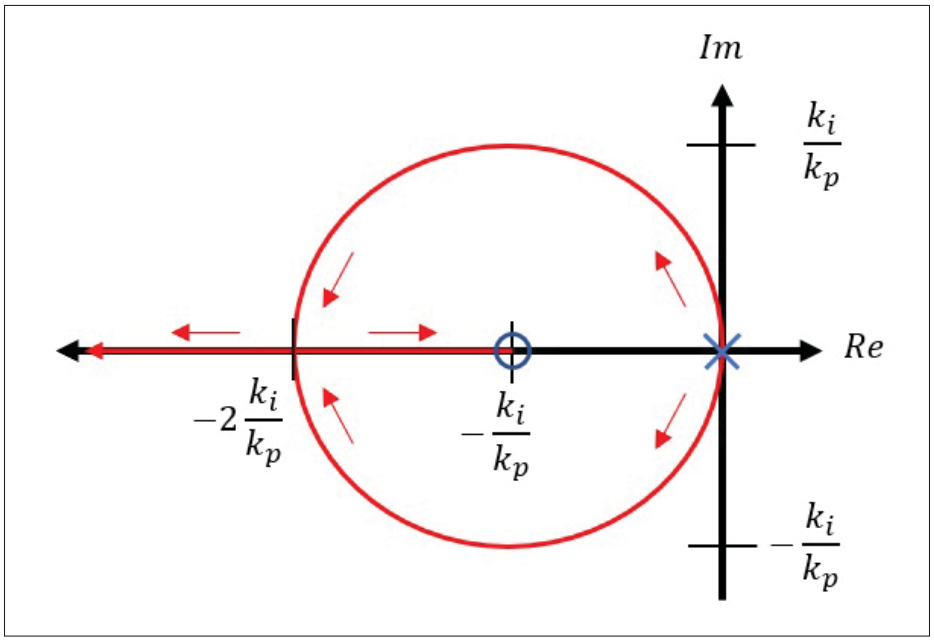

Figure 4.5 Root locus of the qd0 PLL without low-pass filter

4.2.2.2 Root-locus drawing of the qd0-PLL with first order low-pass filter

As said previously, as we move the zero of the controller in respect to the poles of the filter, the shape of the root-locus will change. There are some critical values that can be found mathematically with equation 4.10 that will be used to separate the possibles cases of root-locus shapes.

We find the intersection of the root-locus curves with the real axis by finding the roots of the function $P(s)$:

$$\begin{aligned} P(s) &= (s+k)(2s(s+\omega_f)+s^2) - s^2(s+\omega_f) \\ &= 2s^3 + (\omega_f + 3k)s^2 + 2k\omega_f s = 0 \end{aligned}$$

We then find the roots to be:

$$
\begin{aligned}
s_1 &= 0 \\
s_2 &= -\frac{\omega_f + 3k}{4} + \sqrt{\frac{(\omega_f + 3k)^2}{16} - k\omega_f} \\
s_3 &= -\frac{\omega_f + 3k}{4} - \sqrt{\frac{(\omega_f + 3k)^2}{16} - k\omega_f}
\end{aligned}
\tag{4.12}
$$

Consider the square-root term of equation (4.12) as the critical term. We separate 3 distinct cases as the filter poles approaches the controller's zero. Figure 4.6 shows a shape example of the root locus for each cases discussed.

Case 1:

If equation (4.12) respects the following inequality:

$$(T_d + 3k)^2 > 16kT_d$$

The root locus will have 3 distinct intersection points.

Case 2:

Now, if equation 4.12 respects:

$$(\omega_f + 3k)^2 - 16k\omega_f = 0$$

We write the roots of the cut-off frequency ω_f as a function of the zero:

$$\omega_{f_1} = k$$

$$\omega_{f_2} = 9k$$

If the cut-off frequency is 9 times the value of the zero, the two last intersection points defined in equation (4.12) will merge into a double root. The intersection points then become:

$$\begin{aligned} s_1 &= 0 \\ s_2 &= -\frac{\omega_f + 3k}{4} \\ s_3 &= -\frac{\omega_f + 3k}{4} \end{aligned} \tag{4.13}$$

Case 3:

If the cut-off frequency of the low-pass filter stands between the critical roots by respecting $k < \omega_f < 9k$, where:

$$(\omega_f + 3k)^2 < 16k\omega_f$$

Which means that the s_2 and s_3 roots defined in equation (4.12) are now invalid as there is an imaginary component to a position on the real axis. The only remaining solution of the intersection points is now $s_1 = 0$, and the root locus shape will instead reach to the asymptotes directly instead of intersecting the real axis first as in case 1 and case 2.

Moving the filter closer to the controller zero has no utility, as only cases 1 through 3 would result in a functional PLL design.

Figure 4.6 shows the root-locus of the cases 1 through 3 as the filter transfer function is maintained constant, and the zero of the controller is moved. The m value is used to denote how close the controller's zero is to the filter's pole, following the relation $\omega_f = mk$ where k is the value of the zero. Table 4.1 compiles the information on where the root locus curves hit the real axis as well as the position of the centroid O_A for 3 values of m.

Table 4.1 Values of real axis intersection and centroid for m values

m	s_1	s_2	s_3	O_A
10	0	$-0.25\omega_f$	$-0.4\omega_f$	$-0.45\omega_f$
9	0	$-0.33\omega_f$	$-0.33\omega_f$	$-0.44\omega_f$
5	0	$-0.4\omega_f + j0.2\omega_f$	$-0.4\omega_f - j0.2\omega_f$	$-0.4\omega_f$

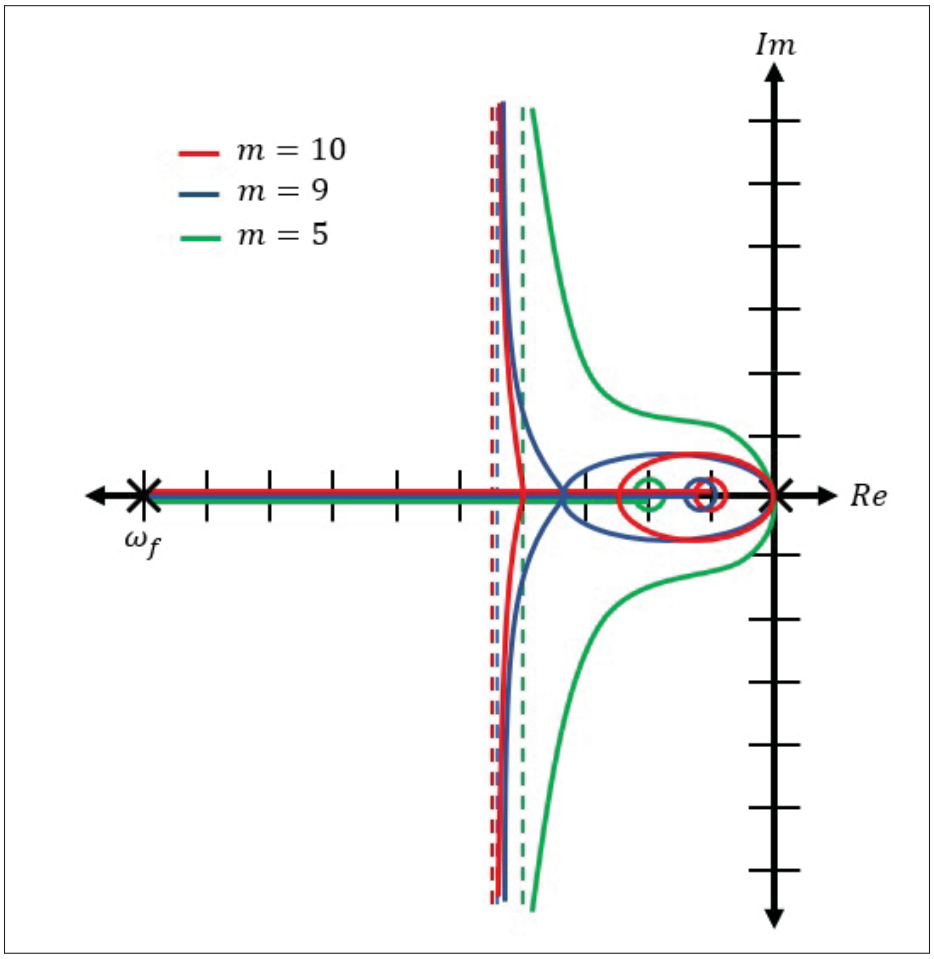

Figure 4.6 Root locus drawing as the controller's zero approaches the filter's pole

The design of the PLL could be based on either of the 3 root locus cases mentioned previously. Though having a filter closer to the controller's zero tends to lower the gain and phase margins.

4.2.2.3 Root-locus drawing of the qd0-PLL with second order low-pass filter

Since the desired PLL is expected be submitted to aggressive harmonics content due to the line voltage notch phenomenon, we may want the final design to contain a low-pass filter of second order in order to remove more harmful harmonic content.

The open-loop transfer function of the PLL with the second order filter is:

$$H(s) = \frac{k_p \omega_f^2 (s + k)}{s^2 (s^2 + 2\xi\omega_f s + \omega_f^2)} \tag{4.14}$$

Knowing that the system has 4 poles and 1 zero, we expect the root locus to have $N_a = n_p - n_z = 3$ asymptotic lines, at $\theta_a = \frac{\pi}{3}, \pi, \frac{5\pi}{3}$ radians (or 60, −60, 180 degrees). The centroid of the root locus is positioned at:

$$O_A = \frac{(-2\xi\omega_f) - (-k)}{3} = \frac{k - 2\xi\omega_f}{3}$$

Building the $P(s)$ function to find the roots where the root locus crosses the real axis yields:

$$P(s) = s^4 + \frac{4(\xi\omega_f + k)}{3} s^3 + \frac{\omega_f(\omega_f + 6k\xi)}{3} s^2 + \frac{2k\omega_f^2}{3} s = 0 \tag{4.15}$$

Which tells us that the root locus will always cross the origin. Since we already know that, we can remove from the equation the term that gives us this information. Simplifying equation (4.15) by reducing the order yields:

$$P(s) = s^3 + \frac{4(\xi\omega_f + k)}{3}s^2 + \frac{\omega_f(\omega_f + 6k\xi)}{3}s + \frac{2k\omega_f^2}{3} = 0$$

With 3 roots instead of 2, it would be much more difficult to analyze every possible case without fixing any parameters like it was done for the PLL with the first order filter. Instead, the frequency and the damping factor will be fixed at $\omega_f = 200$ rad/s and $\xi = 0.7$ respectively, and a numerical approach will be used to draw the root locus for different cases by varying the position of the controller's zero.

Since the closed loop transfer function for the root locus drawing is written:

$$G(s) = \frac{H(s)}{1 + KH(s)}$$

We know that the poles of the closed loop system are roots of the denominator of $G(s)$ expressed as $R(s)$:

$$\begin{aligned} R(s) &= 1 + KH(s) = D(s) + KN(s) \\ &= s^4 + 2\xi\omega_f s^3 + \omega_f^2 s^2 + K(\omega_f^2 s + k\omega_f^2) \\ &= s^4 + 2\xi\omega_f s^3 + \omega_f^2 s^2 + K\omega_f^2 s + kK\omega_f^2 \end{aligned}$$

The following algorithm will allow us to draw the root locus of the system, using $R(s)$ and varying the gain K from 0 towards infinity. The roots of $R(s)$ are the closed loop poles of the system for a given gain K. By superposing the curves obtained for different controller's zero locations, the evolution of the root locus can be exposed.

1. Set the initial gain K.
2. Calculate the characteristic polynomial $R(s)$.
3. Calculate $r = roots(R(s))$.
4. Draw roots (closed loop poles) r on a graph.
5. Increment the gain K and return to step 2.

Figure 4.7 shows the result of the process explained above and repeated for $m = 3, 4, 6$ where $\xi\omega_f = mk$.

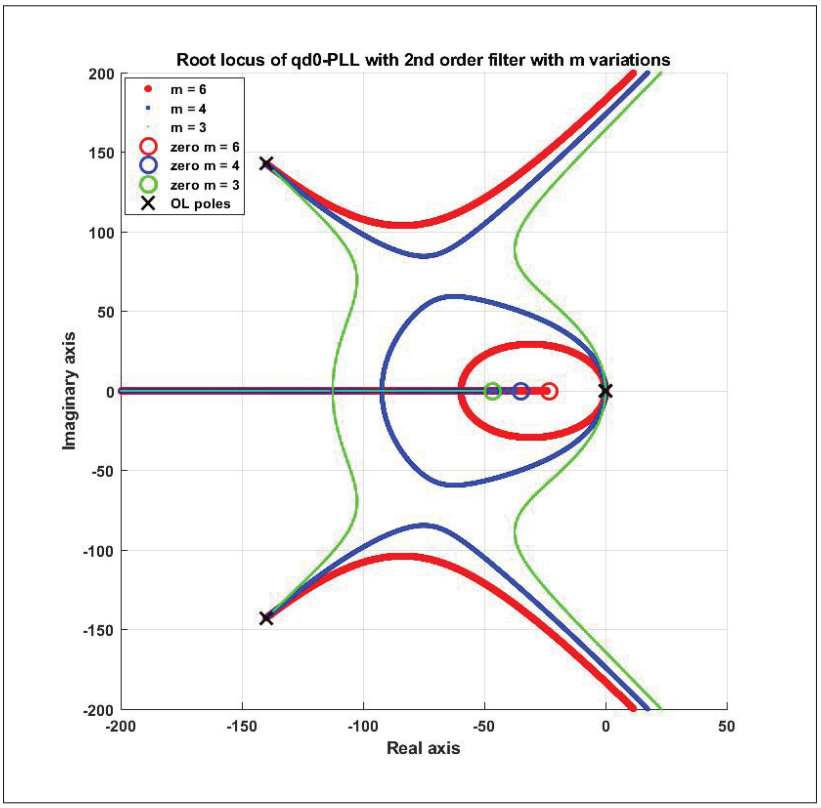

Figure 4.7 Root locus of qd0-PLL with 2nd order filter with m variations

Notice on figure 4.7 that as the controller's zero approaches the low-pass filter poles, the shape of the root locus approaches the imaginary axis. At some point between $m = 3$ and $m = 4$, the root locus curves merge, and the poles coming from the filter starts to follow a path leading to the controller's zero and infinity on the real axis instead of following the asymptotes at $\pm\pi/3$ rad. The desired design of the PLL should not reach this point. The red curve is the area where we want to design the controller of the PLL ($m \geq 4$). Note that the qd-PLL design can literally be scaled with the filter's cutoff frequency, if we consider ξ and m parameters to be fixed.

4.2.3 Qd0-PLL design

The goal of this section is to show the performance difference between the first and second order filters on the qd-frame PLL. The figure 4.8 shows the superposed root locus curves of the qd0 PLLs with order 1 and order 2 filters as well as the closed-loop poles positions chosen. The final gains for both PLLs are $k_p = 64$ and $k_i = 1664$, which places the controller's zero at -26 on the real axis.

The order 1 filter pole's location is $p_1 = -200$, and the order 2 filter's poles are at $p_2 = \xi\omega_f \pm j\omega_f\sqrt{1-\xi^2} = -140 \pm j143$.

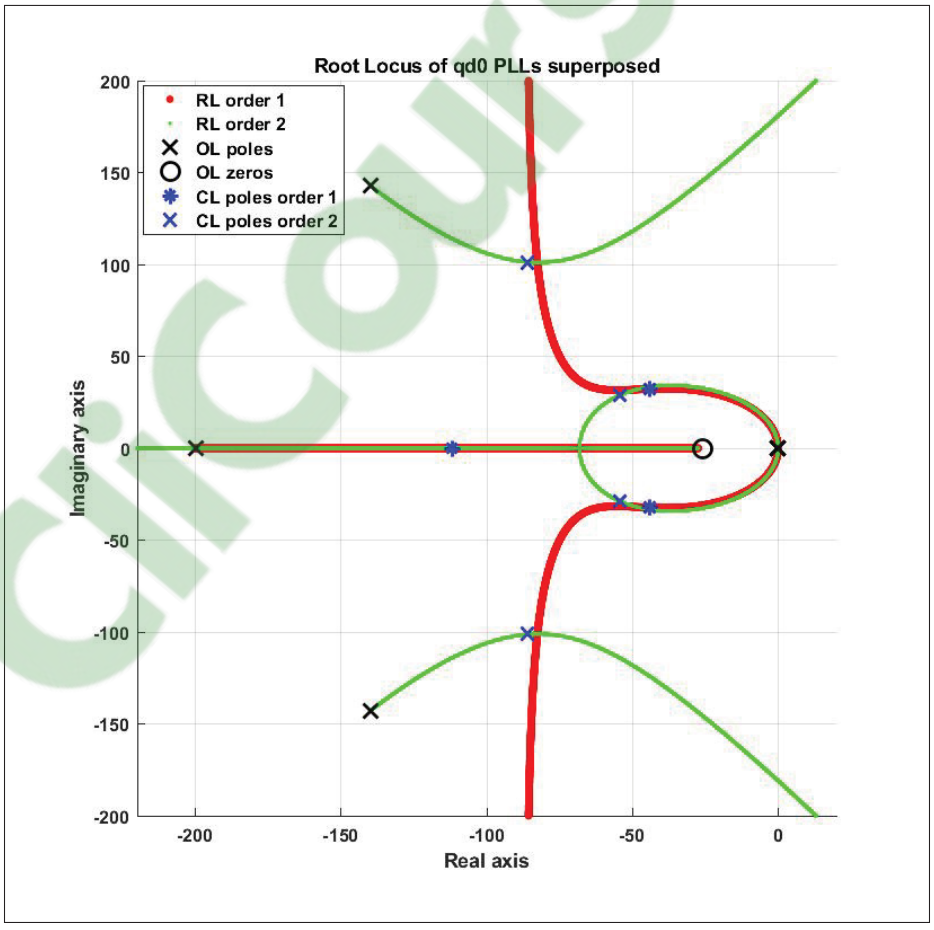

Figure 4.8 Root locus of qd0 PLLs superposed

Figure 4.9 shows the waveform of the voltage input of the PLL, which contains aggressive line voltage notches of a typical thyristor bridge.

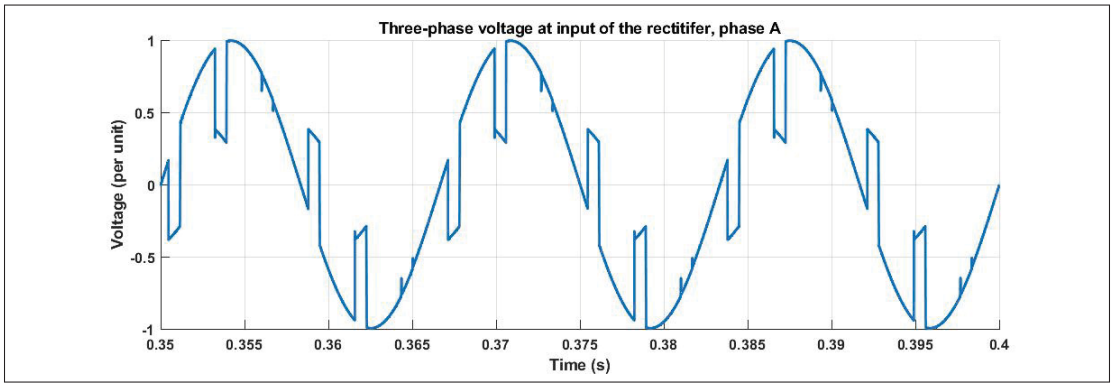

Figure 4.9 Voltage at input of rectifier, for a step of firing angle of 90 to 40 degrees (phase A)

Figures 4.10 and 4.11 show the amplitude and frequency response of the PLL to a firing angle input going from 90 to 40 degrees.

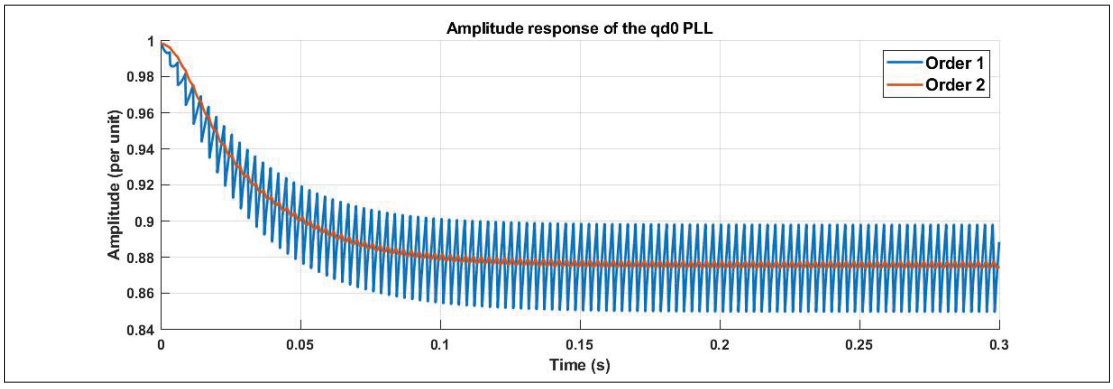

Figure 4.10 Amplitude estimation comparison of qd0 PLLs

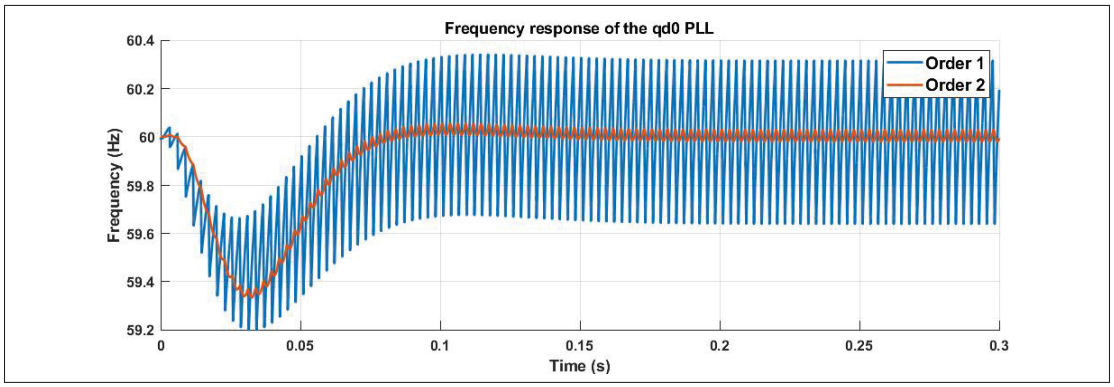

Figure 4.11 Frequency estimation comparison of qd0 PLLs

Notice on figure 4.11 that in order to achieve acceptable frequency ripples, the second order filter is almost mandatory. Consequently, the qd-frame PLL design that will be compared with the UTSP will be using the second order low-pass filter. Also, one must keep in mind that the frequency signal must be integrated to obtain the phase angle, which means that the obtained oscillations on the reference signal

4.3 UTSP model derivation and design

The UTSP proposed in Karimi H. (2019) is a robust algorithm that is able to almost completely decouple the positive sequence and negative sequence input. However, the structure of the UTSP is much more complicated than the qd0-PLL proposed in the last section, and may be more complicated to be physically implemented. A mathematical model of the UTSP is also given, making it possible to place the eigenvalues of the synchronization system at any desired region. It is assumed that the article Karimi H. (2019) and the thesis Karimi (2008) cover the UTSP subject enough, and does not need to be repeated here.

4.3.1 UTSP design

The goal of the UTSP design is to achieve similar or better harmonics filtering than the qd0-PLL, while placing the eigenvalues of the UTSP near the dominant poles of the qd0-PLL to achieve a

similar response time. That way, it will be possible to compare the filtering power of the two PLLs for similar response times.

Since the dominant poles of the qd0-PLL are placed at $s = -60 \pm j25$, we find the parameters $\mu_1 = \mu_2 = \mu$ by placing all the eigenvalues of the UTSP at the location of the dominant poles of the qd0-PLL. By using the UTSP eigenvalues location expression given in Karimi H. (2019):

$$s_{1,2} = s_{3,4} = -\mu \pm j\sqrt{\omega^2 - \mu^2} = -60 \pm j25$$

We then find the μ_i parameters of the UTSP:

$$\mu_1 = \mu = 60$$
$$\mu_2 = \mu = 60$$
$$\mu_3 = \omega^2 = 25^2 + 60^2 = 4225$$

Using those parameters yields the amplitude and frequency estimation results shown on figures 4.12 and 4.13 in response to a step of firing angle going from 90 to 40 degrees.

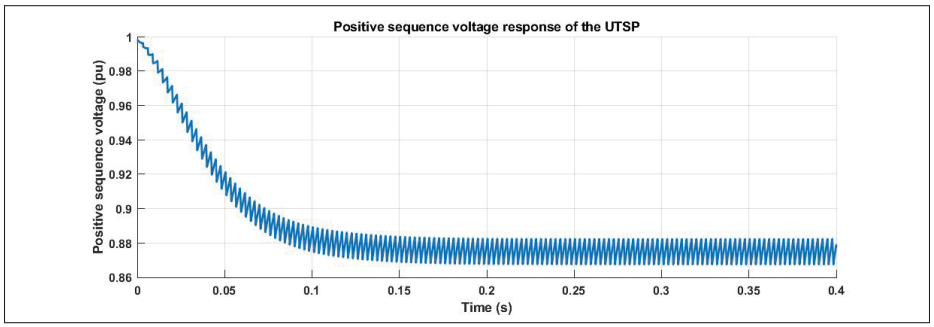

Figure 4.12 Voltage amplitude estimation response of the UTSP to a step of firing angle from 90 to 40 degrees

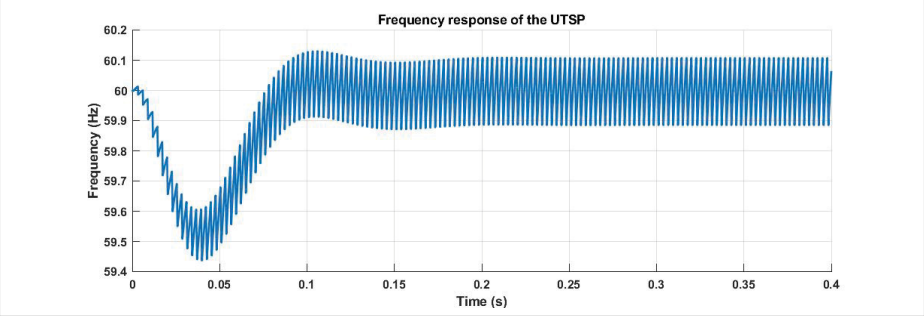

Figure 4.13 Frequency estimation response of the UTSP to a step of firing angle from 90 to 40 degrees

4.4 UTSP and qd0-PLL comparison

As explained in the previous section, the UTSP eigenvalues can be placed in any region of the complex plane. The gains will be chosen in a way that the eigenvalues of the UTSP matches the closed-loop poles of the qd-frame PLL using the second order low-pass filter. Looking at the amplitude and frequency estimated values is a good way to verify the performance of the synchronization system. However, our synchronization system needs to provide a phase angle to the gating circuits on which they will take their reference. If this reference swings too much, the real firing angle sent to the bridge will swing too, causing jittering on the waveforms. This is why we also provide a visual reference of how the phase angle swings by subtracting the source's firing angle to the estimated angle positioned at the input bridge voltage. Figure 4.14 below shows how the synchronization systems will be tested in a simulated environment.

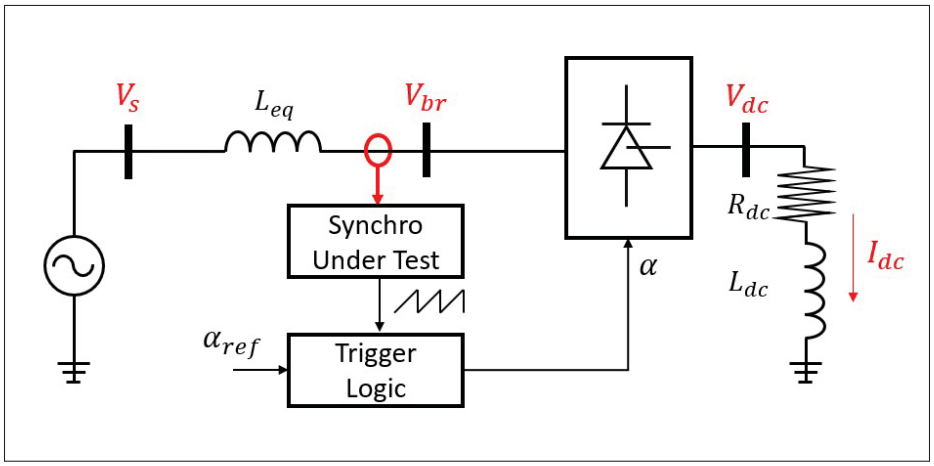

Figure 4.14 Electrical schematic of the simulated environment for synchronization systems testing

The final parameters of both studied PLL for the two proposed designs are compiled in table 4.2.

Table 4.2 Gains used for synchronization systems comparison

Designs	ω_f	k_p	k_i	μ_1	μ_2	μ_3
1	200	54	1080	40	40	2000
2	1000	270	27000	200	200	50000

For the first design with the low-pass filter positioned at $\omega_f = 200$, we get the closed-loop poles $s_{1,2} = -40 \pm j20$, and the following responses:

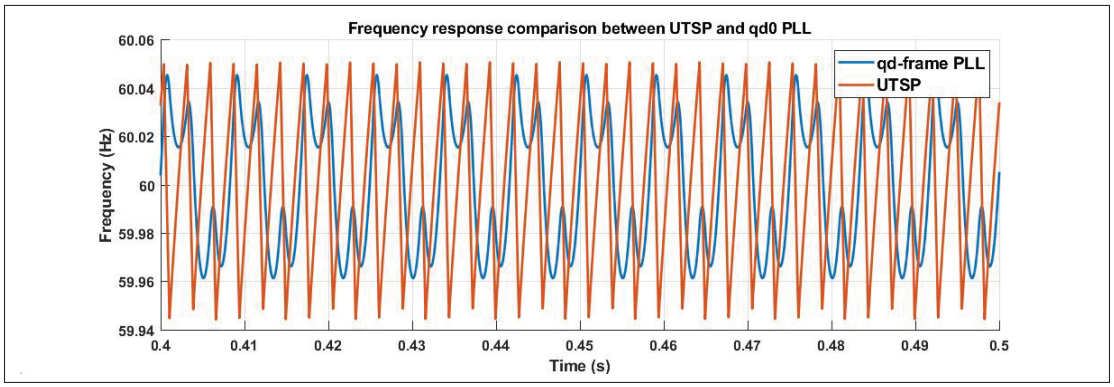

Figure 4.15 Estimated frequency comparison between UTSP and qd-frame PLL with low bandwidth

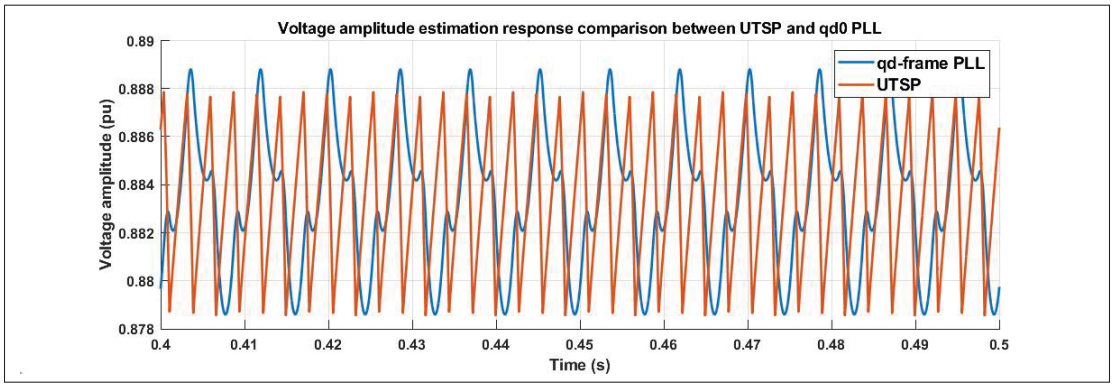

Figure 4.16 Estimated amplitude comparison between UTSP and qd-frame PLL with low bandwidth

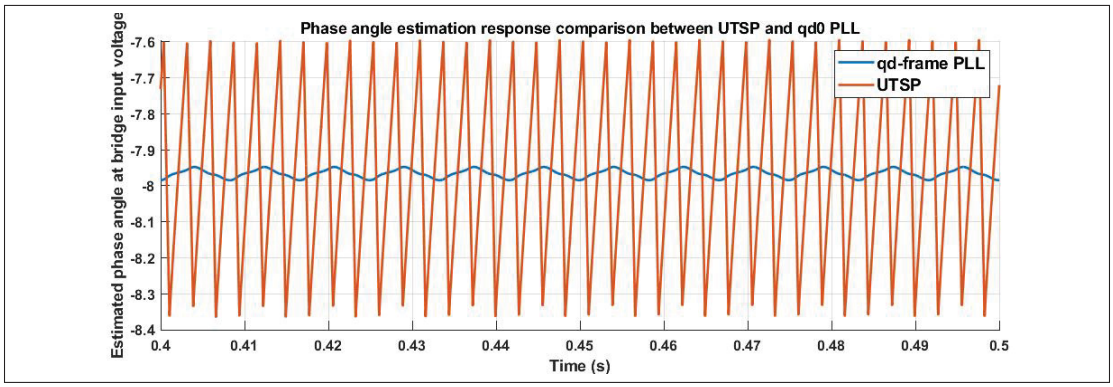

Figure 4.17 Estimated phase angle comparison between UTSP and qd-frame PLL with low bandwidth

With the design using a high cutoff frequency filter, we get the closed-loop poles $s_{1,2} = -200 \pm j100$ and the following responses:

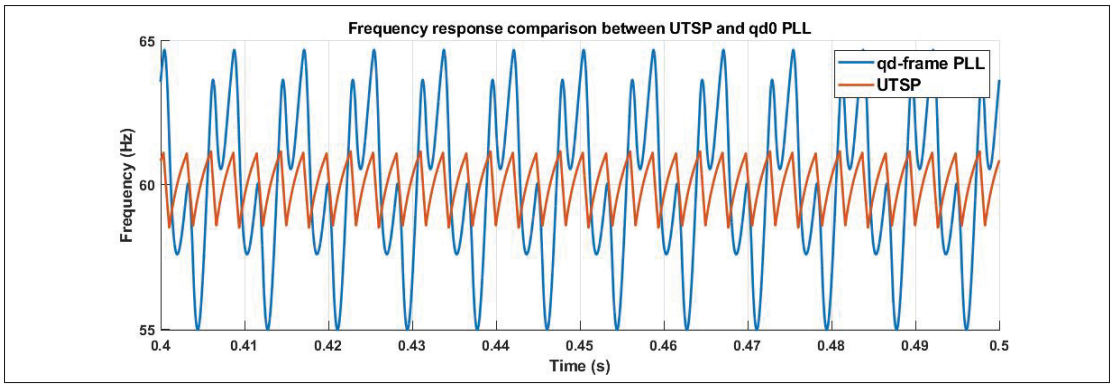

Figure 4.18 Estimated frequency comparison between UTSP and qd-frame PLL with high bandwidth

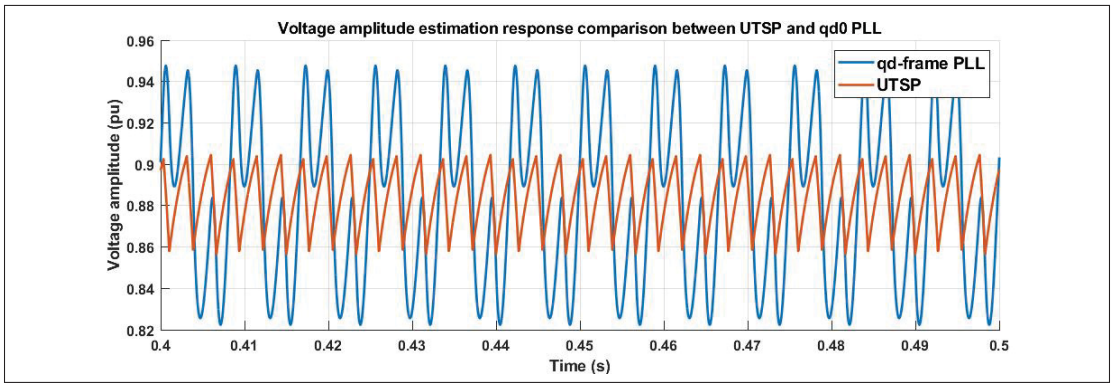

Figure 4.19 Estimated amplitude comparison between UTSP and qd-frame PLL with high bandwidth

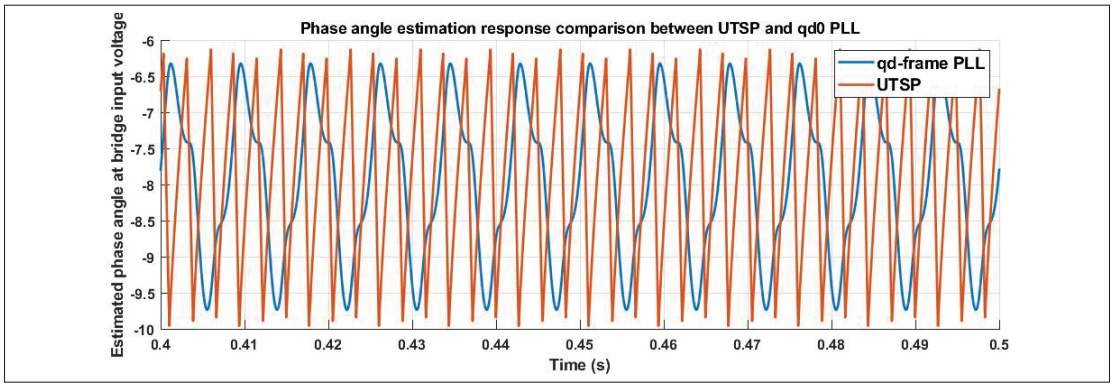

Figure 4.20 Estimated phase angle comparison between UTSP and qd-frame PLL with high bandwidth

4.5 Conclusions on proposed PLLs as synchronization devices for excitation systems

It is clear from the results of the synchronization systems comparisons that the bandwidth of the synchro has to be lowered in order to filter out the harmonic content created by the thyristor switching, giving up time response capacity in exchange. Also, the UTSP's filtering power seems kind of limited by looking at those results. This synchronization device was first created for negative sequence detection, and may not be perfectly suited for our application. There may

be a way to improve it by possibly adding a filter in its structure. However, it is out of the scope of this research. Detecting the negative sequence may be convenient, but does not seem to be necessary for now. It could be used for fault detection, but this subject will not be treated in this research. Remember that the voltage notch width was somewhat aggressive during the comparison. In practice, the notches could actually go that wide because of the large leakage inductance value of the excitation transformer and the high current drawn by the synchronous machine's rotor.

Having a phase angle swinging, and introducing a random error than can go up to more than one degree of firing angle may not be critical for an excitation system since it will be compensated by the regulation loops of the excitation system. However, it could create a serious error during the average model dynamic behavior validation. The topic will be discussed more deeply in Chapter 6.

Now that the synchronization system is designed, the switching model can be built, which will be the reference for the average model validation with simulation tools. Building the average model in state-space form is the subject of the next chapter.

CHAPTER 5

EXCITATION SYSTEM STATE-SPACE MODELING USING PARK'S TRANSFORM

The complete excitation system consists of the excitation transformer, the line voltage notch filter and the rectifier bridge. Figure 5.1 shows the excitation system's single line diagram.

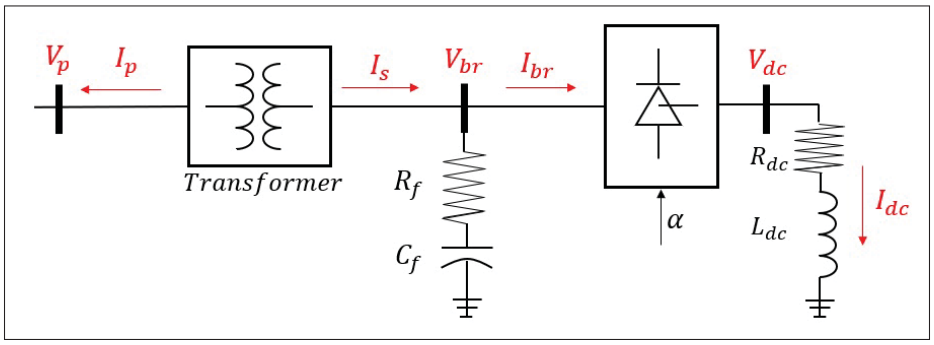

Figure 5.1 Single-line diagram of the excitation system

The technique that will be used for the excitation system modeling is circuit tearing introduced by Balabanian N. (1969), where the complete circuit can be cut into pieces to be modeled and validated separately. Then, the subsystems can be put back together for global validation and various applications. The technique is based on first writing the system's differential equations, then isolate its derivative terms. The variables having derivatives are state variables, the rest of the variables are the inputs of the model. Note that the models developed here are in per units.

5.1 Transformer state-space model expressed in per units

The method used in this chapter to create the state-space model of the transformer is based on the method used by Krause (2002) to build the mathematical model of the asynchronous machine in qd-frame as the asynchronous machine is often seen as a rotating transformer. The same approach is used but the rotor angle of the mutual inductance matrix is set to zero. In Krause (2002), the equations are first written in abc-frame. Then, they are transferred into qd-frame

and expressed into a primary-side equivalent with the transformer ratio. This allows to express all the mutual inductances of the system as a single one called L_m as well as expressing the model into per units. The equations developed in this section are using the same method, but the writing is shortened and adapted for state-space modeling.

The transformer model will be built in Simulink as an S-function with the S-function builder. We want to express the model into the following state-space form, with T subscript referring to transformer model.

$$\begin{aligned} \mathbf{x}_T &= \mathbf{A}_T\mathbf{x}_T + \mathbf{B}_T\mathbf{u}_T \\ \mathbf{y}_T &= \mathbf{C}_T\mathbf{x}_T + \mathbf{D}_T\mathbf{u}_T \end{aligned} \tag{5.1}$$

To write the equations into compressed matrix form, we consider the following new transformation matrices:

$$\mathbf{T}_s = \begin{bmatrix} \mathbf{K}_s & \mathbf{0} \\ \mathbf{0} & \mathbf{K}_s \end{bmatrix}, \ \mathbf{T}_s^{-1} = \begin{bmatrix} \mathbf{K}_s & \mathbf{0} \\ \mathbf{0} & \mathbf{K}_s \end{bmatrix}^{-1} \tag{5.2}$$

The input variables of the transformer state-space model are the voltages on primary and secondary sides, and the state variables are the primary and secondary currents. Consider the phase voltages, currents and flux linkages into compressed matrix form given by equation (5.3):

$$\mathbf{V}_{abc} = \begin{bmatrix} V_{a,p} \\ V_{b,p} \\ V_{c,p} \\ V_{a,s} \\ V_{b,s} \\ V_{c,s} \end{bmatrix}, \ \mathbf{i}_{abc} = \begin{bmatrix} i_{a,p} \\ i_{b,p} \\ i_{c,p} \\ i_{a,s} \\ i_{b,s} \\ i_{c,s} \end{bmatrix}, \boldsymbol{\lambda}_{abc} = \begin{bmatrix} \lambda_{a,p} \\ \lambda_{b,p} \\ \lambda_{c,p} \\ \lambda_{a,s} \\ \lambda_{b,s} \\ \lambda_{c,s} \end{bmatrix}, \tag{5.3}$$

With the flux linkage for a two-side transformer being:

$$\boldsymbol{\lambda}_{abc} = \begin{bmatrix} \mathbf{L}_{abc,p} & \mathbf{L}_{abc,ps} \\ \mathbf{L}_{abc,ps} & \mathbf{L}_{abc,s} \end{bmatrix} \mathbf{i}_{abc} = \mathbf{L}_{abc}\mathbf{i}_{abc} \tag{5.4}$$

The inductance matrix $\mathbf{L}_{abc,p}$ expresses the inductances tied to the flux linking the primary side phases of the transformer, with $L_{l,p}$ being the flux leakage inductances and $L_{m,p}$, the inductance linking the flux of the phases of the primary side.

$$\mathbf{L}_{abc,p} = \begin{bmatrix} L_{l,p} + L_{m,p} & -\frac{L_{m,p}}{2} & -\frac{L_{m,p}}{2} \\ -\frac{L_{m,p}}{2} & L_{l,p} + L_{m,p} & -\frac{L_{m,p}}{2} \\ -\frac{L_{m,p}}{2} & -\frac{L_{m,p}}{2} & L_{l,p} + L_{m,p} \end{bmatrix} \tag{5.5}$$

The inductance matrix $\mathbf{L}_{abc,s}$ expresses the inductances tied to the flux linking the secondary side phases of the transformer, with $L_{l,s}$ being the flux leakage inductances and $L_{m,s}$, the inductance linking the flux of the phases of the secondary side.

$$\mathbf{L}_{abc,s} = \begin{bmatrix} L_{l,s} + L_{m,s} & -\frac{L_{m,s}}{2} & -\frac{L_{m,s}}{2} \\ -\frac{L_{m,s}}{2} & L_{l,s} + L_{m,s} & -\frac{L_{m,s}}{2} \\ -\frac{L_{m,s}}{2} & -\frac{L_{m,s}}{2} & L_{l,s} + L_{m,s} \end{bmatrix} \tag{5.6}$$

The inductance matrix $\mathbf{L}_{abc,ps}$ expresses the inductances linking the flux of the primary to the secondary side phases, with $L_{m,ps}$ being the amplitude of the inductance varying over time as the asynchronous machine rotor rotates.

$$\mathbf{L}_{abc,ps} = L_{m,ps} \begin{bmatrix} \cos(\delta_r) & \cos(\delta_r + \frac{2\pi}{3}) & \cos(\delta_r - \frac{2\pi}{3}) \\ \cos(\delta_r - \frac{2\pi}{3}) & \cos(\delta_r) & \cos(\delta_r + \frac{2\pi}{3}) \\ \cos(\delta_r + \frac{2\pi}{3}) & \cos(\delta_r - \frac{2\pi}{3}) & \cos(\delta_r) \end{bmatrix} \tag{5.7}$$

But since our transformer is actually a stationary asynchronous machine, we set $\delta_r = 0$ (for a Y-Y transformer) and obtain the following matrix:

$$\mathbf{L}_{abc,ps} = \begin{bmatrix} L_{m,ps} & -\frac{L_{m,ps}}{2} & -\frac{L_{m,ps}}{2} \\ -\frac{L_{m,ps}}{2} & L_{m,ps} & -\frac{L_{m,ps}}{2} \\ -\frac{L_{m,ps}}{2} & -\frac{L_{m,ps}}{2} & L_{m,ps} \end{bmatrix} \tag{5.8}$$

We express the voltage drop equation of the transformer with the current reference as going out of the device first. We also wish to transfer the equation into qd-frame and express the bases in per units. The derivation in per units needs to be factored by the base frequency denoted ω_b in order to have the time base expressed in seconds, and the frequency in radians per seconds. Otherwise, the time would be stretched out by a factor of the base frequency. Also, we replace the flux linkages by their definition from equation (5.4) yieldings.

$$\mathbf{V}_{abc} + \mathbf{R}_T \mathbf{i}_{abc} + \frac{d}{dt}\left(\mathbf{L}_{abc}\mathbf{i}_{abc}\right) = 0 \tag{5.9a}$$

$$= \mathbf{T}_s^{-1}\mathbf{V}_{qd0} + \mathbf{R}_T\mathbf{T}_s^{-1}\mathbf{i}_{qd0} + \left(\frac{1}{\omega_b}\right)\frac{d}{dt}\left(\mathbf{L}_{abc}\mathbf{T}_s^{-1}\mathbf{i}_{qd0}\right) \tag{5.9b}$$

$$= \mathbf{T}_s\mathbf{T}_s^{-1}\mathbf{V}_{qd0} + \mathbf{T}_s\mathbf{R}_T\mathbf{T}_s^{-1}\mathbf{i}_{qd0} + \mathbf{T}_s\left(\frac{1}{\omega_b}\right)\frac{d}{dt}\left(\mathbf{L}_{abc}\mathbf{T}_s^{-1}\mathbf{i}_{qd0}\right) \tag{5.9c}$$

$$= \mathbf{V}_{qd0} + \mathbf{R}_T\mathbf{i}_{qd0} + \frac{\mathbf{T}_s\mathbf{L}_{abc}}{\omega_b}\frac{d}{dt}\left(\mathbf{T}_s^{-1}\right)\mathbf{i}_{qd0} + \frac{\mathbf{T}_s\mathbf{L}_{abc}\mathbf{T}_s^{-1}}{\omega_b}\frac{d}{dt}\left(\mathbf{i}_{qd0}\right) \tag{5.9d}$$

By using the substitutions:

$$\mathbf{G}_T = \mathbf{T}_s\frac{d}{dt}\left(\mathbf{T}_s^{-1}\right)$$

$$\mathbf{L}_T = \mathbf{T}_s\mathbf{L}_{abc}\mathbf{T}_s^{-1}$$

We get the following expression converted into qd-frame variables.

$$\mathbf{V}_{qd0} + \mathbf{R}_T \mathbf{i}_{qd0} + \frac{\mathbf{G}_T \mathbf{L}_T}{\omega_b} \mathbf{i}_{qd0} + \frac{\mathbf{L}_T}{\omega_b} \frac{d}{dt} \left(\mathbf{i}_{qd0} \right) = 0 \tag{5.10}$$

And by isolating the derivative term, we get:

$$\frac{d}{dt} \left(\mathbf{i}_{qd0} \right) = -\omega_b \mathbf{L}_\mathbf{T}^{-1} \mathbf{V}_{qd0} - \omega_b \mathbf{L}_T^{-1} \left(\mathbf{R}_T + \frac{\mathbf{G}_T \mathbf{L}_T}{\omega_b} \right) \mathbf{i}_{qd0}$$

Considering the qd-frame currents as state variables and qd-frame voltages as input variables, we can write the state equation as:

$$\dot{\mathbf{x}}_T = -\omega_b \mathbf{L}_T^{-1} \left(\mathbf{R}_T + \frac{\mathbf{G}_T \mathbf{L}_T}{\omega_b} \right) \mathbf{x}_T - \omega_b \mathbf{L}_T^{-1} \mathbf{u}_T \tag{5.11}$$

With the input and state variables defined by

$$\mathbf{u}_T = \begin{bmatrix} V_{q,p} \\ V_{d,p} \\ V_{0,p} \\ V_{q,s} \\ V_{d,s} \\ V_{0,s} \end{bmatrix}, \ \mathbf{x}_T = \begin{bmatrix} i_{q,p} \\ i_{d,p} \\ i_{0,p} \\ i_{q,s} \\ i_{d,s} \\ i_{0,s} \end{bmatrix} \tag{5.12}$$

We have the state matrices:

$$\mathbf{A}_T = -\omega_b \mathbf{L}_T^{-1} \left(\mathbf{R} + \frac{\mathbf{G}_T \mathbf{L}_T}{\omega_b} \right)$$

$$\mathbf{B}_T = -\omega_b \mathbf{L}_T^{-1}$$

With their exploded forms:

$$\mathbf{A}_T = \begin{bmatrix} \frac{R_p\omega_b L_s}{L_m^2 - L_p L_s} & -\omega & 0 & -\frac{R_s\omega_b L_m}{L_m^2 - L_p L_s} & 0 & 0 \\ \omega & \frac{R_p\omega_b L_s}{L_m^2 - L_p L_s} & 0 & 0 & -\frac{R_s\omega_b L_m}{L_m^2 - L_p L_s} & 0 \\ 0 & 0 & -\frac{R_p\omega_b}{L_{lp}} & 0 & 0 & 0 \\ -\frac{R_p\omega_b L_m}{L_m^2 - L_p L_s} & 0 & 0 & \frac{R_s\omega_b L_p}{L_m^2 - L_p L_s} & -\omega & 0 \\ 0 & -\frac{R_p\omega_b L_m}{L_m^2 - L_p L_s} & 0 & \omega & \frac{R_s\omega_b L_p}{L_m^2 - L_p L_s} & 0 \\ 0 & 0 & 0 & 0 & 0 & -\frac{R_s\omega_b}{L_{ls}} \end{bmatrix} \tag{5.13}$$

$$\mathbf{B}_T = \begin{bmatrix} \frac{\omega_b L_s}{L_m^2 - L_p L_s} & 0 & 0 & -\frac{\omega_b L_m}{L_m^2 - L_p L_s} & 0 & 0 \\ 0 & \frac{\omega_b L_s}{L_m^2 - L_p L_s} & 0 & 0 & -\frac{\omega_b L_m}{L_m^2 - L_p L_s} & 0 \\ 0 & 0 & \frac{\omega_b}{L_{lp}} & 0 & 0 & 0 \\ -\frac{\omega_b L_m}{L_m^2 - L_p L_s} & 0 & 0 & \frac{\omega_b L_p}{L_m^2 - L_p L_s} & 0 & 0 \\ 0 & -\frac{\omega_b L_m}{L_m^2 - L_p L_s} & 0 & 0 & \frac{\omega_b L_p}{L_m^2 - L_p L_s} & 0 \\ 0 & 0 & 0 & 0 & 0 & \frac{\omega_b}{L_{ls}} \end{bmatrix} \tag{5.14}$$

The desired output variables are the currents. But we also want to model the magnetizing branch resistance (iron losses) in the transformer. To do so, we add the R_m resistors at the primary and secondary voltage terminals. The output equation is then:

$$\mathbf{i}_{out} = \mathbf{i}_{qd0} - \frac{\mathbf{V}_{qd0}}{2R_m} \tag{5.15}$$

Expressed into the required matrix output equation form:

$$\mathbf{y}_T = \mathbf{I}_6\mathbf{x}_T - \frac{1}{2R_m}\mathbf{I}_6\mathbf{u}_T = \mathbf{C}_T\mathbf{x}_T + \mathbf{D}_T\mathbf{u}_T \tag{5.16}$$

The inductance value L_m is the mutual inductance expressed in per units. Considering the transformer ratio to be $m = N_s/N_p$, this inductance actually refers to $L_{m,p}$, $L_{m,s}$ and $L_{m,ps}$ mutual inductances. Also note that the inductance values L_p and L_s are expressed $L_p = L_{l,p} + L_m$ and $L_s = L_{l,s} + L_m$. The per unit bases used are the following:

$$\begin{aligned} \omega_{base} &= 2\pi f_{base} \\ Z_{base} &= \frac{3V_{base}^2}{S_{base}} \\ I_{base} &= \frac{S_{base}}{3V_{base}} \\ L_{base} &= \frac{Z_{base}}{\omega_{base}} \\ \lambda_{base} &= L_{base} I_{base} \end{aligned} \tag{5.17}$$

5.2 Transformer state-space model validation with simulation tools

The transformer state-space model created in this section is validated with the Simulink transformer in the Sim Power Systems (SPS) library. Figure 5.2 shows the process used to validate the transformer model.

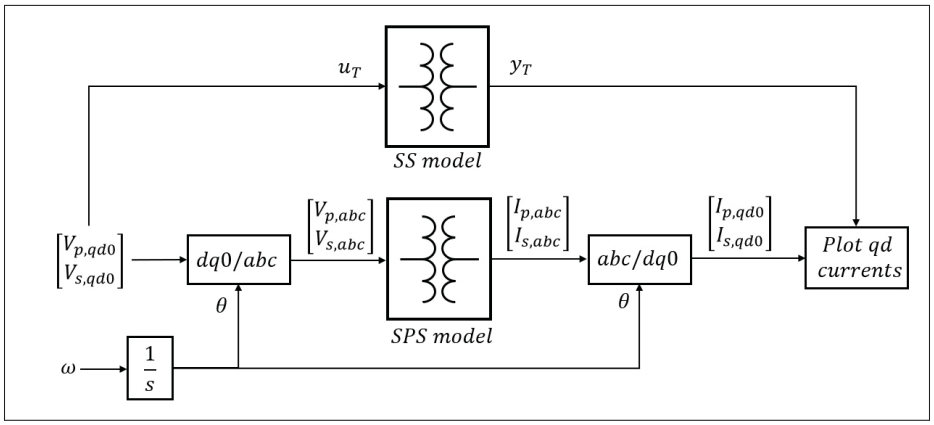

Figure 5.2 Comparison process between the state-space model and SPS model of the transformer

The validation is done through injecting qd-axis voltage steps to both transformers, and measuring their qd-axis output currents. Since the SPS model needs three-phase voltages, the inverse Park transform must be used on the qd-axis voltages step. Also, the computed three-phase currents must be transferred into qd-frame with the Park transform to compare with the state-space model. The angle used for the transforms is generated by integrating a signal coming from a frequency step. To make sure that there are no mathematical errors on the state-space model, arbitrary steps are applied in both q and d axis of both primary and secondary voltages. Tables 5.1, 5.2 and 5.3 give the bases parameters and the step inputs used in the validation simulation respectively.

Table 5.1 Transformer bases (rated values) used for validation by simulations (rms line-to-line values).

Prim. Voltage (V)	**Sec. Voltage (V)**	**Power (kW)**
600	31	25

Table 5.2 Transformer model parameters in per units.

$\mathbf{R_p}$ **(pu)**	$\mathbf{R_s}$ **(pu)**	$\mathbf{R_m}$ **(pu)**	$\mathbf{L_{l,p}}$ **(pu)**	$\mathbf{L_{l,s}}$ **(pu)**	$\mathbf{L_m}$ **(pu)**
0.05	0.05	20	0.1	0.1	20

Table 5.3 Step inputs applied to transformer models for validation by simulations.

	$\mathbf{V_{q,p}}$	$\mathbf{V_{d,p}}$	$\mathbf{V_{q,s}}$	$\mathbf{V_{d,s}}$	$\boldsymbol{\omega}$
Initial value (pu)	0.0	0.0	0.0	1.0	1.0
Final value (pu)	0.1	1.0	0.1	0.9	2.0
Step time (s)	0.1	0.0	0.3	0.2	0.4

Figures 5.4, 5.3, 5.6 and 5.5 compares the currents in qd-frame between the SPS and SS model, using the parameters of table 5.2 and step inputs of table 5.3.

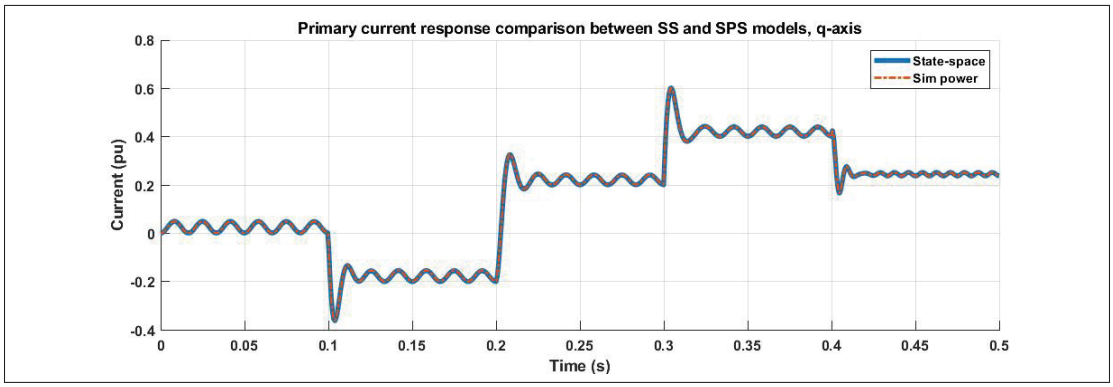

Figure 5.3 Primary currents in q-axis comparison between the models

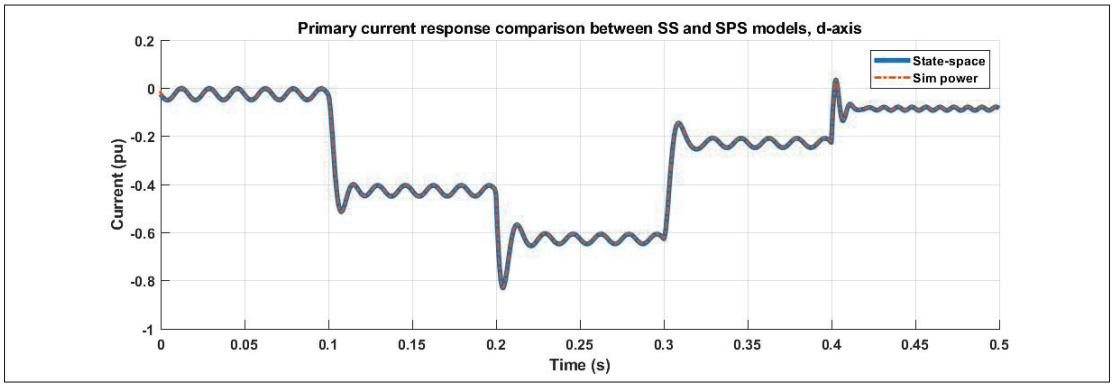

Figure 5.4 Primary currents in d-axis comparison between the models

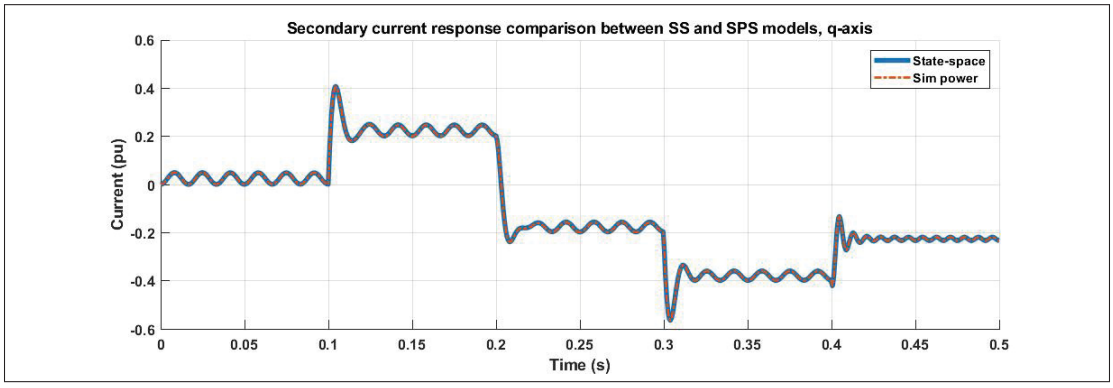

Figure 5.5 Secondary currents in q-axis comparison between the models

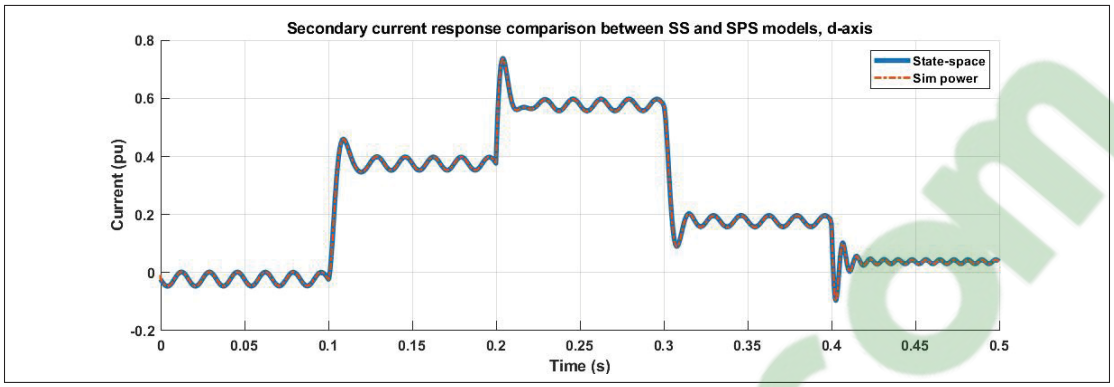

Figure 5.6 Secondary currents in d-axis comparison between the models

5.3 Line voltage notch filter state-space model

Figure 5.7 shows the single-line diagram of the RC filter used to filter line voltage notches.

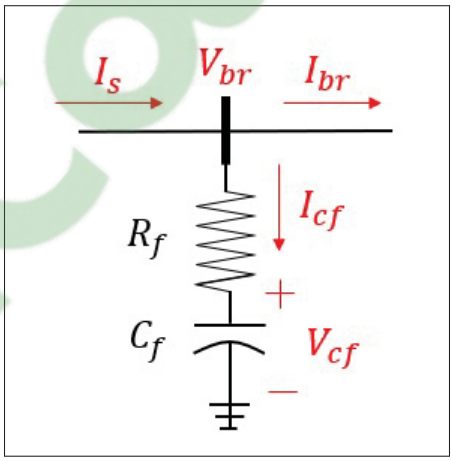

Figure 5.7 Line voltage notch filter single line diagram

Assuming that the filter parameters R_f and C_f are balanced between the phases, and that there are no coupling effects between the phases allows us to write the parameters as scalars in the

equations instead of having to use matrix forms, like it was the case for the transformer model. The state equation in abc-frame is written:

$$\mathbf{i}_{s,abc} - \mathbf{i}_{br,abc} - C_f \frac{d}{dt}\left(\mathbf{V}_{cf,abc}\right) = 0 \tag{5.18}$$

Transferring it into qd-frame gives:

$$\begin{aligned}
&\mathbf{K}_s^{-1}\mathbf{i}_{s,qd0} - \mathbf{K}_s^{-1}\mathbf{i}_{br,qd0} - \frac{C_f}{\omega_b}\frac{d}{dt}\left(\mathbf{K}_s^{-1}\mathbf{V}_{cf,qd0}\right) = 0 \\
&= \mathbf{K}_s\mathbf{K}_s^{-1}\mathbf{i}_{s,qd0} - \mathbf{K}_s\mathbf{K}_s^{-1}\mathbf{i}_{br,qd0} - \mathbf{K}_s\frac{C_f}{\omega_b}\frac{d}{dt}\left(\mathbf{K}_s^{-1}\mathbf{V}_{cf,qd0}\right) \\
&= \mathbf{i}_{s,qd0} - \mathbf{i}_{br,qd0} - \frac{C_f}{\omega_b}\mathbf{K}_s\frac{d}{dt}\left(\mathbf{K}_s^{-1}\mathbf{V}_{cf,qd0}\right) \\
&= \mathbf{i}_{s,qd0} - \mathbf{i}_{br,qd0} - \frac{C_f}{\omega_b}\mathbf{K}_s\frac{d}{dt}\left(\mathbf{K}_s^{-1}\right)\mathbf{V}_{cf,qd0} - \frac{C_f}{\omega_b}\mathbf{K}_s\mathbf{K}_s^{-1}\frac{d}{dt}\left(\mathbf{V}_{cf,qd0}\right) \\
&= \mathbf{i}_{s,qd0} - \mathbf{i}_{br,qd0} - \frac{C_f}{\omega_b}\mathbf{G}_f\mathbf{V}_{cf,qd0} - \frac{C_f}{\omega_b}\frac{d}{dt}\left(\mathbf{V}_{cf,qd0}\right)
\end{aligned}$$

Isolating the derivative term gives the final state equation:

$$\frac{d}{dt}\left(\mathbf{V}_{cf,qd0}\right) = \frac{\omega_b}{C_f}\left(\mathbf{i}_{s,qd0} - \mathbf{i}_{br,qd0}\right) - \mathbf{G}_f\mathbf{V}_{cf,qd0} \tag{5.19}$$

Where $\mathbf{G}_f$ is the coupling terms matrix:

$$\mathbf{G_f} = \mathbf{K}_s\frac{d}{dt}\left(\mathbf{K}_s^{-1}\right)$$

Since we want the output of the filter model to be the input bridge voltage $\mathbf{V}_{br,qd0}$, the output equation is:

$$\mathbf{V}_{br,qd0} = \mathbf{V}_{cf,qd0} + R_f\left(\mathbf{i}_{s,qd0} - \mathbf{i}_{br,qd0}\right) \tag{5.20}$$

By using equation sets (5.19) and (5.20), we write the equations into the state-space model form:

$$\dot{\mathbf{x}}_F = \mathbf{A}_F\mathbf{x}_F + \mathbf{B}_F\mathbf{u}_F$$
$$\mathbf{y}_F = \mathbf{C}_F\mathbf{x}_F + \mathbf{D}_F\mathbf{u}_F$$

Where:

$$\mathbf{x}_F = \begin{bmatrix} V_{cf,q} \\ V_{cf,d} \\ V_{cf,0} \end{bmatrix},\ \mathbf{u}_F = \begin{bmatrix} I_{s,q} \\ I_{s,d} \\ I_{s,0} \\ I_{br,q} \\ I_{br,d} \\ I_{br,0} \end{bmatrix},\ \mathbf{y}_F = \begin{bmatrix} V_{br,q} \\ V_{br,d} \\ V_{br,0} \end{bmatrix}$$

$$\mathbf{A}_F = \begin{bmatrix} 0 & -\omega & 0 \\ \omega & 0 & 0 \\ 0 & 0 & 0 \end{bmatrix},\ \mathbf{B}_f = \begin{bmatrix} \frac{\omega_b}{C_f} & 0 & 0 & -\frac{\omega_b}{C_f} & 0 & 0 \\ 0 & \frac{\omega_b}{C_f} & 0 & 0 & -\frac{\omega_b}{C_f} & 0 \\ 0 & 0 & \frac{\omega_b}{C_f} & 0 & 0 & -\frac{\omega_b}{C_f} \end{bmatrix}$$

$$\mathbf{C}_F = \mathbf{I}_3,\ \mathbf{D}_F = \begin{bmatrix} R_f & 0 & 0 & -R_f & 0 & 0 \\ 0 & R_f & 0 & 0 & -R_f & 0 \\ 0 & 0 & R_f & 0 & 0 & -R_f \end{bmatrix}$$

The parameters in the filter model are also all in per units, except the frequency ω, which is in radians per seconds. The per unit bases used for the filter model are the same as for the transformer, but it is different for the capacity base. The capacity base used is:

$$C_{base} = \frac{1}{\omega_{base} Z_{base}}$$

Building the filter model as an S-function in Simulink instead of the usual Linear Time-Invariant (LTI) block gives the possibility to use the frequency ω as an input, giving the model a time-variant characteristic and allowing the model to be used with a speed-varying synchronous machine.

5.4 Line voltage notch filter state-space model validation with simulation tools

The filter model is validated by comparison with a three-phase circuit. Both of them receive current steps into qd-frame, and their response is compared. The circuits parameters used are $R_f = 3$ pu, $C_f = 1$ pu, with a frequency base of 60 Hz. The step values and step times used for the RC filter validation with simulation files are summarized in table 5.4.

Table 5.4 Step values used for the RC filter model validation with simulation tools.

Inputs	**Initial value (pu)**	**Final value (pu)**	**Step time (s)**
$I_{s,d}$	0.0	0.1	0.0
$I_{s,q}$	0.0	0.1	0.1
$I_{br,d}$	0.0	0.1	0.2
ω	1.0	2.0	0.3
$I_{br,q}$	0.0	0.1	0.4

The qd-axis voltage results to the step inputs described in table 5.4 are shown on figures 5.8 and 5.9.

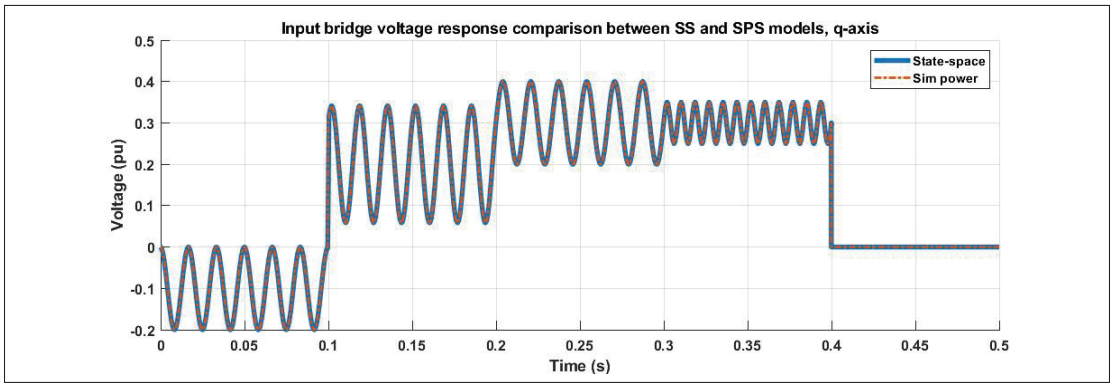

Figure 5.8 Voltage into q-axis response comparison between the models

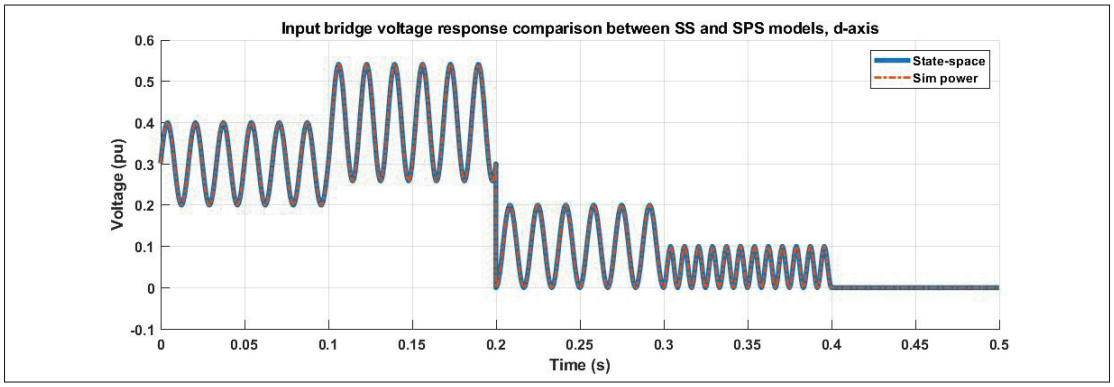

Figure 5.9 Voltage into d-axis response comparison between the models

5.5 Rectifier bridge state-space model

The rectifier bridge equations have to be expressed into qd-frame, then by applying the power balance, we link the three-phase (qd-frame) side with the DC side. The rectifier model does not have any differential terms, but its output equations can still be written and incorporated into the whole state-space model of the excitation system. The model built in this section is an equivalent transformer, based on equations (2.8, 2.9, 2.21) transferred into qd-frame.

First, we wish to find the expression of the switching function expressed into Park's reference frame:

$$\mathbf{S}_{qd0}(t) = \mathbf{K}_s \mathbf{S}_{abc}(t) \tag{5.21}$$

Expanding the matrices gives:

$$\mathbf{S}_{qd0}(t) = \frac{2\sqrt{3}}{\pi} \begin{bmatrix} \sin(\omega t - \alpha + \phi) \\ \sin(\omega t - \alpha + \phi - 2\pi/3) \\ \sin(\omega t - \alpha + \phi + 2\pi/3) \end{bmatrix} \begin{bmatrix} \cos(\theta(t)) & \cos(\theta(t) - \frac{2\pi}{3}) & \cos(\theta(t) + \frac{2\pi}{3}) \\ \sin(\theta(t)) & \sin(\theta(t) - \frac{2\pi}{3}) & \sin(\theta(t) + \frac{2\pi}{3}) \\ 1/2 & 1/2 & 1/2 \end{bmatrix}$$

Since it has been decided that the electrical reference is at the source voltage, the Park transformation angle has to be set on the source voltage phase angle. Substituting $\theta(t) = \omega t + 0$, expanding the terms and simplifying with trigonometric identities gives 5.22. The initial phase angle for $\theta(t)$ substitution needs to be null, because the transform phase angle input is the phase angle of the primary side phase voltage of the transformer, which has been chosen as the system's reference phase angle.

$$\mathbf{S}_{qd0} = \begin{bmatrix} S_q \\ S_d \\ S_0 \end{bmatrix} = \frac{2\sqrt{3}}{\pi} \begin{bmatrix} -\sin(\alpha - \phi) \\ \cos(\alpha - \phi) \\ 0 \end{bmatrix} \tag{5.22}$$

Equation (5.22) implies that the angle of the bridge voltage must somehow be calculated before the switching function can be calculated. Since the voltage inputs of the model are $V_{br,q}$ and $V_{br,d}$, the phase angle of the bridge voltage can be calculated:

$$\phi = atan\left(\frac{V_{br,q}}{V_{br,d}}\right) \tag{5.23}$$

To avoid a division by zero when computing the model, equation (5.23) has to be modified to:

$$\phi = atan\left(\frac{V_{br,q}}{\epsilon + |V_{br,d}|}\right) \tag{5.24}$$

Where ϵ is a small real number. Matlab actually has an ϵ parameter built in with the eps command used directly as a parameter.

The DC voltage is also expressed into qd-frame:

$$E_{dc} = (\mathbf{K}_s^{-1}\mathbf{S}_{qd0})^T(\mathbf{K}_s^{-1}\mathbf{V}_{qd0})$$

Expanding the terms and simplifying with trigonometric identities yields:

$$E_{dc} = \frac{3}{2}\left(S_q V_{br,q} + S_d V_{br,d}\right) \tag{5.25}$$

Or in the matrix form:

$$E_{dc} = \frac{3}{2}\mathbf{S}_{qd0}^T\mathbf{V}_{br,qd0} \tag{5.26}$$

The qd-frame currents expressed with the switching function, using equation (2.8), is written:

$$\mathbf{K}_s^{-1}\mathbf{I}_{qd0} = \mathbf{K}_s^{-1}\mathbf{S}_{qd0}I_{dc}$$

Which simplifies to:

$$\mathbf{I}_{qd0} = \mathbf{S}_{qd0} I_{dc} \tag{5.27}$$

If the voltage drop due to the line voltage notch is to be included in the model, equation (5.25) can be modified to:

$$E_{dc} = \frac{3}{2}\left(S_q V_{br,q} + S_d V_{br,d}\right) - \frac{3\omega L_s I_{dc}}{\pi} \tag{5.28}$$

Where L_s is the total line inductance seen by the bridge.

Figure 5.10 shows the equivalent circuit using equations (5.22, 5.27, 5.28).

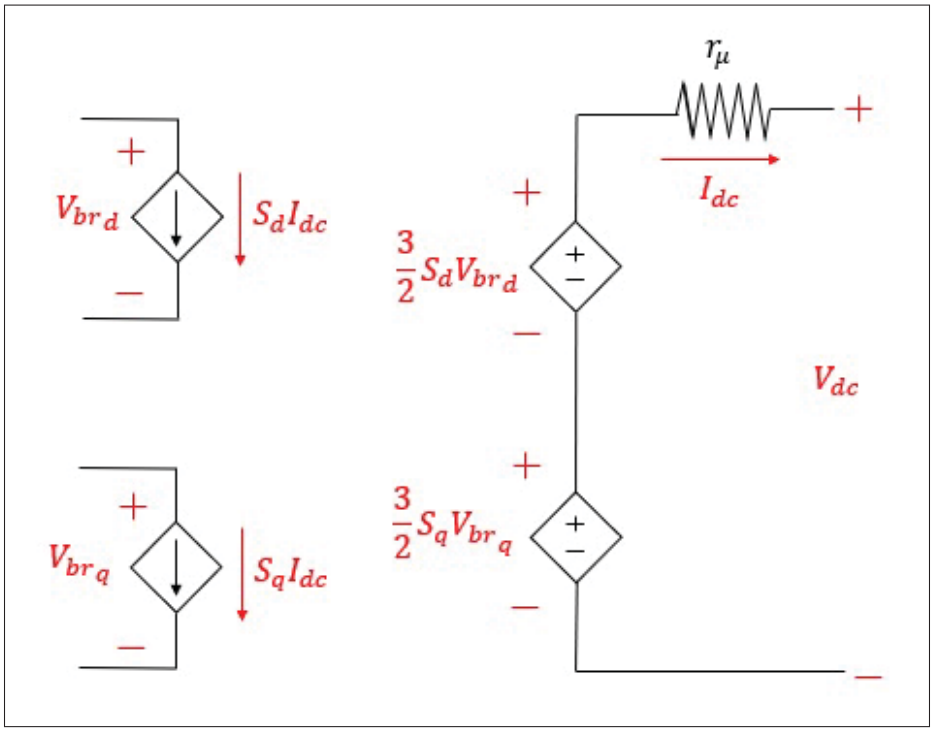

Figure 5.10 Averaged rectifier model equivalent circuit

To write the rectifier's equation into state-space form, we consider the inputs $\mathbf{u}_R$ and outputs $\mathbf{y}_R$:

$$\mathbf{u}_R = \begin{bmatrix} V_{br,q} \\ V_{br,d} \\ I_{dc} \end{bmatrix}, \mathbf{y}_R = \begin{bmatrix} E_{dc} \\ I_{br,q} \\ I_{br,d} \end{bmatrix}$$

The state-space model of the rectifier bridge is algebraic, which means that there are no state variables and no dynamic. The output equation written in the matrix form is:

$$\mathbf{y}_R = \mathbf{D}_R \mathbf{u}_R$$

Where:

$$\mathbf{D}_R = \begin{bmatrix} \frac{3S_q}{2} & \frac{3S_d}{2} & -r_\mu \\ 0 & 0 & S_q \\ 0 & 0 & S_d \end{bmatrix}$$

Note that both the frequency and the firing angle are not actual inputs of the state-space model equations, but those parameters are time-variant. The frequency is expected to vary as the controller of the offline synchronous machine must control it. Also, the firing angle will vary because this is the only command input of the Automatic Voltage Regulator (AVR). This means that the actual model built needs to use those parameters as signal inputs.

5.6 Rectifier bridge state-space model validation with simulation tools

For model validation purposes, the average model will be compared to a full switching model in Simulink. There will be no inductance on the lines for this test, as we only wish to validate the averaging of the model for now. Meaning we wish to validate the switching function principle as an equivalent transformer. The DC load for the test that will be used is a RL load, as it is the type of DC load that the rectifier is expected to be connected to with in the real application.

The voltage at the bridge input will have a phase angle, to make sure that the rectifier average model actually calculates the bridge angle correctly, and calculates the correct switching functions with it. This will insure that the rectifier average model acts as if the synchronization system is connected at the bridge input. This may seem trivial, but it is actually greatly important, as if this is not done, the output DC voltage would vary as the input bridge voltage angle shifts. Figures 5.11 and 5.12 show the voltage and current responses on the DC-side of the rectifier, while a firing angle step is applied.

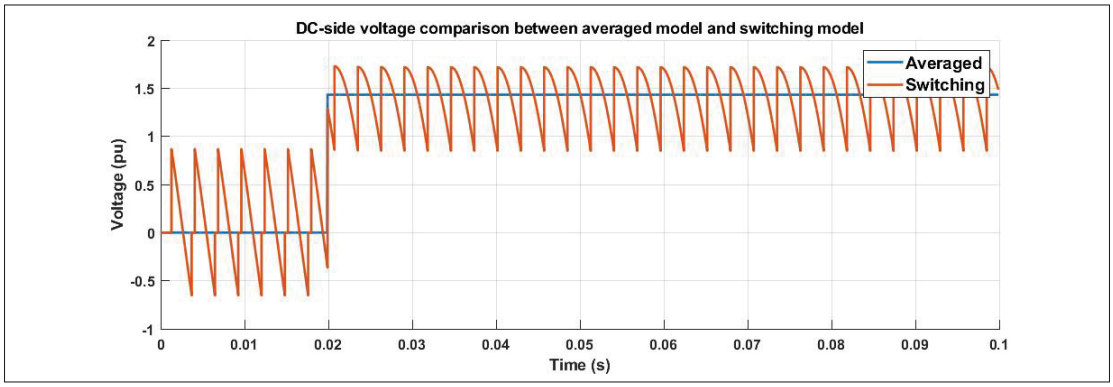

Figure 5.11 DC-side voltage comparison between the averaged model and the switching model for a step of firing angle from 90 to 30 degrees

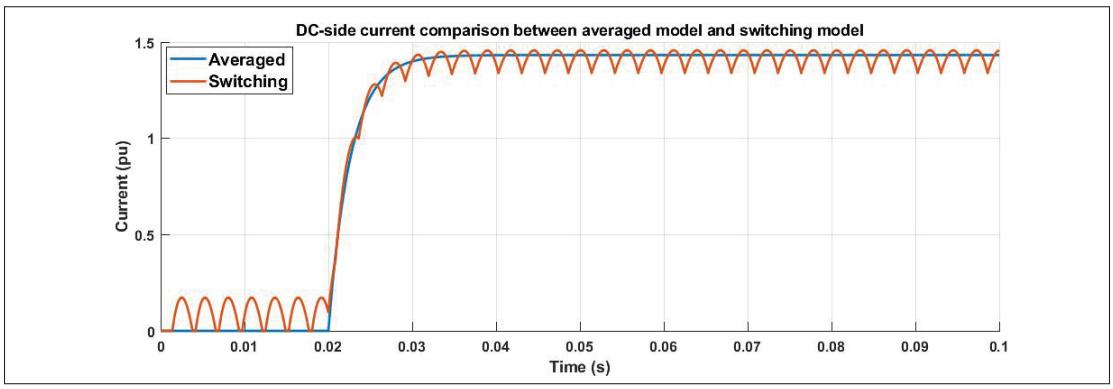

Figure 5.12 DC-side current comparison between the averaged model and the switching model for a step of firing angle from 90 to 30 degrees

Since the average model curve follows the average of the switching model curves, we know that the averaged model is able to simulate the synchronization system connected to the input bridge. Also, the switching functions are able to represent the DC values correctly. However, the line currents on the three-phase side still need to be validated. Figures 5.13 and 5.14 show the line currents response curves to the same experiment as figures 5.11 and 5.12.

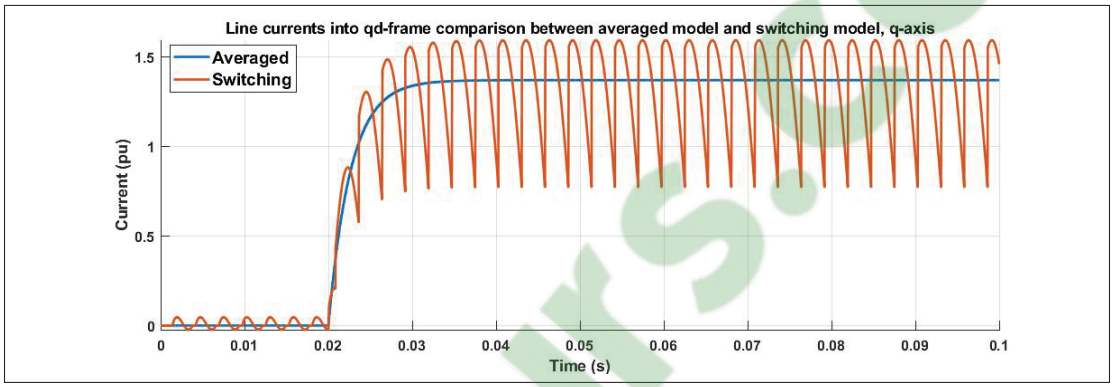

Figure 5.13 Line currents in q-axis comparison between the averaged model and the switching model for a step of firing angle from 90 to 30 degrees

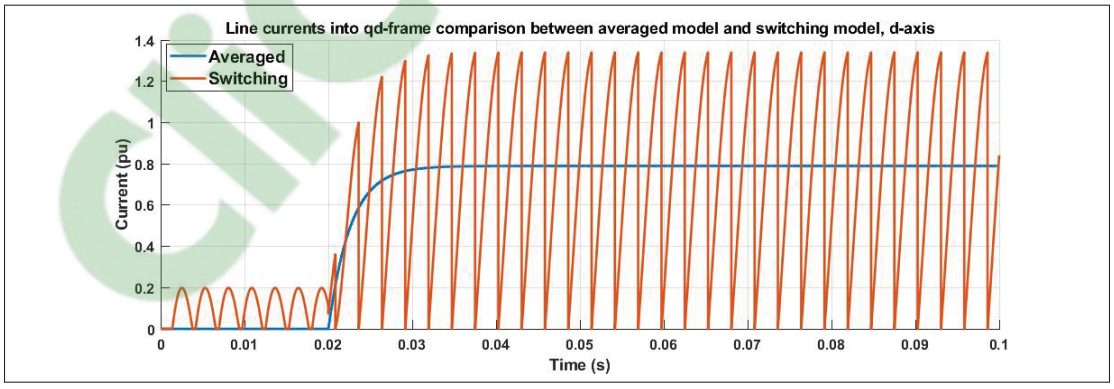

Figure 5.14 Line currents in d-axis comparison between the averaged model and the switching model for a step of firing angle from 90 to 30 degrees

5.7 Complete excitation system state-space model representation

The objective of this section is to combine subsystems state-space models to build the complete state-space model of the excitation system. **In this section, all the variables and parameters defining three-phase systems and subsystems are assumed to be into qd-frame**. The block diagram is shown in figure 5.15.

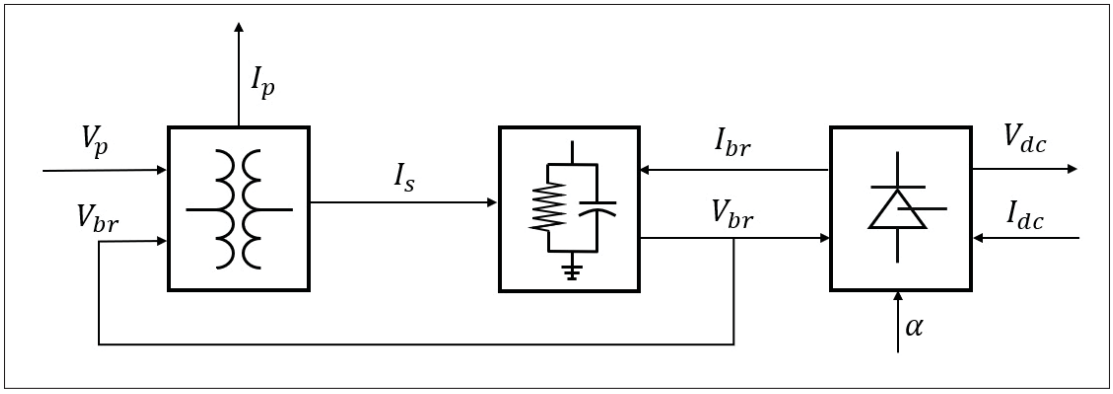

Figure 5.15 Excitation system state-space schematic

The subsystems state-space models are rewritten in simplified sub-matrices form, where the zero-sequence is neglected. For the transformer, the matrices are given by equation (5.29)

$$\begin{bmatrix} \dot{\mathbf{i}}_p \\ \dot{\mathbf{i}}_s \end{bmatrix} = \begin{bmatrix} \mathbf{A}_{T11} & \mathbf{A}_{T12} \\ \mathbf{A}_{T21} & \mathbf{A}_{T22} \end{bmatrix} \begin{bmatrix} \mathbf{i}_p \\ \mathbf{i}_s \end{bmatrix} + \begin{bmatrix} \mathbf{B}_{T11} & \mathbf{B}_{T12} \\ \mathbf{B}_{T21} & \mathbf{B}_{T22} \end{bmatrix} \begin{bmatrix} \mathbf{V}_p \\ \mathbf{V}_{br} \end{bmatrix}$$
$$\begin{bmatrix} \mathbf{i}_p \\ \mathbf{i}_s \end{bmatrix} = \begin{bmatrix} \mathbf{I} & 0 \\ 0 & \mathbf{I} \end{bmatrix} \begin{bmatrix} \mathbf{i}_p \\ \mathbf{i}_s \end{bmatrix} \tag{5.29}$$

For the RC filter:

$$\begin{aligned}\dot{\mathbf{V}}_{cf} &= \mathbf{A}_F\mathbf{V}_{cf} + \begin{bmatrix}\mathbf{B}_{F1} & \mathbf{B}_{F2}\end{bmatrix}\begin{bmatrix}\mathbf{i}_s \\ \mathbf{i}_{br}\end{bmatrix} \\ \mathbf{V}_{br} &= \mathbf{C}_F\mathbf{V}_{cf} + \begin{bmatrix}\mathbf{D}_{F1} & \mathbf{D}_{F2}\end{bmatrix}\begin{bmatrix}\mathbf{i}_s \\ \mathbf{i}_{br}\end{bmatrix}\end{aligned} \tag{5.30}$$

For the rectifier bridge:

$$\begin{bmatrix}E_{dc} \\ \mathbf{i}_{br}\end{bmatrix} = \begin{bmatrix}\frac{3}{2}\mathbf{S}^T & -r_\mu \\ 0 & \mathbf{S}\end{bmatrix}\begin{bmatrix}\mathbf{V}_{br} \\ I_{dc}\end{bmatrix} \tag{5.31}$$

We define input, state and output variables of the complete excitation system model as:

$$\mathbf{u}_e = \begin{bmatrix}\mathbf{V}_p \\ I_{dc}\end{bmatrix}, \mathbf{x}_e = \begin{bmatrix}\mathbf{i}_p \\ \mathbf{i}_s \\ \mathbf{V}_{cf}\end{bmatrix}, \mathbf{y}_e = \begin{bmatrix}\mathbf{i}_p \\ \mathbf{i}_s \\ \mathbf{V}_{br} \\ \mathbf{i}_{br} \\ E_{dc}\end{bmatrix} \tag{5.32}$$

To combine the state equations, for primary currents, we write:

$$\dot{\mathbf{i}}_p = \mathbf{A}_{T11}\mathbf{i}_p + \mathbf{A}_{T12}\mathbf{i}_s + \mathbf{B}_{T11}\mathbf{V}_p + \mathbf{B}_{T12}\mathbf{V}_{br} \tag{5.33}$$

Since the final goal is to write every state variables in terms of either state or input variables, $\mathbf{V}_{br}$ variables have to be replaced with the output equation of the filter. Doing so by replacing the output equation (5.30) into equation (5.33) yields:

$$\dot{\mathbf{i}}_p = \mathbf{A}_{T11}\mathbf{i}_p + \mathbf{A}_{T12}\mathbf{i}_s + \mathbf{B}_{T11}\mathbf{V}_p + \mathbf{B}_{T12}(\mathbf{C}_F\mathbf{V}_{cf} + \mathbf{D}_{F1}\mathbf{i}_s + \mathbf{D}_{F2}\mathbf{i}_{br}) \tag{5.34}$$

Also, bridge input currents $\mathbf{i}_{br}$ have to be replaced with the averaged rectifier equation $\mathbf{i}_{br} = \mathbf{S}I_{dc}$, equation (5.34) then becomes:

$$\dot{\mathbf{i}_p} = \mathbf{A}_{T11}\mathbf{i}_p + \mathbf{A}_{T12}\mathbf{i}_s + \mathbf{B}_{T11}\mathbf{V}_p + \mathbf{B}_{T12}(\mathbf{C}_F\mathbf{V}_{cf} + \mathbf{D}_{F1}\mathbf{i}_s + \mathbf{D}_{F2}(\mathbf{S}I_{dc})) \tag{5.35}$$

Which gives us the final result of the primary currents differential equations:

$$\dot{\mathbf{i}_p} = \mathbf{A}_{T11}\mathbf{i}_p + (\mathbf{A}_{T12} + \mathbf{B}_{T12}\mathbf{D}_{F1})\mathbf{i}_s + \mathbf{B}_{T12}\mathbf{C}_F\mathbf{V}_{cf} + \mathbf{B}_{T11}\mathbf{V}_p + \mathbf{B}_{T12}\mathbf{D}_{F2}\mathbf{S}I_{dc} \tag{5.36}$$

Using the same approach, we find the secondary currents and filter capacitor voltages differential equations to be:

$$\dot{\mathbf{i}_s} = \mathbf{A}_{T21}\mathbf{i}_p + (\mathbf{A}_{T22} + \mathbf{B}_{T22}\mathbf{D}_{F1})\mathbf{i}_s + \mathbf{B}_{T22}\mathbf{C}_F\mathbf{V}_{cf} + \mathbf{B}_{T21}\mathbf{V}_p + \mathbf{B}_{T22}\mathbf{D}_{F2}\mathbf{S}I_{dc}$$

$$\mathbf{V}_{cf} = \mathbf{B}_{F1}\mathbf{i}_s + \mathbf{A}_F\mathbf{V}_{cf} + \mathbf{B}_{F2}\mathbf{S}I_{dc}$$

Writing the above equations into augmented matrices form gives the final state equations:

$$\begin{bmatrix} \dot{\mathbf{i}_p} \\ \dot{\mathbf{i}_s} \\ \dot{\mathbf{V}_{cf}} \end{bmatrix} = \begin{bmatrix} \mathbf{A}_{T11} & \mathbf{A}_{T12} + \mathbf{B}_{T12}\mathbf{D}_{F1} & \mathbf{B}_{T12}\mathbf{C}_F \\ \mathbf{A}_{T21} & \mathbf{A}_{T22} + \mathbf{B}_{T22}\mathbf{D}_{F1} & \mathbf{B}_{T22}\mathbf{C}_F \\ \mathbf{0} & \mathbf{B}_{F1} & \mathbf{A}_F \end{bmatrix} \begin{bmatrix} \mathbf{i}_p \\ \mathbf{i}_s \\ \mathbf{V}_{cf} \end{bmatrix} + \begin{bmatrix} \mathbf{B}_{T11} & \mathbf{B}_{T12}\mathbf{D}_{F2}\mathbf{S} \\ \mathbf{B}_{T21} & \mathbf{B}_{T22}\mathbf{D}_{F2}\mathbf{S} \\ \mathbf{0} & \mathbf{B}_{F2}\mathbf{S} \end{bmatrix} \begin{bmatrix} \mathbf{V}_p \\ I_{dc} \end{bmatrix} \tag{5.37}$$

To build the output equations, the output variables need to be expressed in terms of state variables and input variables. The bridge voltage output equation given by the capacitor output equation is combined with the rectifier output equation to give:

$$\mathbf{V}_{br} = \mathbf{D}_{F1}\mathbf{i}_s + \mathbf{C}_F\mathbf{V}_{cf} + \mathbf{D}_{F2}\mathbf{S}I_{dc}$$

Replacing this equation into the DC voltage output equation of the rectifier yields:

$$E_{dc} = \frac{3}{2}\mathbf{S}^T(\mathbf{D}_{F1}\mathbf{i}_s + \mathbf{C}_F\mathbf{V}_{cf} + \mathbf{D}_{F2}\mathbf{S}I_{dc}) - r_\mu I_{dc}$$

The final output equation is then:

$$\begin{bmatrix} \mathbf{i}_p \\ \mathbf{i}_s \\ \mathbf{V}_{br} \\ \mathbf{i}_{br} \\ E_{dc} \end{bmatrix} = \begin{bmatrix} \mathbf{C}_{T11} & \mathbf{0} & \mathbf{0} \\ \mathbf{0} & \mathbf{C}_{T22} & \mathbf{0} \\ \mathbf{0} & \mathbf{D}_{F1} & \mathbf{C}_F \\ \mathbf{0} & \mathbf{0} & \mathbf{0} \\ \mathbf{0} & \frac{3}{2}\mathbf{S}^T\mathbf{D}_{F1} & \frac{3}{2}\mathbf{S}^T\mathbf{C}_F \end{bmatrix} \begin{bmatrix} \mathbf{i}_p \\ \mathbf{i}_s \\ \mathbf{V}_{cf} \end{bmatrix} + \begin{bmatrix} \mathbf{0} & \mathbf{0} \\ \mathbf{0} & \mathbf{0} \\ \mathbf{0} & \mathbf{D}_{F2}\mathbf{S} \\ \mathbf{0} & \mathbf{S} \\ \mathbf{0} & \frac{3}{2}(\mathbf{S}^T\mathbf{D}_{F2}\mathbf{S}) - r_\mu \end{bmatrix} \begin{bmatrix} \mathbf{V}_p \\ I_{dc} \end{bmatrix} \tag{5.38}$$

The state-space model given above does not consider the load of the system, which obviously impacts the dynamics of the system. Since we wish emulate the dynamic of an excitation system connected to a synchronous generator, we add a RL load to the DC-side, with an inductance big enough to damp the DC-current ripples. We choose such a value because synchronous generator rotor inductance usually have really large values.

Now, to model the whole system with an RL load connected to the DC-side, we first write the load differential equation in per unit:

$$\dot{I_{dc}} = \frac{\omega_b E_{dc}}{L_{dc}} - \frac{\omega_b R_{dc} I_{dc}}{L_{dc}} \tag{5.39}$$

By substituting E_{dc} to obtain an equation that is expressed as a function of the other state variables of the system, we obtain:

$$\dot{I_{dc}} = \frac{3\omega_b \mathbf{S}^T \mathbf{D}_{F1}}{2L_{dc}} \mathbf{i}_s + \frac{3\omega_b \mathbf{S}^T \mathbf{C}_F}{2L_{dc}} \mathbf{V}_{cf} + \omega_b \left(\frac{3\mathbf{S}^T \mathbf{C}_F}{2L_{dc}} - \frac{R_{dc} + r_\mu}{L_{dc}} \right) I_{dc} \tag{5.40}$$

Considering that the DC-side current is now a state variable instead of an input variable to the model, we may now re-write the state equation:

$$\begin{bmatrix} \dot{\mathbf{i}_p} \\ \dot{\mathbf{i}_s} \\ \dot{\mathbf{V}_{cf}} \\ \dot{I_{dc}} \end{bmatrix} = \begin{bmatrix} \mathbf{A}_{T11} & \mathbf{A}_{T12} + \mathbf{B}_{T12}\mathbf{D}_{F1} & \mathbf{B}_{T12}\mathbf{C}_F & \mathbf{B}_{T12}\mathbf{D}_{F2}\mathbf{S} \\ \mathbf{A}_{T21} & \mathbf{A}_{T22} + \mathbf{B}_{T22}\mathbf{D}_{F1} & \mathbf{B}_{T22}\mathbf{C}_F & \mathbf{B}_{T22}\mathbf{D}_{F2}\mathbf{S} \\ \mathbf{0} & \mathbf{B}_{F1} & \mathbf{A}_F & \mathbf{B}_{F2}\mathbf{S} \\ \mathbf{0} & \frac{3\omega_b \mathbf{S}^T \mathbf{D}_{F1}}{2L_{dc}} & \frac{3\omega_b \mathbf{S}^T \mathbf{C}_F}{2L_{dc}} & \omega_b \left(\frac{3\mathbf{S}^T \mathbf{C}_F}{2L_{dc}} - \frac{R_{dc}+r_\mu}{L_{dc}} \right) \end{bmatrix} \begin{bmatrix} \mathbf{i}_p \\ \mathbf{i}_s \\ \mathbf{V}_{cf} \\ I_{dc} \end{bmatrix} + \begin{bmatrix} \mathbf{B}_{T11} \\ \mathbf{B}_{T21} \\ \mathbf{0} \\ \mathbf{0} \end{bmatrix} \mathbf{V}_p \tag{5.41}$$

By also adding the DC current in the output variables, the output equation becomes:

$$\begin{bmatrix} \mathbf{i}_p \\ \mathbf{i}_s \\ \mathbf{V}_{br} \\ \mathbf{i}_{br} \\ E_{dc} \\ I_{dc} \end{bmatrix} = \begin{bmatrix} \mathbf{C}_{T11} & \mathbf{0} & \mathbf{0} & 0 \\ \mathbf{0} & \mathbf{C}_{T22} & \mathbf{0} & 0 \\ \mathbf{0} & \mathbf{D}_{F1} & \mathbf{C}_F & \mathbf{D}_{F2}\mathbf{S} \\ \mathbf{0} & \mathbf{0} & \mathbf{0} & \mathbf{S} \\ 0 & \frac{3}{2}\mathbf{S}^T\mathbf{D}_{F1} & \frac{3}{2}\mathbf{S}^T\mathbf{C}_F & \frac{3}{2}(\mathbf{S}^T\mathbf{D}_{F2}\mathbf{S}) - r_\mu \\ 0 & 0 & 0 & 1 \end{bmatrix} \begin{bmatrix} \mathbf{i}_p \\ \mathbf{i}_s \\ \mathbf{V}_{cf} \\ I_{dc} \end{bmatrix} + \begin{bmatrix} \mathbf{0} \\ \mathbf{0} \\ \mathbf{0} \\ \mathbf{0} \\ \mathbf{0} \\ 0 \end{bmatrix} \mathbf{V}_p \tag{5.42}$$

5.8 Conclusions on the state-space model of the excitation system

In this chapter, the state-space model of the excitation system as been built in qd-frame. Each subsystem has been validated with simulation experiments by comparing the model with Sim Power Systems simulation models. This at least guarantees that there are no major mathematical errors in the equations. However, the model needs to be validated by physical experiments to add real value to the research, which is the subject of the next chapter.

CHAPTER 6

VALIDATION OF THE COMPLETE EXCITATION SYSTEM STATE-SPACE MODEL

The goal of this chapter is to discover under which conditions the average model is actually able to reproduce experimental data. First, the validation method will be explained. There is a major complication regarding the perturbations sent to the firing angle command, and it will be explained thoroughly. Then, the experimental data recorded will be compared with the switching and average models and conclusions will be drawn on the validity of the average model.

6.1 Experimental state-space model validation method

The complete state-space model validation is done by injecting various angle set-points as well as perturbations at fixed frequencies, and comparing the output DC-side values of the switching model, averaged model and experimental rectifier. Temporal curves will be drawn and superposed for the reader to see directly if the curves are fitting or not, and give some analysis. Also, an FFT algorithm is used to isolate DC component as well as perturbation's frequency components on the DC-side values to calculate errors percentages between the experimental curves and the two simulation models results. That way, using many angle set-points, the limits of the model can be determined by experiments. The figure below shows a graphic representation of the model validation process experiments. The parameters denoted with the over-lined with a $tilde$ symbol are perturbation variables, while symbols without any over-line are the set-point (DC) values.

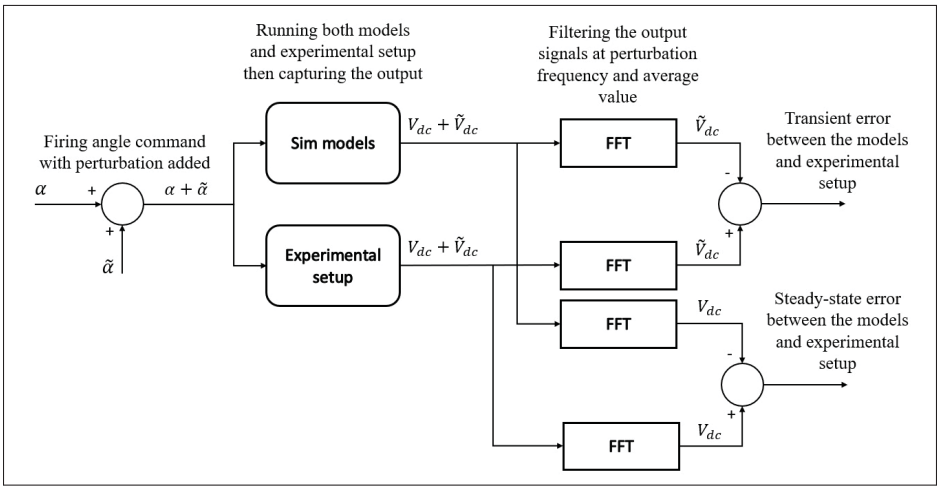

Figure 6.1 Graphical representation of error calculation of the validation process

On figure 6.1, notice that a sinusoidal perturbation has to be introduced on the firing angle command of the rectifier, which is not a problem in the simulation files. However, the simulation firing angle commands have to match with the ones sent to the experimental rectifier. This is where it gets a little more complicated. The firing pulse generation board (Oztek-2100) takes a 0-10V voltage signal as command input, and a signal generator device was used to give the firing angle commands. The problem is that during those experiments, the firing angle command sent to the rectifier bridge were not directly matching the displayed values on the signal generator. This means that the resulting firing angle commands sent by the bridge needed to be measured physically to be able to send the same firing angle set-point and perturbations on the simulation models. The firing angle experimental measurement was fairly difficult, especially for the perturbation amplitude values, which will be discussed in the next section.

A Matlab script was used to compile all the experimental data recorded, finding the real firing angle set-points and perturbation frequencies and amplitudes to send to the simulation models to be able to match the experimental and simulation curves. Figure 6.2 shows how the error data set is acquired from the simulation files and experimental data sets.

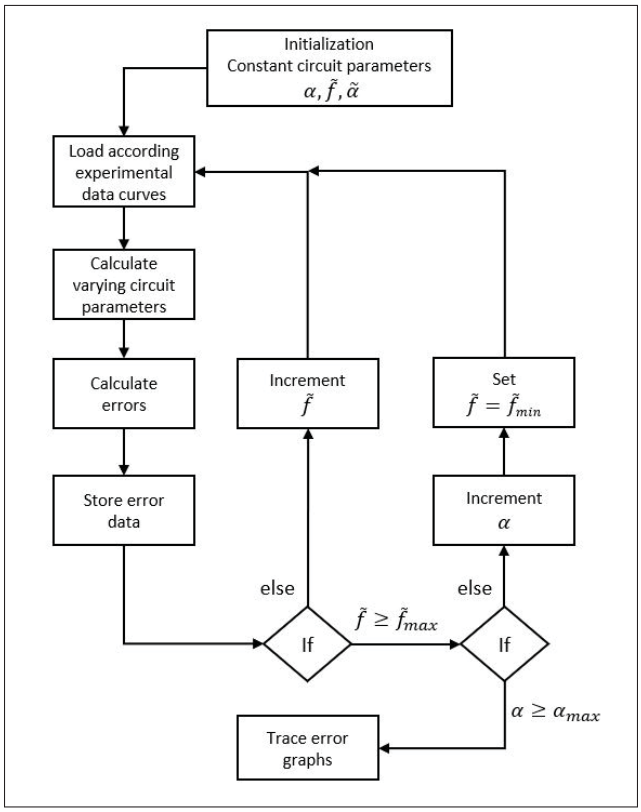

Figure 6.2 Pseudo-code of the process used to trace error data graphs

Note that $\tilde{f}$ is the frequency of the perturbation, $\tilde{\alpha}$ is the amplitude of the firing angle perturbation, and α is the firing angle set-point (constant value). Basically, the algorithm increments the perturbation frequency and firing angle set-points to match all the experimental curves recorded. The amplitude of the perturbation remains constant throughout the whole process. The varying circuit parameter calculated in this experiment is the DC-side physical resistance, which was varying greatly with temperature rise in the experimental setup. It was calculated by dividing the constant components of the voltage and current on the DC-side. Figures (6.3-6.7) are the pictures that were taken in the laboratory to show the equipment that was used.

Figure 6.3 Excitation transformer used during experiments

Figure 6.3 shows the transformer that was used, which is built as a $\Delta - Y$ configuration transformer, connected to an auto-transformer at the output.

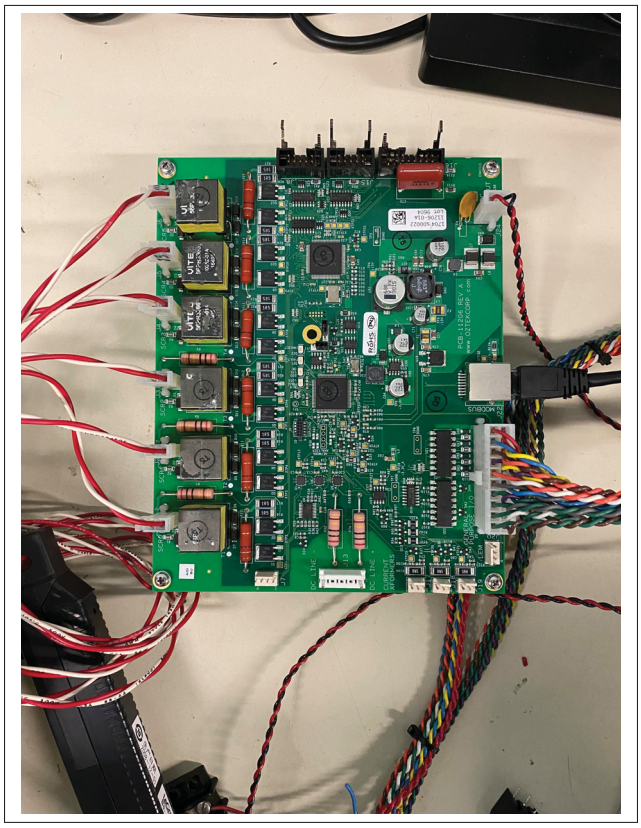

Figure 6.4 Firing board used during experiments

Figure 6.4 shows the firing board (Oztek-2100) that was used.

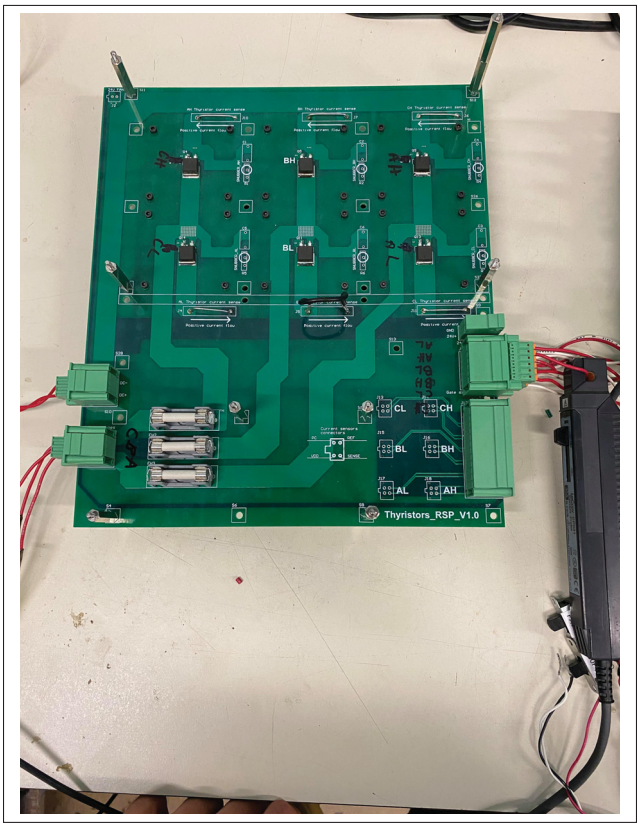

Figure 6.5 Thyristor board used during experiments

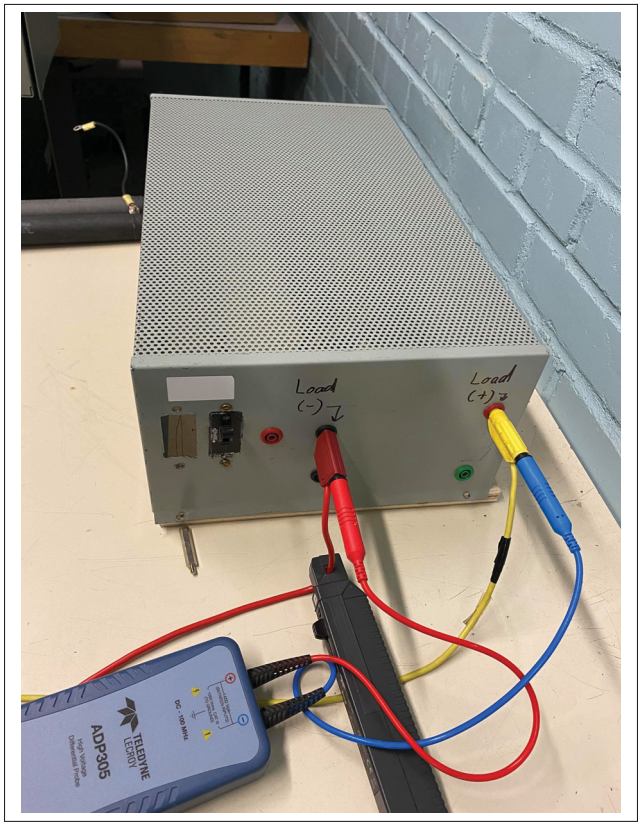

Figure 6.6 Load used during experiments (covered)

Figure 6.7 Load used during experiments (uncovered)

6.2 Firing angle set-point and perturbation measurement

The firing angle measurements are based on the delay measurement between the line voltage V_{ca} zero-crossing and the impulse sent to the thyristor connected between the phase A and the positive terminal of the DC voltage (thyristor A+). For the firing angle set-point, it is fairly simple since the delay can be measured directly. However, for the amplitude of the perturbation sent on the firing angle, persistence mode of the oscilloscope has to be used. This is because there is no other way to record the actual amplitude sent. Instead, we use persistence traces on the oscilloscope to recover the complete amplitude with time.

6.2.1 Firing angle set-point measurement method

As said before, the firing angle set-point is calculated by measuring a delay on the oscilloscope between the V_{ca} line voltage and the impulse sent to the thyristor connected to the phase A and the positive terminal of the DC-side. The figure below shows an example of the delay measurement with the oscilloscope. The persistence is shown on the oscilloscope only to include all the previous set-points on the image, showing the decreasing delay as the firing angle approaches zero. Note that on figure 6.8, the firing angle set-point corresponds to the distance between the cursors, but also needs a time to angle conversion.

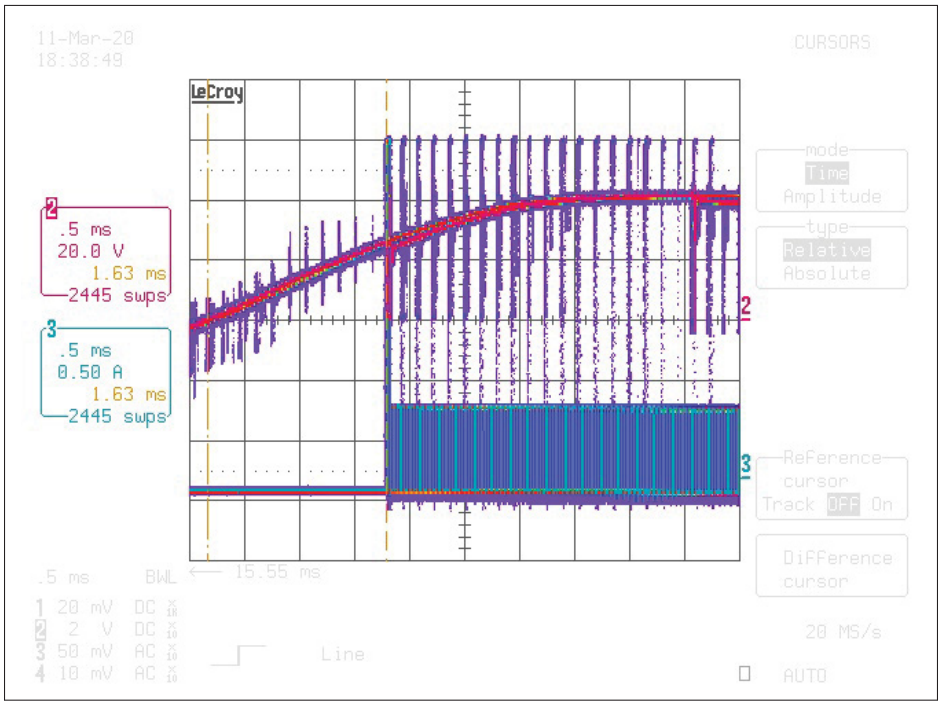

Figure 6.8 Oscilloscope screenshot used to show firing angle set-point measurement

As an example of firing angle measurement, the delay given by the oscilloscope cursors between the zero-crossing of V_{ca} bridge input line voltage and the firing pulse of thyristor A+ gives the following firing angle set-point:

$$\alpha = \frac{360^\circ}{T} t_\alpha = 60 \cdot 360^\circ \cdot 1.63 \cdot 10^{-3} = 35.21^\circ$$

The method has been used for firing angles going from about 100 to 30 degrees, and a graph has been drawn to show the similitude between the firing angle given by the Oztek firing angle board software and the measured firing angle with the presented method.

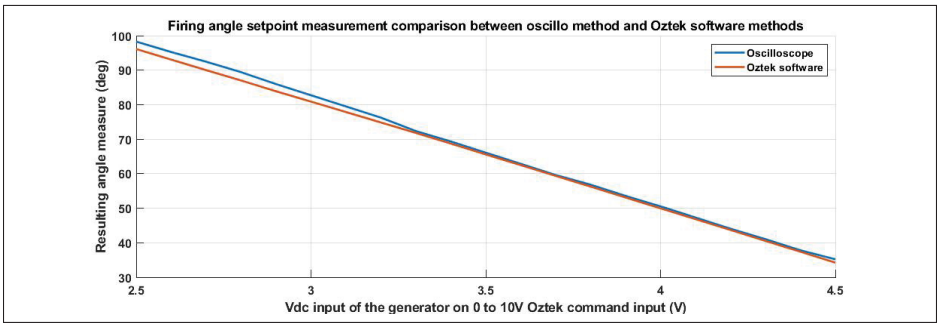

Figure 6.9 Comparison of the firing angle given by the Oztek software and the proposed measuring method

Notice that the curves do not perfectly fit. The figures below traces the errors between the curves, absolute and relative respectively. The error remains acceptable, but it also must be taken into account in the validation process as it increases the actual error between the experimental setup and the simulation models.

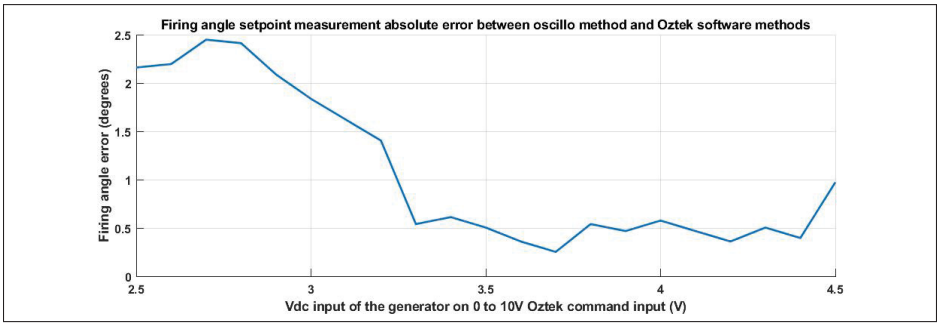

Figure 6.10 Firing angle set-point measurement absolute error between oscillo method and Oztek software

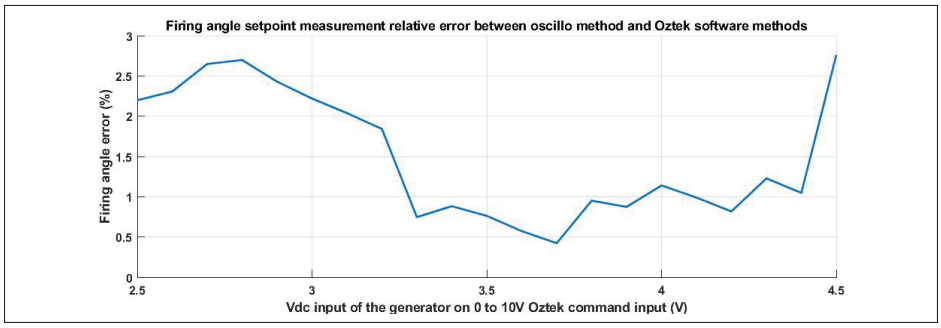

Figure 6.11 Firing angle set-point measurement relative error between oscillo method and Oztek software

The error for high firing angles (100 to 80) are pretty high. An error above 2 degrees would not be negligible. However, the model is not supposed to operate in this region. For most of the operating region, the error is under 1 degree, which is more acceptable. It is then confirmed that the delay measurement on the oscilloscope can at least give quite accurate value of the instantaneous firing angle sent to the rectifier bridge, and the concept could be used to measure the firing angle perturbation amplitude.

6.2.2 Firing angle perturbation amplitude measurement method

To measure the perturbation amplitude on the firing angle, we use persistence to be able to see the actual area where the firing angle sweeps. By taking half of the extremes (dividing peak value by 2), we get the amplitude. The figure below shows the oscilloscope screenshot used as an example to calculate the firing angle perturbation amplitude.

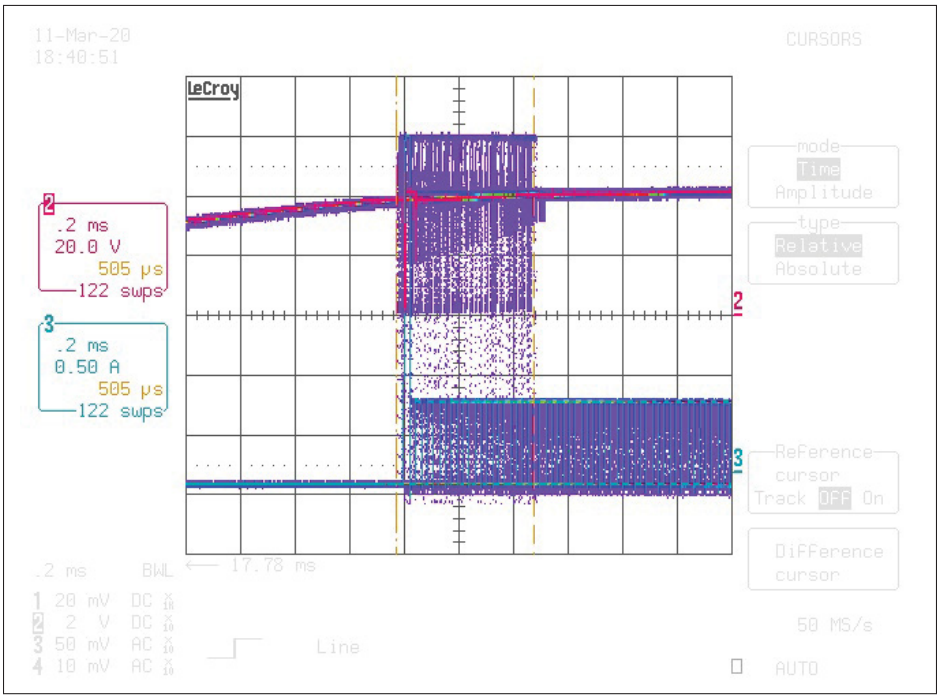

Figure 6.12 Oscilloscope screenshot used to show firing angle perturbation amplitude calculation

From figure 6.12, we get the following amplitude:

$$\tilde{\alpha} = \frac{360^\circ}{T}\widehat{t_\alpha} = 60 \cdot 360^\circ \cdot \frac{505 \cdot 10^{-6}}{2} = 5.45^\circ$$

An experiment has been conducted to evaluate if there is any kind of low-pass characteristic between the firing angle command input of the firing board, and the output firing angle sent to the physical semiconductors. To do so, amplitudes have been recorded with the discussed method for many frequencies and firing angle set-points. Figures 6.13 and 6.14 below show the data recorded during the experiment.

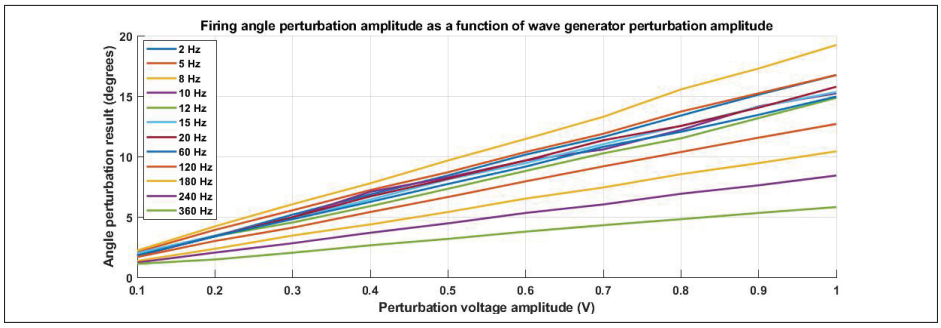

Figure 6.13 Firing angle perturbation amplitude as a function of wave generator perturbation voltage amplitude for different frequencies

Figure 6.13 tells us that for a fixed frequency, the output firing angle amplitude of a perturbation respects quasi linear relation with the wave generator perturbation voltage input on the firing board. It was expected that the experiment would show some kind of low-pass behavior, and this is clearly true for frequencies of 60 Hz and higher, but does not seems to be the case otherwise. To give another perspective, figure 6.14 instead traces the resulting perturbation amplitude on the firing angle as a function of frequency.

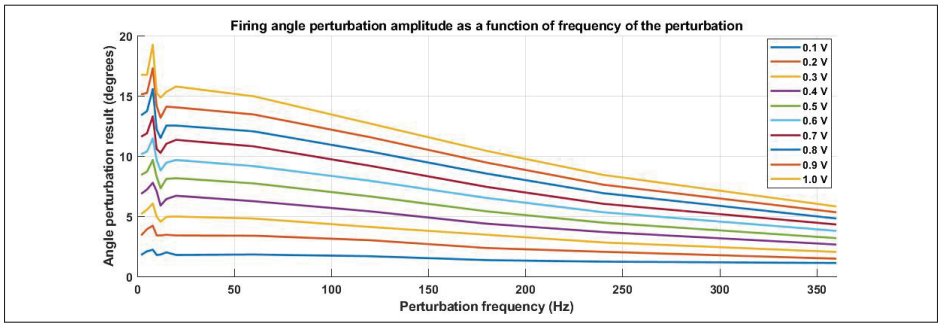

Figure 6.14 Firing angle perturbation amplitude as a function of perturbation frequencies for different wave generator perturbation voltages

The low-pass behavior of the firing board is clearly shown on figure 6.14. However, a ripple also happens at low frequencies, which is shown more clearly on figure 6.15, showing the same data as figure 6.14 but zoomed on lower frequencies.

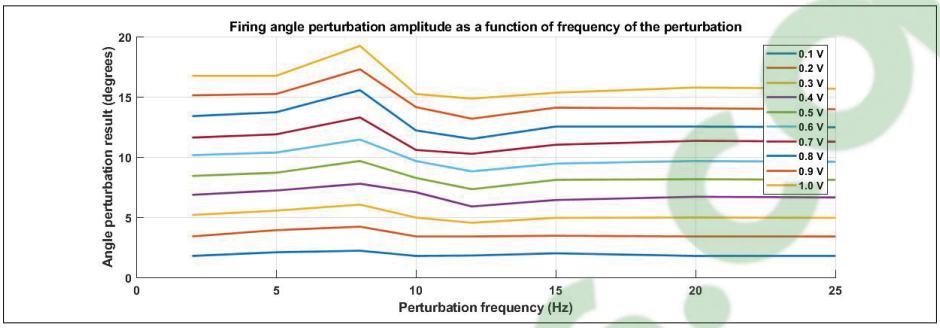

Figure 6.15 Firing angle perturbation amplitude as a function of perturbation frequencies for different wave generator perturbation voltages

Figure 6.15 clearly shows the spike and ripple around 8 Hz that caused the curves to seem to not fit for low frequencies on figure 6.13. The spike repeats for every curve of different voltage amplitude recorded, which rules out the fact that the unexpected behavior may have come from recording errors. Something really happens at low frequency on the firing board that causes an important ripple. Some hypothesis can be made on this phenomenon, but the real cause will not be identified in this research since the code on the board is propriety of Oztek. What is important to remember from this experiment is that the amplitude on the firing angle sent in the simulations will change for every experimental data sets. However, the recorded data in this section clearly shows that the firing board has a dynamic in itself, and seems to have a kind of filter centered at low frequencies, which is exactly in the synchronous machine's bandwidth. This means that there are no doubt that the firing board dynamics will affect the excitation system sold by Andritz-Hydro Canada (AHC), but it is unknown to what extent.

6.3 Experiments at low perturbation amplitude

We have seen in the previous section that the ripple around 8 Hz on figure 6.14 worsens as the perturbation voltage amplitude input of the function generator increases. We then wish to see if the experimental data will fit if we use a low perturbation amplitude. This experiment should isolate out (or most of it) the low-pass characteristic of the firing board. If this is true, the averaged model should have a lower error for low perturbation amplitude than for higher amplitude.

The experimental data has been recorded for many DC component of the wave generator voltage, as well as many frequencies of the AC component, but for a fixed perturbation voltage of $0.2V$. Tables 6.1 and 6.2 compile the input command sent to the firing board. By using figures 6.9 and 6.14, the angle values are also given.

Table 6.1 Firing angle set-points used during the validation process for low perturbation amplitudes

$\mathbf{V_{gen,dc}}$ **(V)**	**3**	**3.5**	**4**	**4.5**
α (deg)	81	65	50	35

By using the 0.2V perturbation curve on the graph of figure 6.14, we create the table 6.2, which will be used to send the correct perturbations on the firing angle to better fit the experimental data.

Table 6.2 Firing angle perturbations used during the validation process for low perturbation amplitudes

$\tilde{\mathbf{f}}$ **(Hz)**	2	5	8	10	12	15	20	60	120	180	240	360
$\tilde{\alpha}$ **deg**	3.40	3.92	4.21	3.4	3.4	3.46	3.4	3.38	3	2.35	2.04	1.47

Figures (6.16-6.23) give the error percentages for every physically recorded data sets between the simulation models and the experimental data.

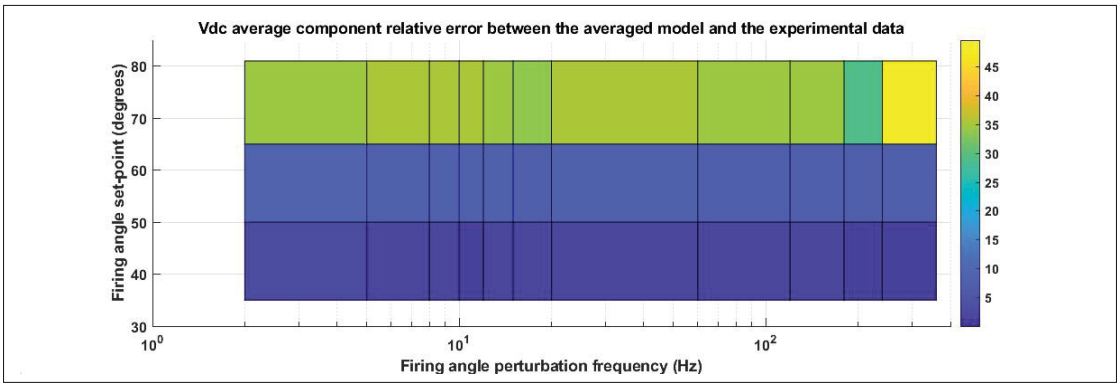

Figure 6.16 Relative error on DC-side voltage DC component between average model and experimental data for low amplitude perturbations

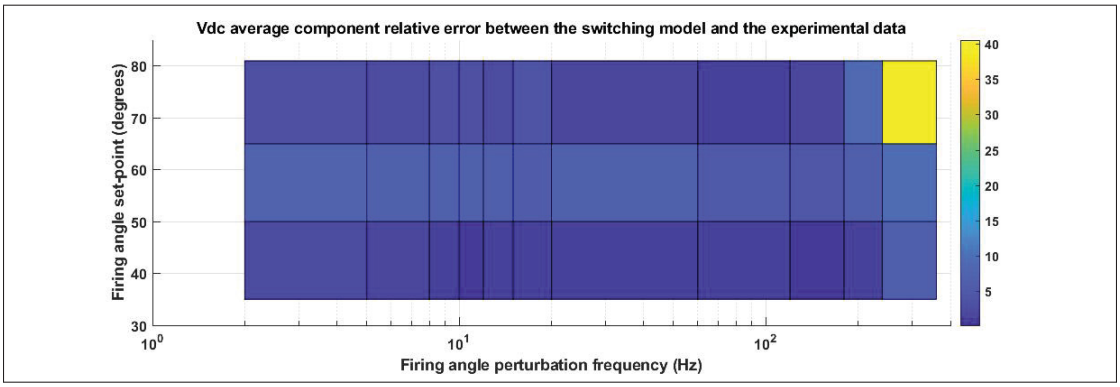

Figure 6.17 Relative error on DC-side voltage DC component between switching model and experimental data for low amplitude perturbations

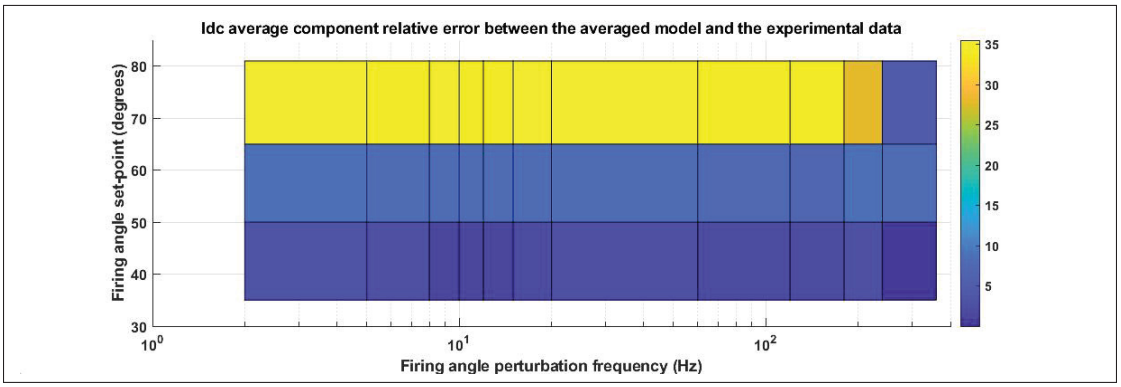

Figure 6.18 Relative error on DC-side current DC component between average model and experimental data for low amplitude perturbations

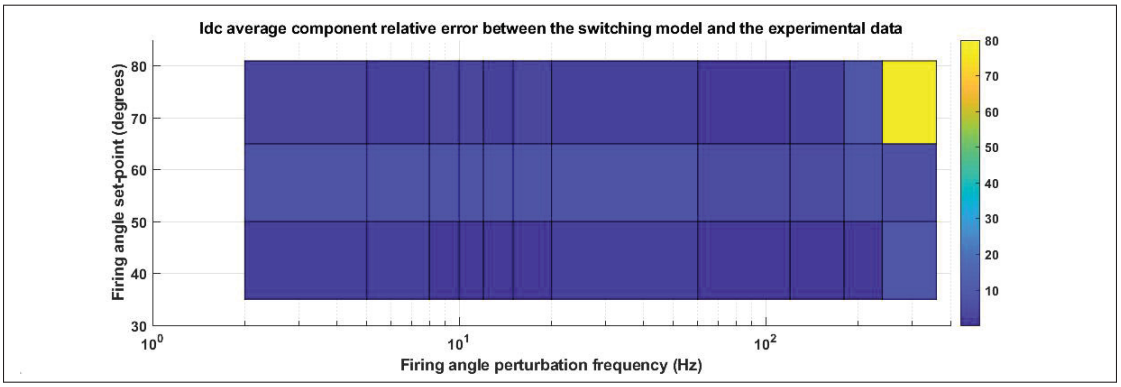

Figure 6.19 Relative error on DC-side current DC component between switching model and experimental data for low amplitude perturbations

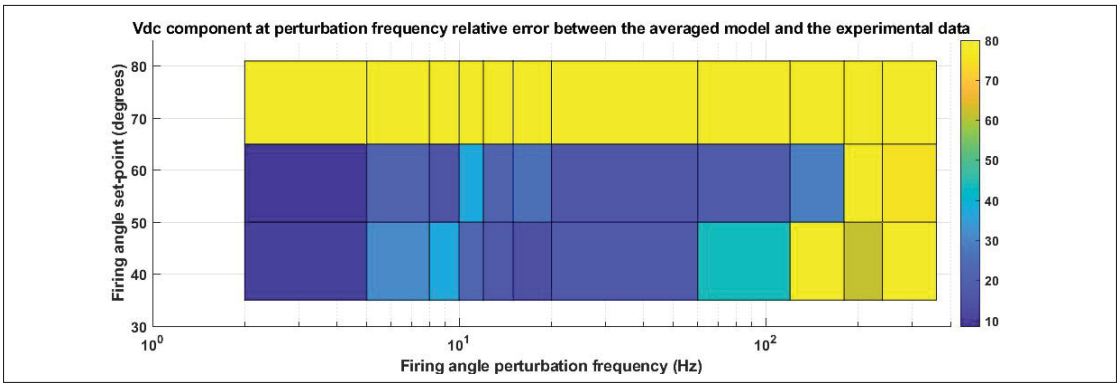

Figure 6.20 Relative error on DC-side voltage component at perturbation output frequency between average model and experimental data for low amplitude perturbations

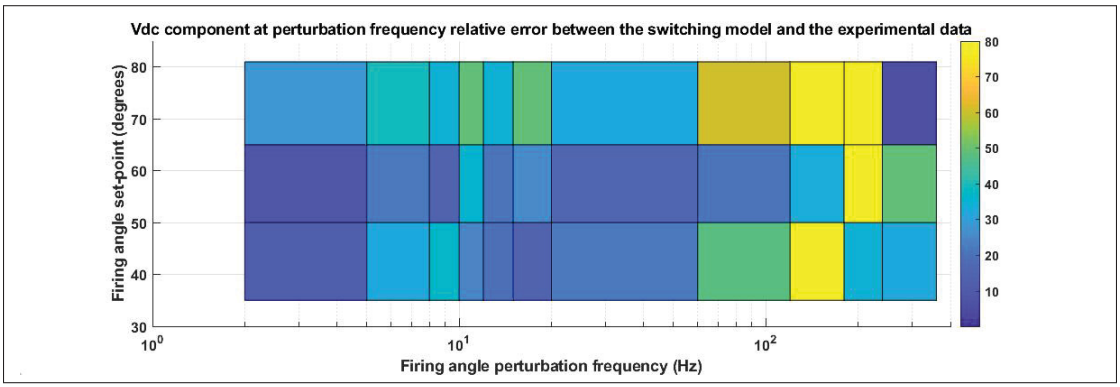

Figure 6.21 Relative error on DC-side voltage component at perturbation output frequency between switching model and experimental data for low amplitude perturbations

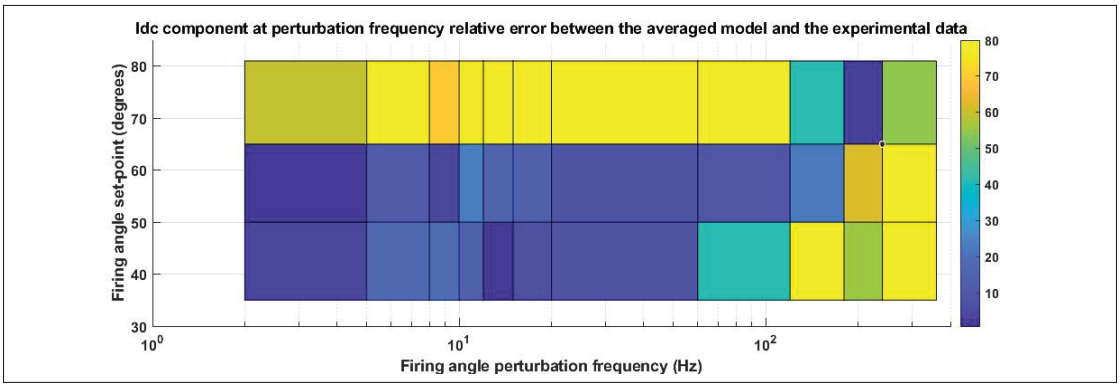

Figure 6.22 Relative error on DC-side current component at perturbation output frequency between average model and experimental data for low amplitude perturbations

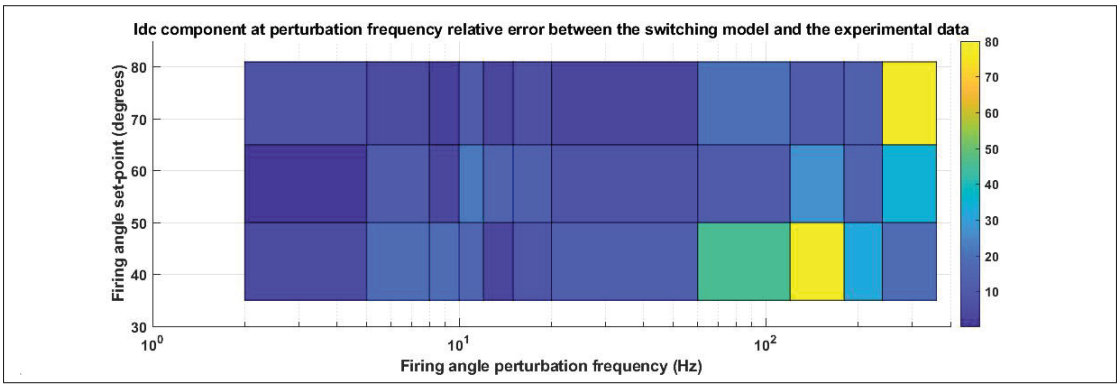

Figure 6.23 Relative error on DC-side current component at perturbation output frequency between switching model and experimental data for low amplitude perturbations

From the error results on figures (6.16-6.23), we distinguish three distinct operating zones. The first is discontinuous conduction mode, which is when the current is too low and reaches zero between the commutations. It happened during the experiments between 65 and 90 degrees of firing angle, and made the average model diverge from both the switching model and the experimental data. The next is the continuous conduction zone at higher frequencies (above 45 Hz), where the errors also rise greatly for both the average and switching models. However,

this error only appears on the voltage curves. This may be because of the RL load filtering the current. Finally, the valid operation zone with continuous conduction and low frequency perturbations (under 45 Hz), where the results match btter between the simulation models and the experimental data. Each of the operation zones will be discussed in its own subsection.

6.3.1 Simulations model performances under discontinuous conduction mode with low perturbation amplitude

It must be noticed that the average model do not fit the experimental data for set-point angles that makes the rectifier enter discontinuous conduction mode, which means that the model is not valid under those conditions. The discontinuous conduction happens for firing angle over about 65 degrees in our experiments, but if the DC load was to change characteristics, the discontinuous conduction zone would be different. In synchronous machine excitation applications, the discontinuous conduction is not supposed to happen because the rotor inductance is so large that it almost perfectly flattens the current curve. However, the switching model is still able to represent well the behavior of the experimental rectifier, even in discontinuous conduction mode (which is expected from a switching model).

To show what happens at firing angles that are too close to 90 degrees and actually cause discontinuous conduction, the temporal curves have been drawn on figures 6.24 and 6.25 for the data set using a firing angle set-point of 81 degrees, with a perturbation frequency of 2 Hz.

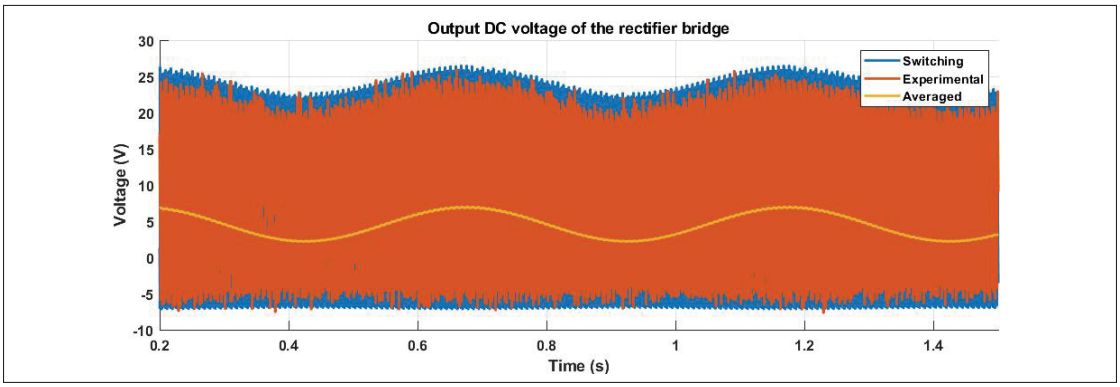

Figure 6.24 DC-side voltage comparison between the models and the experimental data - discontinuous conduction with low frequency perturbations

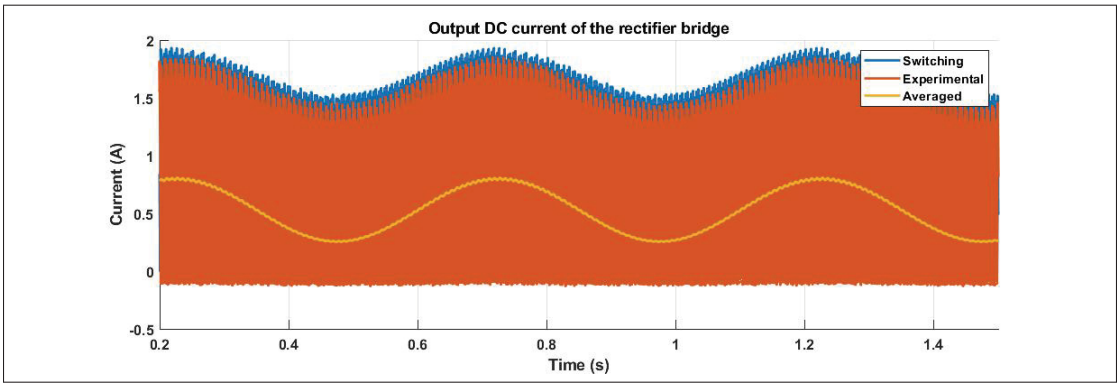

Figure 6.25 DC-side current comparison between the models and experimental data - discontinuous conduction with low frequency perturbations

Notice that the perturbation oscillation on the curves are only represented on the high end of the envelope of the curves of experimental data and switching model. The lower end of the envelope clips the oscillations, which does not happen for the averaged model. This is a visual reference of why the average model do not fit the experimental data under these conditions for both averaging and dynamic representation of the experimental rectifier.

6.3.2 Simulation models performances for high frequency perturbations with low perturbation amplitude

The output voltage and current oscillations on the DC side caused by the firing angle perturbations do not fit between the average model and the experimental data. This means that the model could not be used to represent the transient characteristics of the excitation system because its validity is compromised under those conditions. However, the average values are still well represented, even for high frequencies. The error between the average model and the experimental data could again be caused by either the low-pass behavior of the switching pattern, or the synchronization system, which are absent from the average model.

The switching model's averaged output values fit the experimental data for high perturbation frequencies. It also seems that the switching model behaves better than the averaged model for perturbation representation at higher frequencies. This could be because the switching mechanics are actually included in the switching model, and it also contains a synchronization device dynamics, and the combination of both may approach the firing board's dynamics.

To better visualize the effects on the models under those conditions, figures 6.26 and 6.27 show the temporal curves for a firing angle set-point of 50 degrees, and a perturbation frequency of 240 Hz.

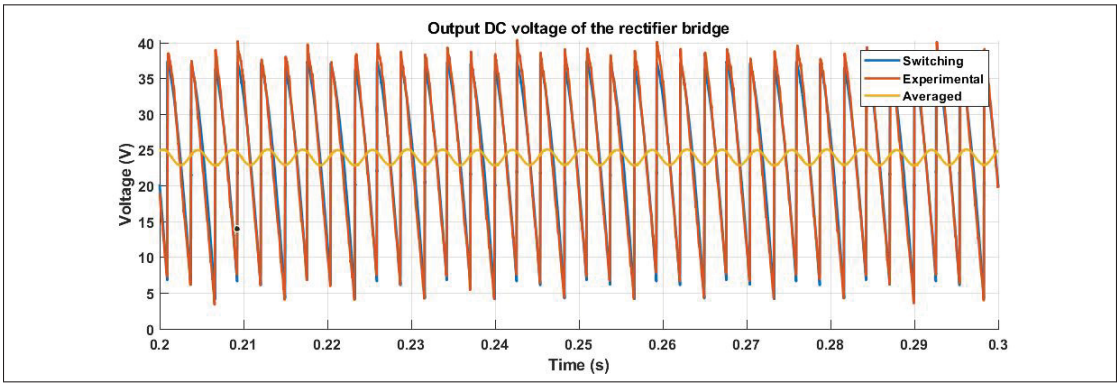

Figure 6.26 DC-side voltage comparison between the models and the experimental data - continuous conduction with high frequency perturbations

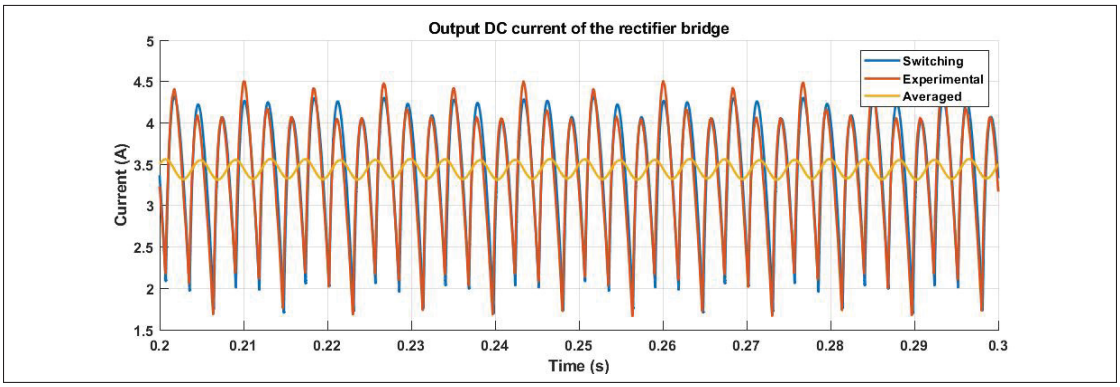

Figure 6.27 DC-side voltage comparison between the models and the experimental data - continuous conduction with high frequency perturbations

From those figures, it is pretty clear that the perturbation output on the switching model and experimental data is filtered by the fact that the bridge can only update its firing angle command 6 times per cycles. Physically speaking, it could be interpreted as a sampling time on the firing angle signal sent to the firing board, with a maximum sampling frequency of 360 Hz. Mathematically, the highest frequency that the rectifier bridge could represent on the DC-side would be 180 Hz, as the Nyquist's frequency states (sampling time has to be faster than 2 times the period of the signal sampled). Though, it is a mathematical limit. To really be able to represent well a signal, a factor of about 10 is usually what is considered acceptable. It could explain why the perturbations do not pass through the experimental rectifier and switching model like it happens for the averaged model.

6.3.3 Simulation models performances during continuous conduction and low perturbation frequencies with low perturbation amplitudes

Continuous conduction mode and low frequencies is actually the conditions under which the average model has to operate in order to be considered valid. Figures 6.28 and 6.29 show the temporal curves for a firing angle set-point of 35 degrees, and a perturbation frequency of 2 Hz.

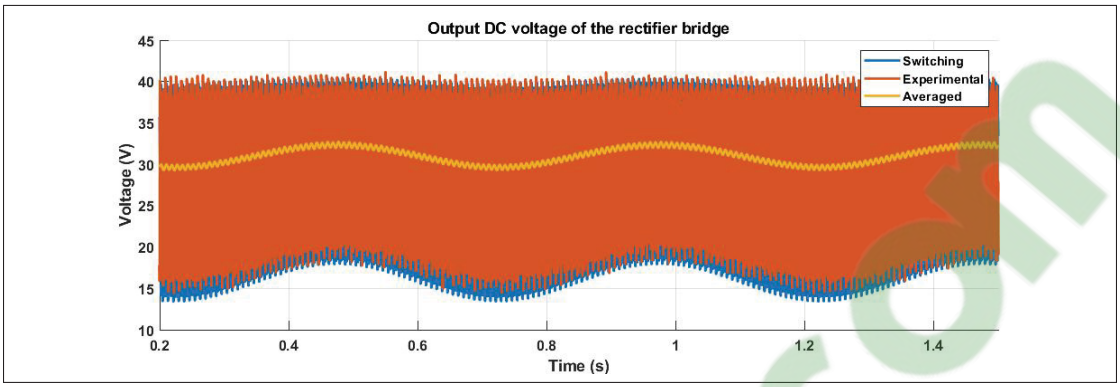

Figure 6.28 DC-side voltage comparison between the models and the experimental data - continuous conduction with low frequency perturbations

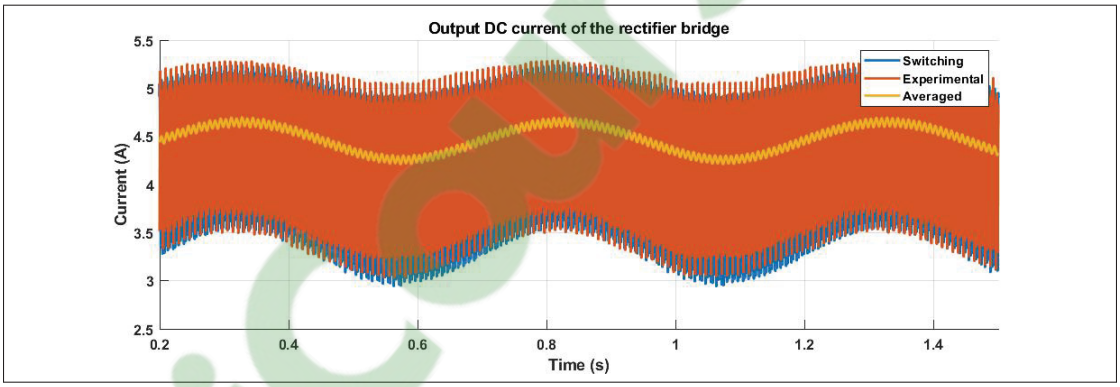

Figure 6.29 DC-side current comparison between the models and the experimental data - continuous conduction with low frequency perturbations

Note that in this operation zone, the average model is able to represent the average value as well as the transient response quite accurately. The error between the average mode and the experimental data is still quite high (between 5 and 20 percent), but we can conclude that considering the dynamics introduced by the firing angle sampling and the synchronization system, the model is valid when operating in continuous conduction and under about 45 Hz.

6.4 Discussion on experimental results

The experimental results have so far shown that the average model built in this research is able to represent an excitation system's steady state and transient behavior correctly, under specific conditions. However, the error between the model and the experimental data is still quite high, and this sections will go through the causes of errors, the limits of the model and the modifications that can be made.

6.4.1 Effects of the on-state resistance of the thyristors on the output voltage

Since the voltage values used during the experiments were quite low compared to normal applications of synchronous machine excitation systems, the on-state voltage drop of the thyristors needed to be added to the averaged rectifier model. In the datasheet of the thyristors used during those experiments, the on-state voltage is considered to cause an average of $V_f = 0.9V$ voltage drop across the thyristors (depending on the temperature). But since the temperature remained low during the experiments, the constant value of $V_f = 0.9V$ was kept. If the thyristors were to undergo aggressive temperature rises while the voltage is low, this value of V_f would maybe need to be modulated as the temperature changes.

To calculate the voltage drop on the DC-side caused by the on-state resistance of the thyristors, we need to consider that two thyristors are connected to the DC-side load at all times. This means that the DC-side voltage suffers a voltage drop of $2V_f$.

6.4.2 Effects of the voltage input imbalance on the DC-side voltage and currents

It has been observed that the DC-side values always had a small 120 Hz components when using the FFT tool on the oscilloscope. This is because there is a negative sequence component to the grid voltage feeding the rectifier in the laboratory. It has also been observed in simulations that the negative sequence creates uneven peaks on the DC-side voltage that are otherwise perfectly even if there is no negative sequence and no perturbation introduced. But unfortunately, it was impossible to remove this component.

We previously established that the qd-frame values in presence of negative sequence when the PLL is locked on the grid's frequency are written:

$$\begin{bmatrix} f_q \\ f_d \\ f_0 \end{bmatrix} = \begin{bmatrix} A_p \sin(\delta_p - \delta_r) + A_n \sin(2\omega t + \delta_n + \delta_r) \\ A_p \cos(\delta_p - \delta_r) - A_n \cos(2\omega t + \delta_n + \delta_r) \\ A_z \sin(\omega t + \delta_z) \end{bmatrix} \tag{6.1}$$

By also placing the PLL at the input bridge voltage V_{br} ($\delta_r = \delta_p$), equation 6.1 becomes:

$$V_{br,qd} = \begin{bmatrix} V_{br,q} \\ V_{br,d} \end{bmatrix} = \begin{bmatrix} V_{br,n} \sin(2\omega t + \delta_n + \delta_p) \\ V_{br,p} - V_{br,n} \cos(2\omega t + \delta_n + \delta_p) \end{bmatrix} \tag{6.2}$$

Using the switching function expression with the system's reference at V_{br} to be coherent with the voltage equation:

$$\begin{bmatrix} S_q \\ S_d \end{bmatrix} = \frac{2\sqrt{3}}{\pi} \begin{bmatrix} -\sin(\alpha(t)) \\ \cos(\alpha(t)) \end{bmatrix} \tag{6.3}$$

We can write the DC-side voltage as:

$$E_{dc} = \frac{3}{2}(V_{br,q} S_q + V_{br,d} S_d) \tag{6.4}$$

And replacing the equations 6.2 and 6.3 into equation 6.4 and locking the PLL on the positive-sequence angle yields:

$$E_{dc} = \frac{3\sqrt{3}}{\pi} V_{br,p} \cos(\alpha(t)) - \frac{3\sqrt{3}}{\pi} V_{br,n} \cos(2\omega t - \alpha(t) + \delta_p + \delta_n) \tag{6.5}$$

From equation (6.5), we see that the DC-side voltage has a DC component created by the positive sequence. However, the negative sequence term has a frequency of 120 Hz.

Since only one phase of the input line voltage was recorded, it is impossible to try to fit the experimental data by comparing the line voltages only. Some experiments have been conducted where no perturbations were added to the firing angle signal. During those experiments, the DC-side voltage peaks should have been always of the same height for a balanced set of voltages and no perturbations were introduced, which was not the case. It is also possible that the uneven DC-side peaks could have been created by the swinging synchronization system's angle. However, the grid feeding the bridge was clearly unbalanced, as the firing board's software always gave uneven phase voltage. As an example, at some point, the phase voltages were (29.6, 30.0, 30.6), but those values were continuously changing. To better match the uneven DC-side experimental voltage peaks, a negative sequence of about 2 percent of the positive sequence grid voltage was added to the simulations. The grid voltage feeding the experimental rectifier may also have a zero-sequence added to it, but the averaged model do not take the zero-sequence into account, so there is no point in adding it to the input signals.

The main concern about the negative sequence on the voltage is its effects on the synchronization system in the laboratory. As discussed in the synchronization system chapter, some systems may not react well to negative sequence. Since we do not know exactly what is the synchronization system included in the firing board, there is no way to know its reaction to unbalanced grid voltage. Though we think that the product is good enough to not be affected by it. To make sure that the unbalanced condition did not affect the simulation files, the UTSP PLL was used because it was made to decouple the negative sequence in a three-phase signal.

6.4.3 Effects of the firing angle command update maximum frequency of the rectifier bridge

The frequency characteristics of the firing board internal filter have not yet been determined, but we know for sure that it exists, and that it will impact the whole excitation system controls bandwidth in some ways. The synchronization system does not need to be fast since the

bandwidth is already restricted by the sampling of the firing board. The applications of the thyristors as an excitation system work well in that case because the machine that needs to be controlled is already really slow since rotor inductance values are high (we expect time constants around the seconds units). However, rectifier bridges using thyristors would not be suitable for ultra-fast motor controls because of their limited bandwidth.

6.5 Discussion on the state-space model validity

Until now, the experimental results are pointing towards a validation of the state-space averaged model. The average output values of the experimental curves and the simulation models are clearly matching, while some non-negligible errors remain on the output at perturbation's frequencies. However, many points have not been discussed, and more experiments could have been done to be sure that the model actually represents the physical behavior of a thyristor based rectifier bridge.

6.5.1 Synchronization system effects on the rectifier bridge dynamics

The first thing that comes to mind is the synchronization device used in simulations and physical experiments. It is thought that the synchronization method used by the firing pulse generation board is possibly based on zero-crossing, and its dynamics remains yet unknown for confidential reasons. To isolate the effects of the synchronization system on the rectifier bridge, the UTSP should have been used in both switching simulation model and physical setup. Also, keep in mind that the synchronization system dynamics is not included in the averaged state-space model. However, it has been done in research papers for power electronics applications and would be the next step to improve the model quality if the research were to be continued.

6.5.2 Firing angle perturbation measurement method

While measuring the perturbation amplitude of the firing angle sent to the rectifier bridge with persistence mode on the oscilloscope, the values obtained were fluctuating, even when

recapturing exactly the same measure. This variance on the perturbation amplitude clearly has an effects on the final results, and could not be quantified correctly to set the boundaries of acceptable errors. Also, it could not be determined precisely if the firing unit has a low-pass characteristic, though we think that there is, since the rectifier bridge can only update its firing angle command between every pulses.

6.5.3 Rectifier bridge dynamics with added impedance on the secondary side of the transformer

Transformer parameters were not experimentally determined, and reasonable values were used to generate simulation waveforms. If inductance were to be added to the lines feeding the bridge, the total inductance seen by the bridge would certainly have affected its dynamic. It remains unknown if the state-space model would still be valid with the added impedance. However, the transformer is still included in the state-space model, which means that there are no major errors impacting the results. We then know that at least the mathematics behind the model are right.

The notch width phenomenon could not be validated experimentally, as impedance would need to be added to the lines. In the state-space model, the secondary side leakage inductance was used as total impedance seen by the rectifier bridge, but it is yet unclear if this hypothesis is correct or not due to the present of supplementary impedance on AC lines.

6.5.4 Simulation errors and instability

The notch filter was not physically implemented in practice since there were almost no voltage notch during the experiments. However, the RC filter model could not be removed from the state-space model since it is used to give the global model the bridge's input voltage inside the model. The values of the RC filter was then tuned to not affect the values of the simulations, but let them run smoothly. It was noticed (but not quantified) that when the RC filter eigenvalues are too far from the main dynamic, the simulation model tends to crash and generate errors as the solving algorithms have a hard time resolving stiff differential equations systems. Keep in mind that there may also be a notion of instability in the simulation model if the solver used

is using a fixed time step. Fixed step simulation needs to be avoided as much as possible, as it generally introduces error when subsystems are coupled together. Using variable time step solving algorithms removes those errors, which is unfortunate since most real-time HIL systems are using fixed-step only.

6.6 Conclusions on the state-space model validity

It has been discovered in this chapter that the excitation system's dynamic is affected by its firing board command update frequency as well as its synchronization system. To answer the question as to why the gains of the excitation system controller needed to be tuned in certain conditions, it may be because the firing unit has its own dynamic at frequencies situated in the bandwidth of the controller.

Three different operating regions have been defined, and the average model is valid only in one of them. Since the valid region is continuous conduction mode at low frequencies, the fact that the excitation system is connected to a synchronous machine guarantees that the average model is always valid for this application. However, the experiments conducted were not perfect, and some errors were surely introduced. The method used to measure the perturbations sent to the firing board had an important variance, and may lead to mismatches between the perturbations sent to the models and the experimental setup. Also, due to physical limitations in the laboratory, the transformer could not be characterized properly. For validation purposes, reasonable parameters were used but they were not matching the experimental setup parameters. The equivalent resistance r_μ was not validated experimentally either, because impedance would have been needed on the AC lines, and again, due to physical limitations in the laboratory, it could not be done.

Since the average model is valid for synchronous machine excitation applications, it can be used to observe the effects of parameter variations on the system's dynamics, which is the subject of the next chapter.

CHAPTER 7

DISCUSSION ON THE FIRST ORDER APPROXIMATION

In this chapter, the dynamics of the excitation system will be analyzed by varying parameters in the state-space model matrix and applying firing angle steps to the average model. To do so, some starting parameters will be chosen, then each section will treat its own parameter variation. The DC resistance has been fixed so that the line currents drawn on the feeding lines would reach 1 per unit when the rectifier receives a firing angle of 30 degrees. Then, the DC inductance has been set to a value that produces a time constant between $0.1s$ and $1s$. The common 5 percent leakage inductance was chosen as a starting value for both primary and secondary sides, with a mutual inductance set at $L_m = 100L_{ls}$. The winding resistances were set at a value of $R = 0.001$ per unit. The filter values were set at $R_f = 10$ per unit and $C_f = 0.1$ per unit.

7.1 Effects of the transformer mutual inductance

In this section, the mutual inductance is varied from 50 to 500 times the value of the leakage inductance. Figures (7.1-7.4) show the excitation system's response to a firing angle step going from 90 to 30 degrees at $t = 0.01s$.

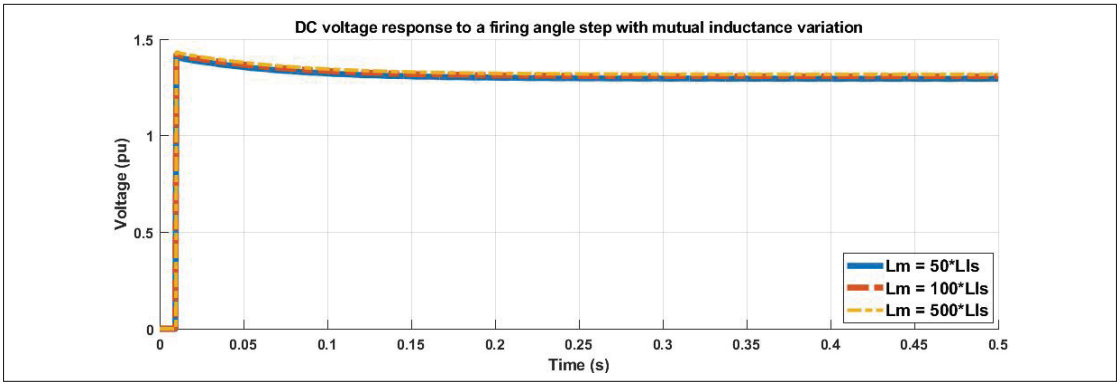

Figure 7.1 DC-side voltage response to a firing angle step with mutual inductance variation

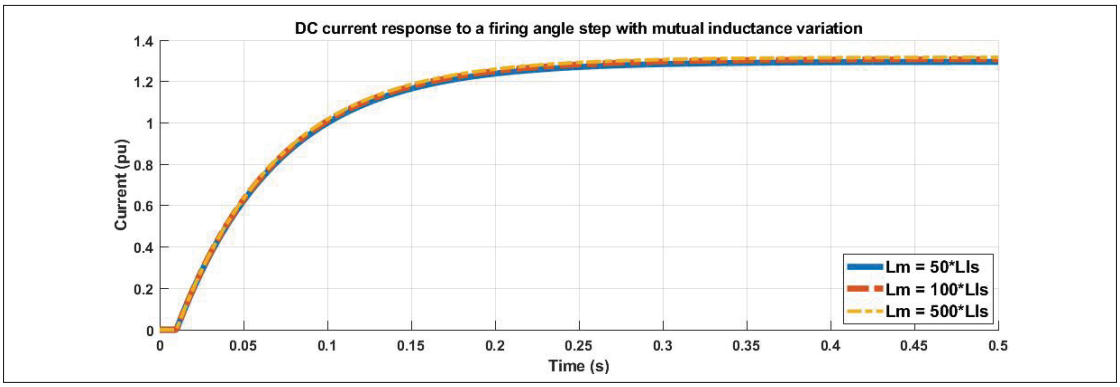

Figure 7.2 DC-side current response to a firing angle step with mutual inductance variation

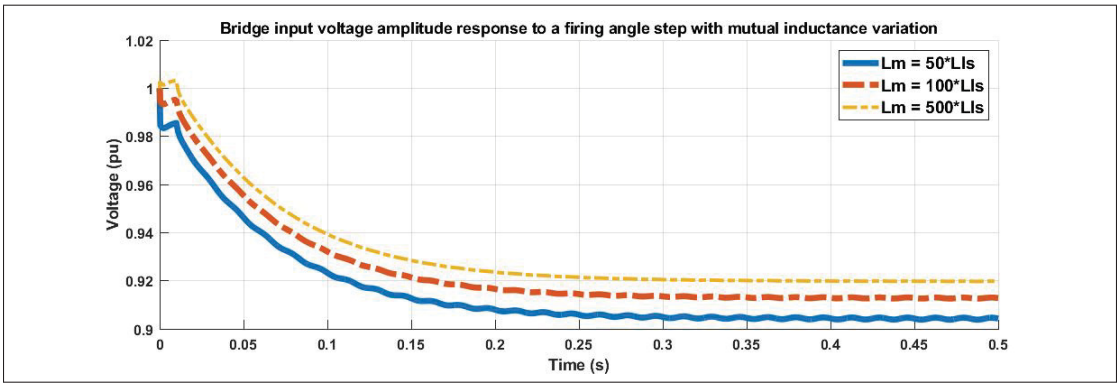

Figure 7.3 Input bridge voltage amplitude response to a firing angle step with mutual inductance variation

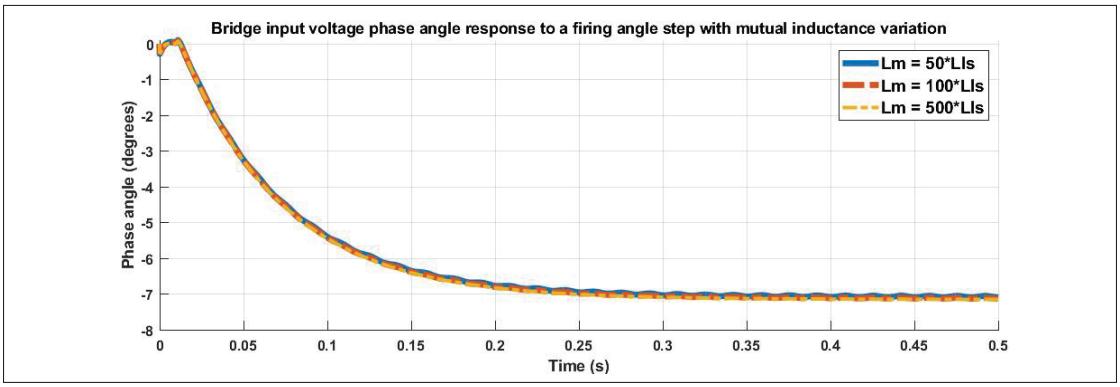

Figure 7.4 Input bridge voltage phase angle response to a firing angle step with mutual inductance variation

Having a higher mutual inductance to leakage inductance ratio usually means that the transformer quality is improved, which explains the voltage drop present at the input of the rectifier bridge as seen on figure 7.3. Notice that the voltage drop also follows a shape that has the same time constant as the DC-side current rising. This would indicate that the machine's rotor time constant dominates the whole system's dynamics. Also, the curves seem to all have the same time constant as the mutual inductance of the transformer is varied, meaning that the dynamic would not be affected by it. However, the steady-state values are affected, as the voltage drop worsens when the mutual inductance is lowered. Since it has been established that the bridge input voltage dynamic is tied to the rotor dynamic, it is now clear that the DC-side voltage dynamic is also governed by the rotor dynamic. It is quite clear on figure 7.1 that the bridge input voltage drop appears on the DC-side, and also follows the rotor dynamic.

7.2 Effects of the transformer leakage inductances

Figures (7.5-7.8) show the system's responses to a firing angle step from 90 to 30 degrees at $t = 0.01s$. Three waveforms have been drawn on each graphs, showing the responses for different leakage inductance values Ll applied to both primary and secondary side leakage inductance parameters. Figures (7.5-7.8) show the excitation system's response to a firing angle step going from 90 to 30 degrees at $t = 0.01s$.

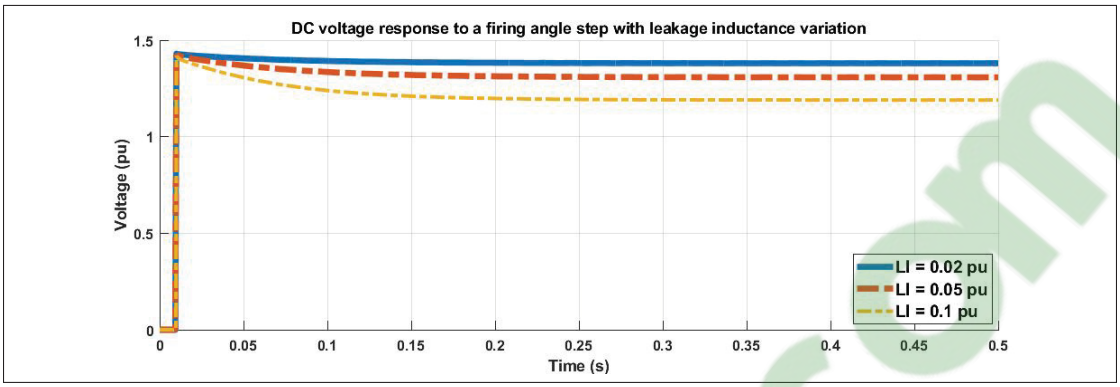

Figure 7.5 DC-side voltage response to a firing angle step with leakage inductance variation

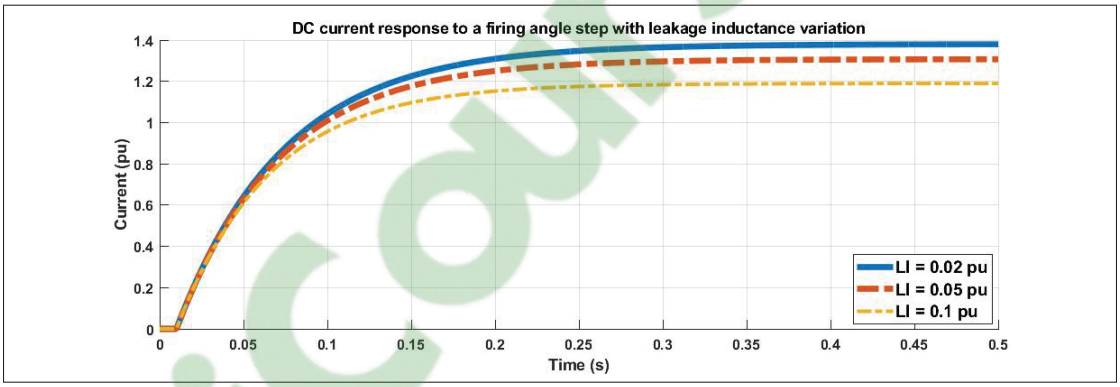

Figure 7.6 DC-side current response to a firing angle step with leakage inductance variation

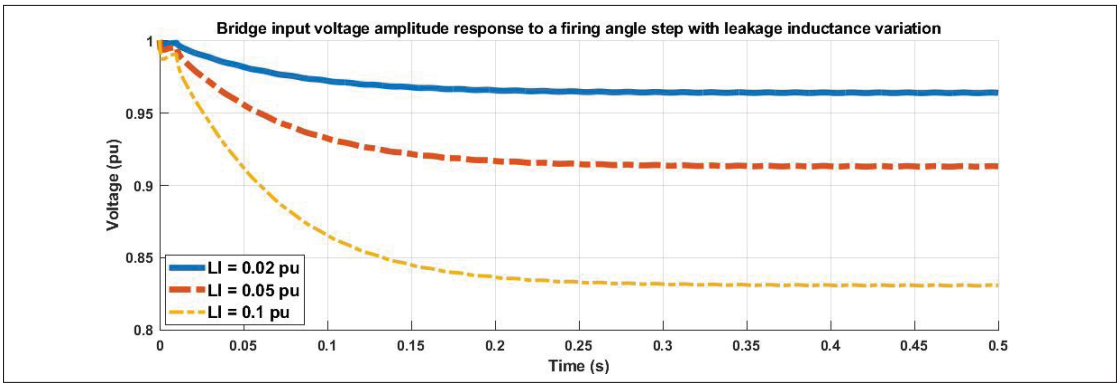

Figure 7.7 Input bridge voltage amplitude response to a firing angle step with leakage inductance variation

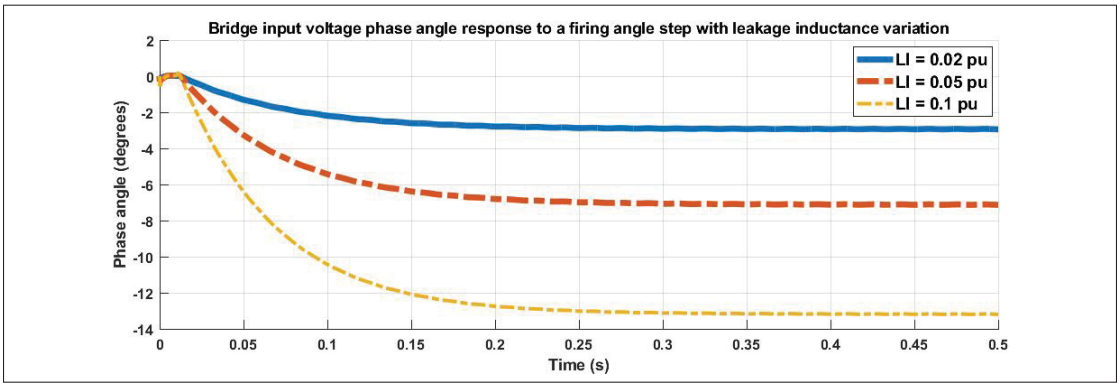

Figure 7.8 Input bridge voltage phase angle response to a firing angle step with leakage inductance variation

The waveforms obtained by leakage inductance variations are quite similar to the ones obtained by mutual inductance variations. Again, we see the rotor dynamic dominating all the variables observed.

7.3 Effects of the transformer winding resistances

Figures (7.9-7.12) show, again, the system's responses to a firing angle step from 90 to 30 degrees at $t = 0.01s$. The resistance values appearing on the graphs are applied on both primary and secondary side parameters are the same time.

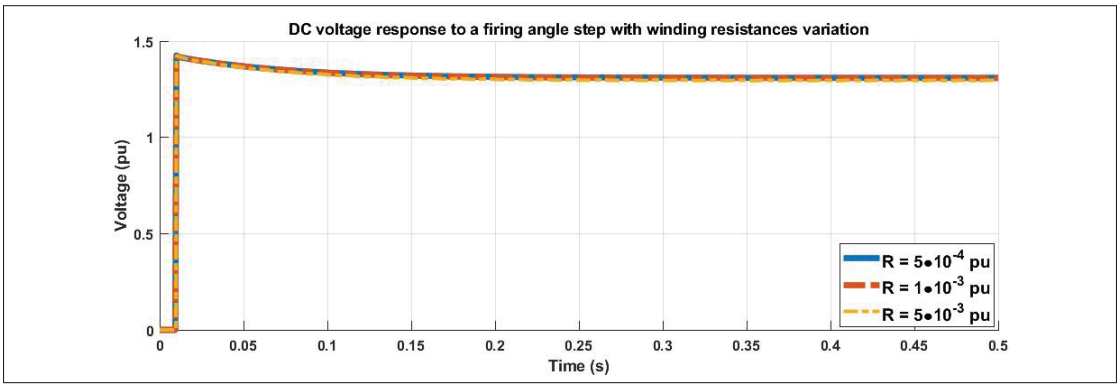

Figure 7.9 DC-side voltage response to a firing angle step with windings resistance variation

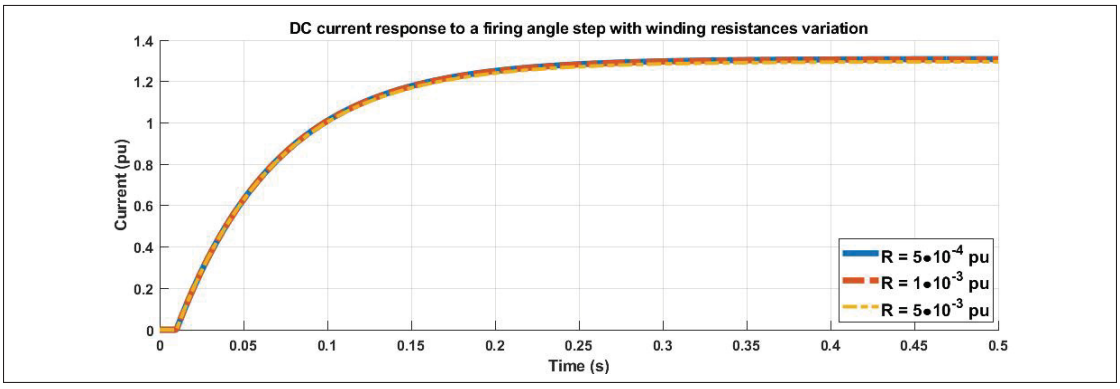

Figure 7.10 DC-side current response to a firing angle step with windings resistance variation

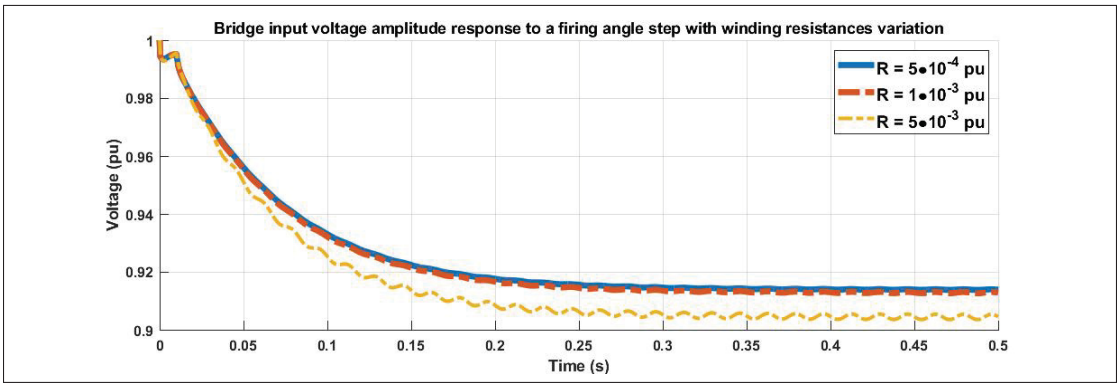

Figure 7.11 Input bridge voltage amplitude response to a firing angle step with windings resistance variation

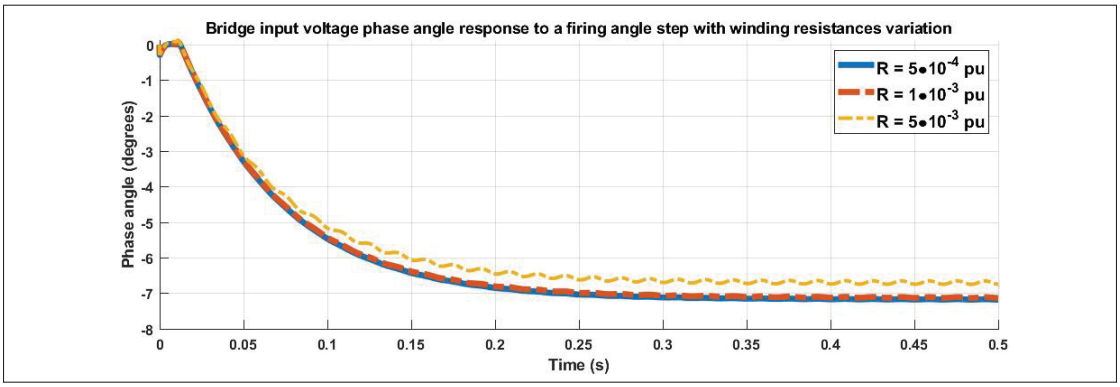

Figure 7.12 Input bridge voltage phase angle response to a firing angle step with windings resistance variation

The resistance in the windings also seems to increase the effects of the first-order dynamic coming from the rotor when line currents are drawn, as it happened with the mutual inductance and the leakage inductances.

7.4 Conclusions on the first-order approximation

It is quite clear now with the step experiments conducted that the whole excitation system's dynamic is governed by the rotor dynamic. It can then be concluded that if the gating circuits and

synchronization system's dynamics are neglected, the whole system actually behaves like a first order on all its observed variables when the system's parameters are varied within reasonable range. However, the first-order characteristic seem to affect the variables even more as the transformer's mutual inductance lowers, or as the leakage inductance or windings resistances increases. Any parameter that affects the voltage drop across the transformer will also affect the dynamic of the voltage output. Since the voltage drop is cause be the current passing through the transformer, the dynamic of the current drawn in the feeding lines also affects the voltage output. Also, it has previously been established that the excitation system controller would be affected by the firing board. To investigate further, the firing board's dynamic would need to be characterized better, and introduced in the state-space model.

CONCLUSION AND RECOMMENDATIONS

The goal of this research was to understand why it can usually be assumed that the excitation systems follow a first-order dynamic since the industrial partner sometimes had to re-tune the control system's gains in certain situations. To answer this question, an average mathematical model of a thyristor-based excitation system for synchronous generator needed to be built in Park's reference frame, which included an excitation transformer, a notch filter and a six-pulse rectifier bridge. To validate each of these subsystems by comparison with a switching model, a synchronization system needed to be designed. Then, the average model was compared with an experimental setup, which did not include the notch filter as there were no notches on the feeding lines. However, the filter's parameters were set in a way that it would not affect the results since it could not be removed from the model. During the physical experiments, it was discovered that the firing board including the gating circuits and the synchronization system actually have a dynamic that is centered right in the expected bandwidth of the excitation system's controller. It was also uncovered that the command update of the firing board actually forces a low-pass characteristics on the firing angle command. Finally, after the mathematical model was validated through simulation and physical experiments, it was used to conduct a dynamics analysis of the main variables of the system by sending firing angle steps to the average model. It was brought to light that the rotor time constant seems to appear on all the observed variables, but its effects increased as the transformer's quality worsened. However, since the average model does not include the firing board dynamics, the interaction between the controller and the firing board could not be analyzed.

In conclusion, the excitation system appears to be ruled by a first order dynamic, as long as the gating circuits and synchronization system dynamics can be neglected. However, it does not appear to be the case as the firing board clearly has a dynamic centered in the control system's dynamics.

In order to pursue the research, the gating circuits and synchronization system should be characterized and included in the average model to uncover the true dynamic affecting the control system. Also, the physical experiment should be redone with added impedance on the feeding lines, and physical firing angle step experiments should be conducted. Building a synchronization system would allow to change its dynamics and test the effects of its tuning on the excitation system. Correctly characterizing the transformer would also bring great value to this project. Connecting the excitation system to an actual synchronous generator would also advance the project by a lot, but would require much more time and effort than the other recommendations.

The industrial partner now knows that the gating circuits and the synchronization system affect the controller's dynamics and may break the first-order approximation validity, but that the first-order characteristic in question comes from the interaction between the transformer and the rotor dynamics.

BIBLIOGRAPHY

Adkins B., R. H. (1975). *The General Theory of Alternating Current Machines* (ed. 1). Chapman and Hall.

Balabanian N., T. A. B. (1969). *Electrical Network Theory* (ed. 1). Wiley and Sons.

Belkhayat, M. (1997). *Stability Criteria for AC power systems*. (Ph.D. thesis, Purdue University, West Lafayette, Indiana, USA).

Best, R. (2003). *Phase-Locked Loops : Design, Simulations and Applications*. McGraw-Hill Inc.

Bevrani H.,F. B., T. I. (2017). *Microgrid Dynamics and Control* (ed. 1). Wiley and Sons.

Chaijarurnudomrung K.,K.-N. A., K.-L. A. (2010). Modeling of Three-phase Controlled Rectifier using a DQ method.

Chapman, S. (2012). *Electric Machinery Fundamentals*. McGraw-Hill Inc.

Chen, C.-T. (1999). *Linear system theory and design* (ed. 3). New York, Oxford: Oxford University Press.

Corinthios, M. (2009). *Signals, Systems, Transforms, and Digital Signal Processing with MATLAB* (ed. 1). CRC Press.

Dupré, G. (2019). *Contrôle d'une unité de production d'énergie décentralisée raccordée à un réseau de distribution déséquilibré*. (Master's thesis, Polytechnique de Montréal, Montréal, Canada).

Erickson R., D. M. (2004). *Fundamentals of Power Electronics*. Kluwer Academic Publishers.

Escarela-Perez R.,N. T., C.-L. E. (2001). Synchronous Machine Parameters from Frequency-Response Finite-Element Simulations and Genetic Algorithms. *IEEE Transactions on Energy Conversion*, 16(2), 198-203.

Francis, G. (2010). *An Algorithm and system for measuring impedance in d-q coordinates*. (Ph.D. thesis, Virginia Polytechnic Institute and State University, Blacksburg, Virginia, USA).

Graham, A. D. (1993). *Frequency domain analysis for multiple controlled rectifiers*. Communication presented in 1993 Fifth European Conference on Power Electronics and Applications, Brighton, UK (pp. 205-210).

IEEE. (2002). *IEEE Guide for Synchronous Generator Modeling Practices and Applications in Power System Stability Analyses*. IEEE Std 1110-2002.

Karimi, H. (2008). *Islanding Detection and Control of an Islanded Electronically-Coupled Distributed Generation Unit*. (Ph.D. thesis, University of Toronto, Toronto, Canada).

Karimi H.,Y. S., M. K.-G. (2019, June). *A Robust and Simple Phase-Locked Loop for Unbalanced Power Grid Applications*. Communication presented in 2019 IEEE 28th International Symposium on Industrial Electronics (ISIE), Vancouver, BC, Canada (pp. 29-34).

Karimi H., S. S. (2012). *Stability analysis of a single-phase phase-locked loop for power system applications*. Communication presented in The 11th International Conference on Information Sciences, Signal Processing and their Applications: Special Sessions, Montréal, QC, Canada (pp. 1383-1387).

Krause, P. (2002). *Electric Machinery and Drive Systems*. John Wiley Sons, Inc.

Kundur, P. (1994). *Power system stability and control* (ed. 1). McGraw-Hill, Inc.

Mohan, N. (2003). *Power Electronics: Converters, Applications and Design*. John Wiley Sons, Inc.

Rashid, M. H. (2001). *Power Electronics Handbook*. Academic Press.

Streetman G. B., S. K. B. (2015). *Solide State electronic Devices* (ed. 7). Pearson.

Sudhoff S.D., O. W. (1993). Analysis and average-value modeling of line-commutated converter - Synchronous machine systems. *IEEE Transactions on Energy Conversion*, 8(1), 92-99.

Verma V.,K. S. S., S. J. (2017). *State space modeling of three-phase transformers for small-signal analysis of a microgrid*. Communication presented in 2017 North American Power Symposium (NAPS), Morgantown, WV.

Wood, A. J. (1996). *Power Generation Operation and Control* (ed. 2). Wiley and Sons.

Zhang B.,Yi S., H. X. (2000, October). *A novel harmonic current detection technique based on a generalized dq coordinate transform for active power filter and fault protection of power system*. Communication presented in 5th Conference on Advances in Power System Control, Operation and Management, APSCOM 2000, Hong Kong (pp. 543-547).